



Defense Threat Reduction Agency
8725 John J. Kingman Road, MS
6201 Fort Belvoir, VA 22060-6201



DTRA-TR-17-5

TECHNICAL REPORT

Mechanisms of Radiation-Induced Effects in Carbon Nanotubes

Distribution Statement A. Approved for public release; distribution is unlimited.

October 2016

HDTRA1-10-1-0122

Brian J. Landi, et al.

Prepared by:
Rochester Institute of
Technology
160 Lomb Memorial Dr.
Rochester, NY 14604

DESTRUCTION NOTICE:

Destroy this report when it is no longer needed.
Do not return to sender.

PLEASE NOTIFY THE DEFENSE THREAT REDUCTION
AGENCY, ATTN: DTRIAC/ J9STT, 8725 JOHN J. KINGMAN ROAD,
MS-6201, FT BELVOIR, VA 22060-6201, IF YOUR ADDRESS
IS INCORRECT, IF YOU WISH IT DELETED FROM THE
DISTRIBUTION LIST, OR IF THE ADDRESSEE IS NO
LONGER EMPLOYED BY YOUR ORGANIZATION.

REPORT DOCUMENTATION PAGE					<i>Form Approved</i> OMB No. 0704-0188	
<p>The public reporting burden for this collection of information is estimated to average 1 hour per response, including the time for reviewing instructions, searching existing data sources, gathering and maintaining the data needed, and completing and reviewing the collection of information. Send comments regarding this burden estimate or any other aspect of this collection of information, including suggestions for reducing the burden, to Department of Defense, Washington Headquarters Services, Directorate for Information Operations and Reports (0704-0188), 1215 Jefferson Davis Highway, Suite 1204, Arlington, VA 22202-4302. Respondents should be aware that notwithstanding any other provision of law, no person shall be subject to any penalty for failing to comply with a collection of information if it does not display a currently valid OMB control number.</p> <p>PLEASE DO NOT RETURN YOUR FORM TO THE ABOVE ADDRESS.</p>						
1. REPORT DATE (DD-MM-YYYY) 00-10-2016		2. REPORT TYPE Technical			3. DATES COVERED (From - To) Oct 5, 2010 - Dec 31, 2015	
4. TITLE AND SUBTITLE Mechanisms of Radiation-Induced Effects in Carbon Nanotubes				5a. CONTRACT NUMBER HDTRA1-10-1-0122		
				5b. GRANT NUMBER		
				5c. PROGRAM ELEMENT NUMBER		
6. AUTHOR(S) Brian J. Landi, PhD, Principal Investigator Seth Hubbard, PhD, (co-PI) Cory Cress, PhD, (co-PI)				5d. PROJECT NUMBER		
				5e. TASK NUMBER		
				5f. WORK UNIT NUMBER		
7. PERFORMING ORGANIZATION NAME(S) AND ADDRESS(ES) Department of Chemical Engineering Rochester Institute of Technology 160 Lomb Memorial Dr Rochester, NY 14604-5603					8. PERFORMING ORGANIZATION REPORT NUMBER	
9. SPONSORING/MONITORING AGENCY NAME(S) AND ADDRESS(ES) Defense Threat Reduction Agency 8725 John J. Kingman Road STOP 6201 Fort Belvoir, VA 22060					10. SPONSOR/MONITOR'S ACRONYM(S) DTRA	
					11. SPONSOR/MONITOR'S REPORT NUMBER(S) DTRA-TR-17-5	
12. DISTRIBUTION/AVAILABILITY STATEMENT Distribution Statement A. Approved for public release; distribution is unlimited.						
13. SUPPLEMENTARY NOTES						
14. ABSTRACT The research agenda was highly impactful on understanding the fundamental radiation response of nanocarbon materials (CNTs and graphene) and the nanoscale electronic devices comprising them. The primary outcome of this program, determined using both theory and experiment, has been a complete understanding of the mechanisms of radiation damage in carbon nanotubes as a function of their chirality-dependent effects (i.e., influence of electronic-type, diameter, etc.), and an understanding of the defect types created for both ionizing and non-ionizing particles under exposure to high total ionization and displacement damage doses.						
15. SUBJECT TERMS Carbon nanotube (CNT), conductivity, defects, radiation effects, molecular dynamics, transistor						
16. SECURITY CLASSIFICATION OF:			17. LIMITATION OF ABSTRACT	18. NUMBER OF PAGES	19a. NAME OF RESPONSIBLE PERSON	
a. REPORT	b. ABSTRACT	c. THIS PAGE			Jacob Calkins	
U	U	U	SAR	74	19b. TELEPHONE NUMBER (Include area code) 703-767-3075	

UNIT CONVERSION TABLE

U.S. customary units to and from international units of measurement^{*}

U.S. Customary Units	<div style="display: inline-block; text-align: right;"> Multiply by </div> <div style="display: inline-block; text-align: left;"> Divide by[†] </div>	International Units
Length/Area/Volume		
inch (in)	2.54 $\times 10^{-2}$	meter (m)
foot (ft)	3.048 $\times 10^{-1}$	meter (m)
yard (yd)	9.144 $\times 10^{-1}$	meter (m)
mile (mi, international)	1.609 344 $\times 10^3$	meter (m)
mile (nmi, nautical, U.S.)	1.852 $\times 10^3$	meter (m)
barn (b)	1 $\times 10^{-28}$	square meter (m ²)
gallon (gal, U.S. liquid)	3.785 412 $\times 10^{-3}$	cubic meter (m ³)
cubic foot (ft ³)	2.831 685 $\times 10^{-2}$	cubic meter (m ³)
Mass/Density		
pound (lb)	4.535 924 $\times 10^{-1}$	kilogram (kg)
unified atomic mass unit (amu)	1.660 539 $\times 10^{-27}$	kilogram (kg)
pound-mass per cubic foot (lb ft ⁻³)	1.601 846 $\times 10^1$	kilogram per cubic meter (kg m ⁻³)
pound-force (lbf avoirdupois)	4.448 222	newton (N)
Energy/Work/Power		
electron volt (eV)	1.602 177 $\times 10^{-19}$	joule (J)
erg	1 $\times 10^{-7}$	joule (J)
kiloton (kt) (TNT equivalent)	4.184 $\times 10^{12}$	joule (J)
British thermal unit (Btu) (thermochemical)	1.054 350 $\times 10^3$	joule (J)
foot-pound-force (ft lbf)	1.355 818	joule (J)
calorie (cal) (thermochemical)	4.184	joule (J)
Pressure		
atmosphere (atm)	1.013 250 $\times 10^5$	pascal (Pa)
pound force per square inch (psi)	6.984 757 $\times 10^3$	pascal (Pa)
Temperature		
degree Fahrenheit (°F)	$[T(^{\circ}\text{F}) - 32]/1.8$	degree Celsius (°C)
degree Fahrenheit (°F)	$[T(^{\circ}\text{F}) + 459.67]/1.8$	kelvin (K)
Radiation		
curie (Ci) [activity of radionuclides]	3.7 $\times 10^{10}$	per second (s ⁻¹) [becquerel (Bq)]
roentgen (R) [air exposure]	2.579 760 $\times 10^{-4}$	coulomb per kilogram (C kg ⁻¹)
rad [absorbed dose]	1 $\times 10^{-2}$	joule per kilogram (J kg ⁻¹) [gray (Gy)]
rem [equivalent and effective dose]	1 $\times 10^{-2}$	joule per kilogram (J kg ⁻¹) [sievert (Sv)]

^{*} Specific details regarding the implementation of SI units may be viewed at <http://www.bipm.org/en/si/>.

[†] Multiply the U.S. customary unit by the factor to get the international unit. Divide the international unit by the factor to get the U.S. customary unit.

Mechanisms of Radiation-Induced Effects in Carbon Nanotubes

**Final Report
February, 2016**

Grant No. HDTRA1-10-1-0122

DTRA Program Manager Dr. Jacob Calkins (jacob.a.calkins.civ@mail.mil)	
Team	
Dr. Brian J. Landi (PI), Dr. Seth Hubbard (co-PI) Rochester Institute of Technology 1 Lomb Memorial Drive Rochester, New York 14623	Dr. Cory Cress (co-PI) Naval Research Labs Washington, DC
Test structure fabrication, radiation effects testing, and MD simulation	Radiation effects testing and analysis

Technical Point of Contact:
Dr. Brian J. Landi (brian.landi@rit.edu); 585-475-4726
Rochester Institute of Technology, Department of Chemical Engineering
160 Lomb Memorial Drive, Building 73, Room 4107
Rochester, New York 14623

Administrative Point of Contact
Katherine Clark (kacsrs@rit.edu); 585-475-7984
RIT Sponsored Research Services
2400 University Services Center
Rochester, New York, 14623

1. EXECUTIVE SUMMARY

High performance nanoelectronics employing carbon nanotubes are earmarked to replace conventional semiconductor devices in the near future. At the onset of the current program, carbon nanotube technology was quickly showing viability, yet very little was understood about the stability of carbon nanotube structures under hostile environments. This joint program between the NanoPower Research Laboratories (NPRL) at Rochester Institute of Technology (RIT) and the U.S. Naval Research Laboratory (NRL) has supported the Basic and Applied Sciences Directorate, Basic Research for Combating Weapons of Mass Destruction (C-WMD), Topic F: Science for Survivable Nano-scale Electronics (Thrust 3), and focused specifically on “Basic material and radiation effects research...on carbon nanotubes...” The research agenda was highly impactful on understanding the fundamental radiation response of nanocarbon materials (CNTs and graphene) and the nanoscale electronic devices comprising them. Thus, the primary outcome of this program, determined using both theory and experiment, is a complete understanding of the mechanisms of radiation damage in carbon nanotubes as a function of their chirality-dependent effects (*i.e.*, influence of electronic-type, diameter, etc.), and an understanding of the defect types created for both ionizing and non-ionizing particles under exposure to high total ionization and displacement damage doses. Additionally, the radiation effects on CNT carrier transport parameters (mobility, lifetime, conductivity) have been characterized to establish defect generation rates and chirality-dependent radiation response. Being able to predict which particle:SWCNT interaction (*i.e.*, the ionizing or non-ionizing energy loss of the particle) that leads to the largest phenomenological response has enabled recovery of CNT physical and electrical properties after radiation exposure, and allowed for the design of radiation hardened oxides to mitigate such effects in nanoelectronic devices slated for environments pertinent to C-WMD applications.

2. RECENT ACCOMPLISHMENTS

A. *Carbon Nanotube-Based Sensenna*: As a result of work performed under this grant, a patent opportunity has been identified, wherein a resonant SWCNT thin-film antenna can be used as a remote wireless sensor and transmitter. The uniqueness of the invention is that the resonant SWCNT thin-film antenna structure is used both as the sensing and transmitting element, reducing system complexity and cost. In addition to sensing radiation, as shown in the example in Section 7.2 of this report, the SWCNT thin-film antenna can be further modified to sense other environmental factors that affect its conductivity and resonance characteristics.

B. *Molecular Dynamics Simulation and Modeling*: Two new open-source computational “toolkits” were developed to facilitate the preparation and post-processing analysis of the MD simulations input and output, respectively. The first toolkit, TASR, is a Toolkit for Atomistic Simulation with Radiation, provides several tools for performing large, systematic molecular dynamics simulation studies of irradiation effects in matter. It has been designed to be useful to the non-expert scientist interested in performing molecular dynamics simulations of irradiation by providing a single input configuration file in which the user is able to define the parameters necessary to run complete molecular dynamics “experiments” from start to finish. Structure data and input simulation script formatted for the specific MD engine being used are all handled by TASR behind the scenes. The second package, scikit-nano, is a

toolkit for generating and analyzing nanostructure data, including single- and multi-walled nanotubes, graphene, fullerenes, and any combinations thereof. Both of these toolkits are written in the Python programming language and leverage many popular open-source Python packages including numpy and scipy.

3. EXPERIMENTAL PROCEEDURES, RESULTS, AND DISCUSSION

1. Synthesis and Separation of SWCNTs

1.1 SWCNT Synthesis

SWCNTs used in this program were synthesized at the Nanopower Research Labs (NPRL) at RIT via laser vaporization using either an Alexandrite (755nm) or Nd:YAG (1064nm) laser. Depending on the carrier gas, pressure, and temperature used, the chirality of the resulting SWCNT soot can be modified to produce SWCNT samples of varying diameter distribution.¹ In addition to the SWCNTs synthesized at RIT, HiPco (CNI Carbon Nanotubes) and CoMoCAT (SWeNT SG65) soot was purchased with diameter distributions smaller than those that can be produced by laser vaporization. The availability of varying as-produced SWCNT materials allows for the survey of different separations techniques, which provides a large enough samples set to study the diameter and electronic-type SWCNT radiation response across a typical range of SWCNT materials. In addition, the efficacy of the separations performed at RIT was compared to commercially available, electronic-type-separated SWCNT materials purchased from NanoIntegris, Inc, the only commercial supplier of separated SWCNT materials. These SWCNT materials, which contain the largest diameter distribution of all synthetic materials examined in the current study, were synthesized using arc discharge, and have been separated by density gradient ultracentrifugation (DGU).

1.2 SWCNT Electronic-Type Separations

SWCNTs were separated using a well established column chromatography method first proposed by H. Kataura et al.² This process allows for SWCNT separation based on electronic-types, and was optimized at RIT to accommodate the differing as-produced SWCNT materials available (laser vaporization, HiPco, and CoMoCAT). SWCNTs were dispersed in an aqueous 2.0 wt% SDS solution through bath and horn ultracentrifugation, which is required for the exfoliation of individual SWCNTs from the bundles. The resulting dispersions were ultracentrifuged at 110,000×g to remove carbonaceous and metal catalyst impurities, as well as any remaining bundled SWCNT material. The top 90% of the supernatant was decanted from the pellet after ultracentrifugation and used as the starting material in the separation process. Chromatography columns were packed with an allyl dextran-based agarose gel bead (GE Sepharose 2b), and the stationary phase protected by a layer of sand (Figure 1a). The prepared SWCNT dispersions were applied to the top of the column (Figure 1b) and allowed to soak into the layer of sand before proceeding with the electronic-type separation. M-SWCNTs were eluted first from the column (Figure 1c) using 2.0 wt% SDS, followed by the elution of the S-SWCNTs (Figure 1d) in 2.0 wt% sodium deoxycholate (DOC).

By increasing both the diameter and effective length of the chromatography column, the separation technique has been optimized to improve the efficacy and throughput of the separation. Compared to initial published results, the chromatography columns currently

being employed at RIT have a diameter 5x larger and effective length more than 4x greater. The increased length of the column has produced the most gain in improving the quality of the separated SWCNT samples. It has been observed that residual nanostructured carbon impurities elute after the M-SWCNT band in 2.0 wt% SDS. With insufficient column lengths, the impurities mix together with the metallic SWCNTs causing contamination of the M-SWCNT fractions. Likewise, the increased inner diameter of the column allows for separation of more than 50x the volume compared to the original column. While the full capacity of the largest column has not yet been fully realized, the quality of the separated M-SWCNT and S-SWCNT materials has been significantly improved. Continuing to increase the column dimensions will advance the throughput of SWCNT material that can be processed in a single separation step.

Column chromatography has been successfully implemented for the separation of laser-Ar, laser-He, HiPco, and CoMoCAT SWCNT materials, thus yielding metallic and semiconducting chiral fractions of different diameter distributions. Following separation, the metallic and semiconducting fractions are vibrantly colored compared to the initially black starting dispersions, which contain both electronic-types. When the metallic and semiconducting SWCNTs are mixed, the dispersion appears to be black due to the overlapping absorption bands of each individual SWCNT, covering nearly the entire range of the visible spectrum.³ However, when the metallic and semiconducting SWCNTs are separated, the dispersions take on different colors depending on their diameter distribution, and ultimately the peak position of the optical absorption band. Each separated fraction was analyzed by optical absorbance spectroscopy to evaluate the efficiency of the separation (Figure 2). Compared to the starting dispersion prior to separation (black line), the metallic fractions (blue line) show a diminished S-SWCNT signal, and the semiconducting fractions (red line) show a diminished M-SWCNT signal. In addition to the absorption data, a photograph of each colored fraction is shown for a visual comparison of the difference in diameter distribution (Figure 3).

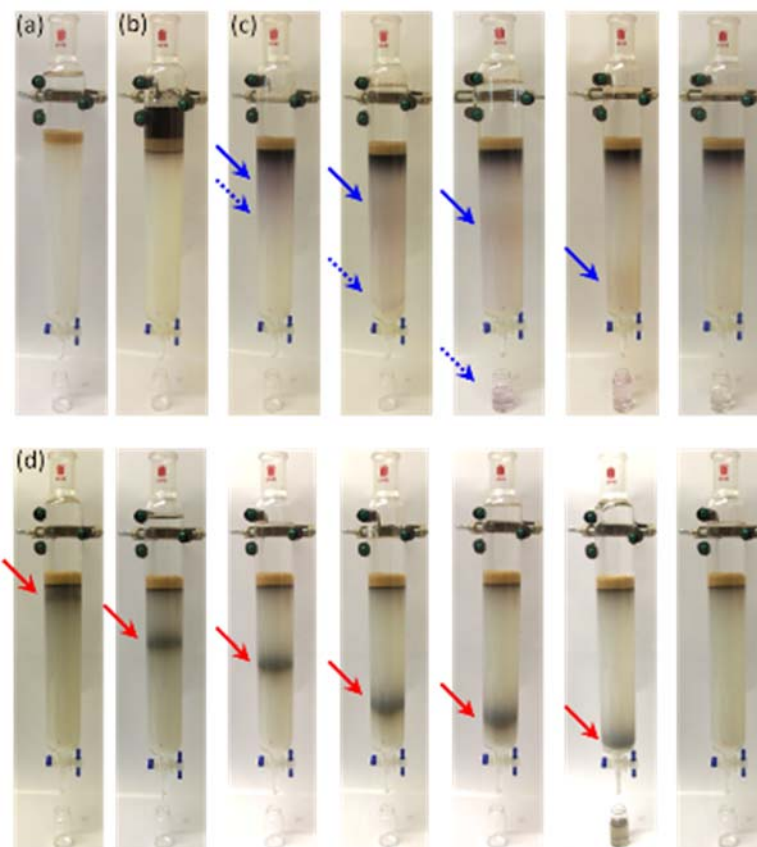


Figure 1. A representative process flow for the electronic-type-separation of SWCNTs via column chromatography is demonstrated. (a) The chromatography column is prepared with a Sepharose 2B stationary phase protected by a layer of sand. (b) A SWCNT dispersion prepared in 2.0 wt% SDS is loaded onto the column and allowed to soak into the stationary phase. (c) M-SWCNTs are eluted from the column in 2.0 wt% SDS, followed by (d) the S-SWCNTs in 2.0 wt% DOC. The blue and red arrows are intended to draw the viewers' attention to the SWCNT band migrating through the chromatography column prior to the elution of the M-SWCNT and S-SWCNT fractions, respectively.

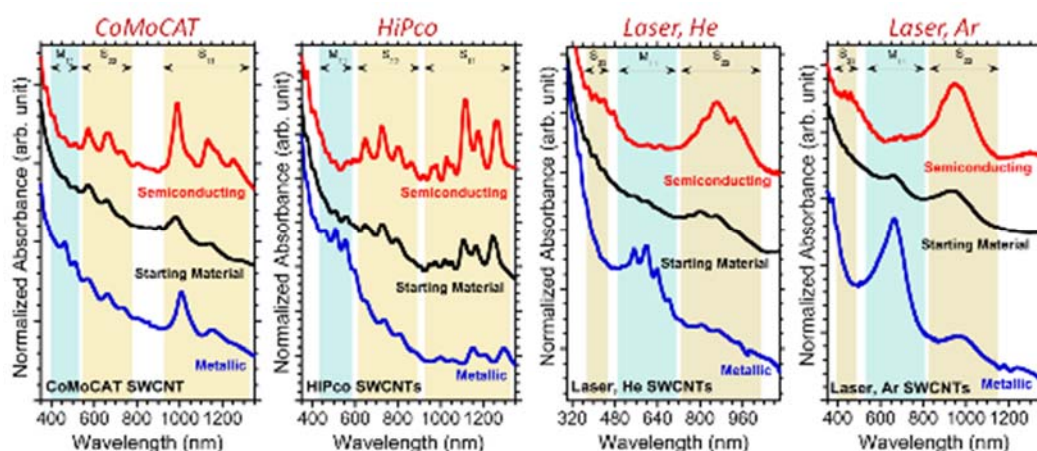


Figure 2. Optical absorption spectroscopy analysis of electronic-type-separated SWCNT samples produced at RIT as a function of synthetic technique (CoMoCAT, HiPco, and laser vaporization). The starting dispersion for each synthetic material is shown in black, while the separated M-SWCNT data is blue and S-SWCNT data is red.

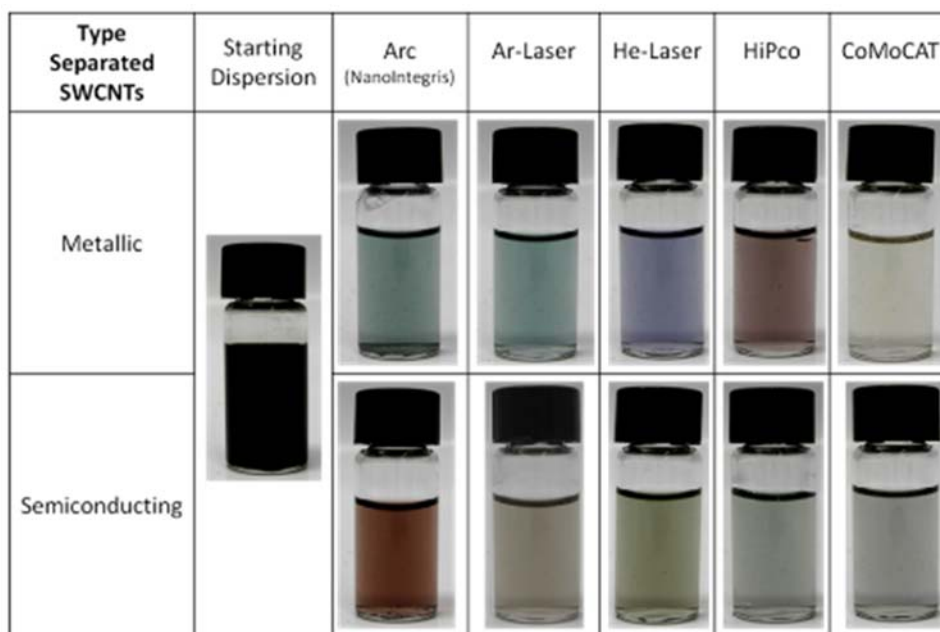


Figure 3. A photograph of each SWCNT synthetic material separated at RIT by electronic-type via column chromatography is presented and compared to the as-produced starting dispersion. Also presented are dispersions of M-SWCNTs and S-SWCNTs synthesized via arc discharge and separated at NanoIntegris via DGU method.

Column chromatography has provided a universal and scalable means to successfully separate SWCNTs based on electronic-type. By exploiting differences in the surface interaction of SDS and DOC with the SWCNTs, continued efforts have focused on refining the column chromatography process with the goal of achieving near mono-chiral fractions. To this end, the stationary phase composition and surfactant concentration were studied to evaluate their effect on separation efficacy. In-house synthesized laser-He SWCNTs were used in this analysis. The SWCNTs were again dispersed in 2.0 wt% SDS and prepared as described previously. The final dispersion was separated into two equivalent aliquots such that one could be separated on a column containing a stationary phase composed of Sepharose 2B and the other containing Sephacryl S200-HR. In both cases, the M-SWCNTs were eluted with 2.0 wt% SDS. Subsequently, DOC of varying concentration, ranging from 0.01 wt% to 2.0 wt%, was used to elute the S-SWCNTs and evaluate the ability of each to selectively solubilize narrow distributions of the S-SWCNTs. It was observed that only the 0.1, 0.5, and 2.0 wt% DOC caused an effect on the eluted S-SWCNT diameter distribution from the Sepharose column. Figure 4a shows that the largest diameter S-SWCNTs were eluted in the lowest concentration DOC, and the average diameter decreased with increasing DOC concentration (as seen by the blue shift in S-SWCNT peak position in the optical absorbance spectra with increasing DOC concentration). Interestingly, varying the DOC concentration during separation on the Sephacryl column did not have any effect on the diameter distribution of the S-SWCNTs eluted, and the majority of the S-SWCNT collected were in the 0.1 wt% DOC eluent. Figure 4b shows a comparison of the S-SWCNT fractions collected in 0.1 wt% DOC from the Sephacryl (red line) and Sepharose (blue line) columns, and demonstrates that there is a difference in the diameter distribution based on the stationary phase used. This improvement in the method demonstrates that fractions with narrower

diameter distribution can be achieved through optimization of the column chromatography method, and further refinement may lead to the separation of mono-chiral fractions.

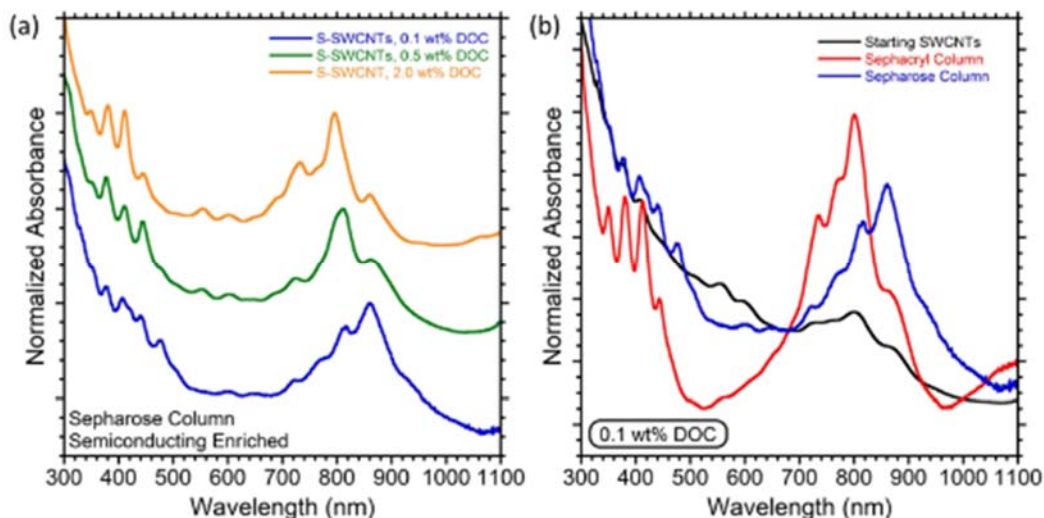


Figure 4. (a) Optical absorbance spectra of separated S-SWCNT fractions collected from a Sepharose column in different concentrations of DOC showing narrow diameter distribution. (b) Comparison of S-SWCNT fractions separated on sephacryl (red line) and sepharose (blue line) chromatography columns. All data was collected using laser-He SWCNTs as the starting material.

Analysis using fluorescence spectroscopy was performed on the S-SWCNT fractions described in Figure 4a to identify the specific chiralities present in each separated sample. Figure 5a shows the fluorescence map for the as-produced SWCNT sample prior to separation in 2.0 wt% DOC. By comparison, the S-SWCNT sample collected from the column in 0.1 wt% DOC (see Figure 5b) is nearly mono-chiral and contains predominately the (8,6) chirality. S-SWCNT fractions collected in 0.5 wt% DOC contain many of the same chiralities as the as-produced starting material (see Figure 5c), but appear to be enriched with the (8,6), (11,3), and (12,1) chiralities. Sample collected in 2.0 wt% DOC contained predominantly the (8,7), (9,5), and (10,5) chiralities (see Figure 5d). The results of the laser-He SWCNT separation using multiple concentrations of DOC are representative of the optimization to the chromatography method, and have been applied to the laser-Ar SWCNTs, as well as commercial HiPco and CoMoCAT materials, showing universality of the technique independent of the initial diameter distribution.

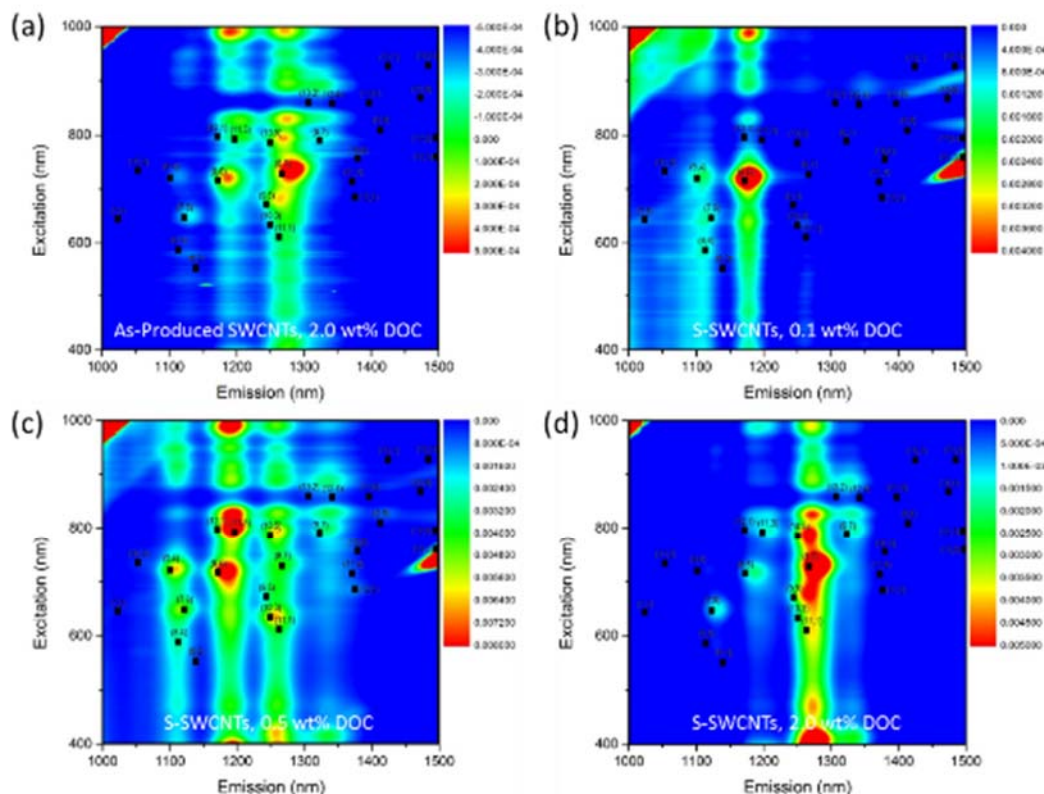


Figure 5. (a) Fluorescence analysis of the as-produced laser-He SWCNTs in 2.0 wt% DOC is used as a control to compare with the fractions collected after separation via column chromatography. Data for the S-SWCNT enriched fractions collected in (b) 0.1, (c) 0.5, and (d) 2.0 wt% DOC are also presented.

As an extension of the original column chromatography work, the “single-surfactant multicolumn gel chromatography” method, first proposed by Kataura *et al.*,⁴ was also investigated as a means to obtain mono-chiral SWCNT fractions. Much like the single column experiments, the columns were packed with an agarose gel stationary phase. Many small columns were then set up in series and the eluent from one was allowed to drip into the next. It is expected that due to the limited number of binding sites in each column, the SWCNTs are forced to organize in each column based on binding affinity to the stationary phase, so that when eluted each S-SWCNT fraction contains a single/narrow diameter distribution. SWCNTs were dispersed in 2.0 wt% SDS and applied to the first column, however, this technique relies on overloading the column, such that the ratio of SWCNTs to stationary phase by volume is in excess of 10x. Once the initial SWCNT dispersion had passed through all six columns, the series was disassembled and the bound S-SWCNTs were eluted from each column with 5.0 wt% SDS. One benefit to this method is the use of only a single surfactant, such that purification after separation is simplified. Figure 6 shows the results of the optical absorption spectroscopy for the S-SWCNT fractions collected. Although the fractions in general appear to be highly enriched in semiconducting SWCNT character, they also appear to contain multiple SWCNT chiralities. Thus, the multi-column chromatography does not provide mono-chiral fractions, or any appreciable difference compared to the single-column approach.

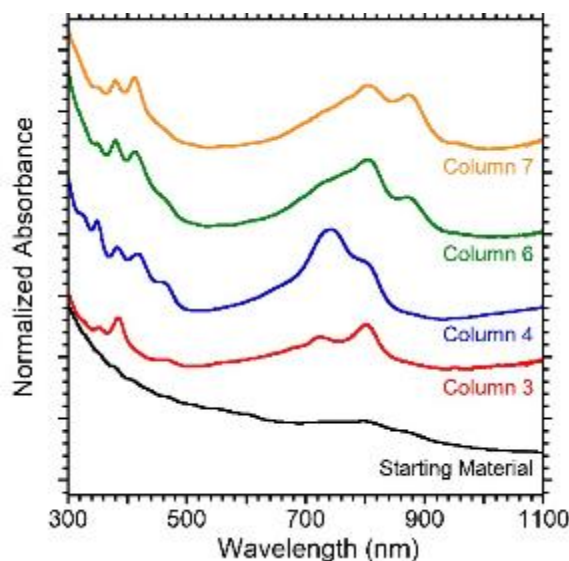


Figure 6. Optical absorption spectra for the S-SWCNT fractions obtained via separation using the “single-surfactant multicolumn gel chromatography” process.

In addition to column chromatography, RIT has investigated several recently reported SWCNT separation techniques, including selective dispersion with polyfluorene compounds. The selective dispersion method was originally proposed for the separation of large diameter, near armchair, semiconducting SWCNTs.⁵ This method was evaluated by dispersing in-house laser-Ar SWCNT soot in poly[(9,9-dihexylfluorenyl-2,7-diyl)-co-(9,10-anthracene)] (PFH-A) in toluene with a SWCNT soot concentration of 1 mg/mL. SWCNTs were dispersed using a combination of bath and horn ultrasonication (0.5 and 1 hour, respectively), and SWCNTs stabilized by the PFH-A were isolated via centrifugation (5k rpm, 1 hour). The separation efficacy was evaluated using optical absorption and fluorescence spectroscopy. The polymer selectivity for the SWCNTs was investigated by examining PFH-A concentrations between 0.5 to 4 mg/mL. There was no change in the chirality distribution dispersed by the PFH-A when using laser-Ar SWCNTs, and a 1 mg/mL polymer concentration was deemed optimal as it yielded high concentration SWCNT dispersions while minimizing the polymer loading. This technique was applied to the smaller diameter laser-He, HiPco, and CoMoCAT SWCNT synthetic-types. Figure 7a shows a representative absorbance spectrum for the separated laser-He sample compared to the as-produced reference sample in 2.0 wt% DOC. After separation using this selective dispersion technique, highly enriched S-SWCNTs are obtained. The absorbance data indicates that there is a more narrow S-SWCNT diameter distribution compared to the starting material, which was confirmed by analysis with fluorescence spectroscopy. The fluorescence map in Figure 7b demonstrates the selectivity of the PFH-A toward larger diameter SWCNTs, specifically the (8,7), (9,7), and (12,4) chiralities, compared to the as-produced starting material (see Figure 5a). In general, the PFH-A selective dispersion technique yielded highly enriched S-SWCNT samples with narrow diameter distribution for the CoMoCAT, HiPco, and laser synthetic materials, however, when applied to the larger diameter, arc-discharge SWCNTs, there was little to no selectivity and both metallic and semiconducting electronic-types were dispersed and stabilized by the polymer.

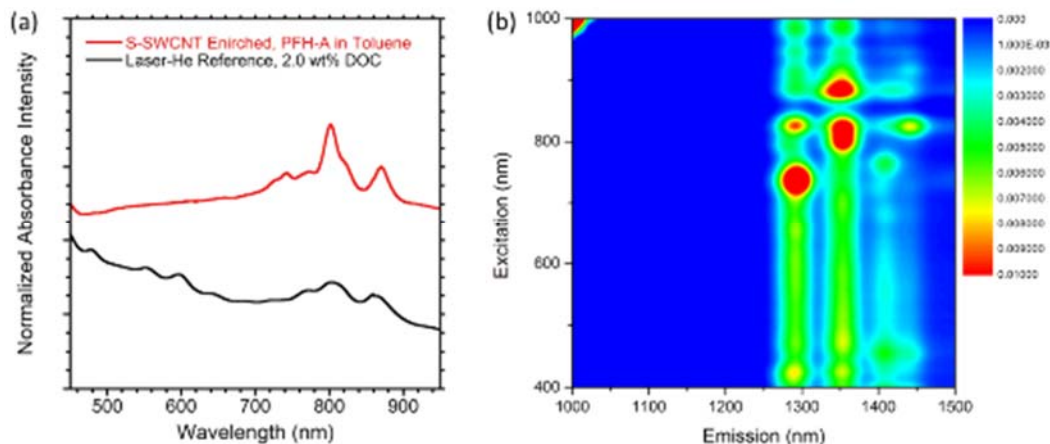


Figure 7. (a) Representative absorbance data for a S-SWCNT enriched sample separated via selective dispersion with PFH-A in toluene is compared to the as-produced reference material in 2.0 wt% DOC for the laser-He SWCNTs. (b) The S-SWCNT enriched sample is characterized by fluorescence spectroscopy to identify the specific chirality distribution in the sample.

Compared to column chromatography, the PFH-A selective dispersion provides a fast technique for the isolation of S-SWCNTs, with relatively narrow diameter distribution. However, the method (as published) creates significant SWCNT waste, and does not allow for the separation of highly enriched M-SWCNTs. Additional S-SWCNT material can be recovered by redispersing the pelleted material in fresh PFH-A/toluene and repeating the separation process without sacrificing enrichment. The ability to produce separated SWCNT materials across multiple synthetic types, diameters, electronic-types, etc. allows for the intrinsic radiation response of typical SWCNTs to be studied and exploited when incorporated into nanoelectronic devices (*i.e.*, TFTs, FETs, etc.) or macroscale devices (*i.e.*, advanced wires, cables, etc.).

1.3 Surfactant Removal From Separated SWCNTs

After separation, SWCNTs require purification to remove surfactants, polymers, etc. from processing, which ensures that the intrinsic properties of the SWCNTs can be probed in subsequent radiation studies. Using SDS as a model, a reagent-based surfactant removal technique has been proposed. A purified reference sample (P-SWCNT), having never been exposed to SDS, was quantified using optical absorbance spectroscopy, and found to be equivalent to a 100% pure reference sample.⁶ Thus, the P-SWCNT reference material is pure and can be used as a metric to compare the effects of residual surfactant and the efficiency of the proposed reagent-based surfactant removal method.

SEM analysis was also used as a qualitative measure of SWCNT purity. Figure 8a shows a representative micrograph of the P-SWCNT control sample, which clearly indicates that the SWCNT surface morphology is free from carbonaceous and metal catalyst impurities (typically appear as residual coating on SWCNTs or bright spots, respectively). The P-SWCNTs were subsequently dispersed in 2.0 wt% sodium dodecyl sulfate (SDS) using a combination of bath and horn ultrasonication. This process is used to mimic the exfoliation of SWCNT bundles into individualized SWCNTs stabilized by the surfactant used by many spectroscopy and/or separation techniques, as well as nanoelectronic device fabrication, and exposes the P-SWCNTs to typical surfactant environments and processing conditions. The

surfactant treated SWCNTs were recovered by vacuum filtration and rinsed with copious amounts of DI H₂O, and the reference material obtained will be referred to as SDS-SWCNTs from here on. SEM analysis of the SDS-SWCNTs (see Figure 8b) reveals that there is a residual surfactant coating on the SWCNTs, making them more difficult to identify. A second control sample was prepared, whereby P-SWCNTs were dispersed in DI H₂O (H₂O-SWCNTs) in the absence of surfactant using the same procedure to produce the SDS-SWCNTs. Characterization of the H₂O-SWCNT sample confirmed that the residue was related to the SDS and not an artifact of the processing conditions. Thus it can be concluded that the coating on the SDS-SWCNT sample is related to the residual surfactant and not carbonaceous impurities introduced during ultrasonication. While simple water washing alone removes the bulk SDS, the SEM analysis demonstrates that there is residual surfactant adsorbed to the SWCNT surface. In the present study, a reagent-based method is proposed, which allows for the isolation of pure SWCNTs and removes the residual surfactant surface coatings.

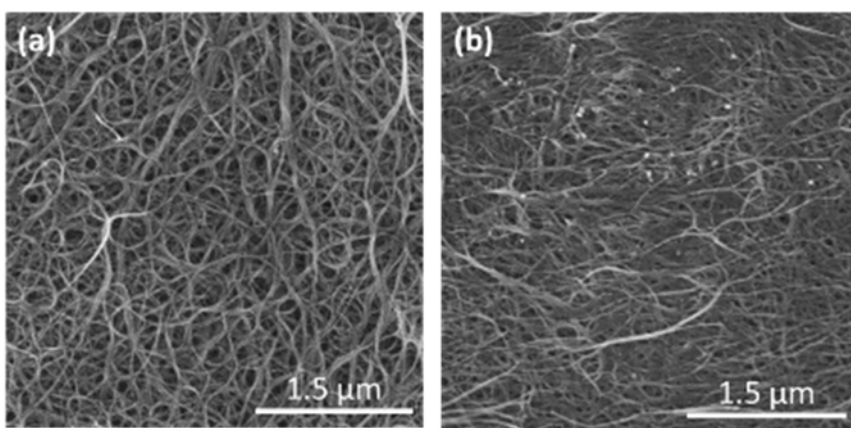


Figure 8. SEM analysis for the (a) P-SWCNT and (b) SDS-SWCNT (filtered from SDS and washed with copious amounts of DI H₂O) control samples.

The proposed reagent-based method was designed to interrupt the SWCNT:SDS interaction and allow for more efficient isolation of pure SWCNTs. A number of reagents were qualitatively surveyed by mixing equal volumes of P-SWCNTs dispersed in 2.0 wt% SDS with the desired reagent, including various acids, bases, organic solvents, and salts. Those reagents that interrupted the SWCNT:SDS interaction, yet did not change the solubility of the surfactant, were of great interest as these would allow the SWCNTs to be easily filtered from the bulk solution. Based on the qualitative analysis of approximately 20 reagents, five organic solvents yielded optimal results, including acetone, ethanol, N,N-dimethylacetamide (DMA), 1-cyclohexyl-2-pyrrolidone (CHP), and acetonitrile. Figure 9a and b show representative photographs of the initial SWCNT dispersion in 2.0 wt% SDS and the desired reagent interaction, respectively. Reagents were discarded from the study if they caused both the SWCNTs and SDS to precipitate, caused a color change, or did not affect the SWCNT:SDS interaction (see Figure 9c-e, respectively). The ratio of reagent to SWCNT dispersion was optimized so as to minimize the amount of solvent needed to precipitate the SWCNTs. Thus, further characterization of the acetone, ethanol, DMA, CHP, and acetonitrile treated SWCNT samples was conducted to quantitatively determine how efficient each reagent was toward removing residual SDS from the SWCNTs.

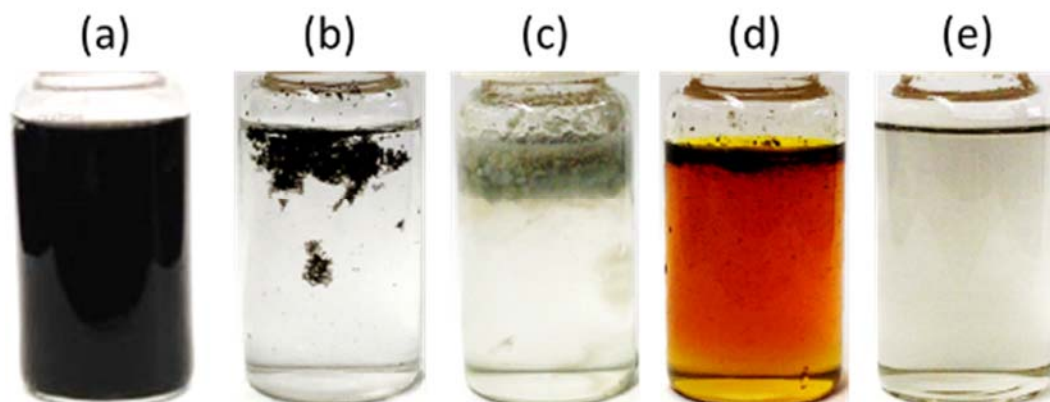


Figure 9. A photograph of (a) SWCNTs dispersed in aqueous 2.0 wt% SDS. Based on a qualitative screening of various acids, bases, organic solvents, and salts, a successful reagent will (b) interrupt the SWCNT:SDS interaction but not affect the solubility of the surfactant, whereas an unsuccessful reagent will (c) cause both the SWCNTs and SDS to precipitate, (d) cause a side reaction (indicated by color change), or (e) have no effect on the SWCNT:SDS interaction.

The purification process was scaled up so that SWCNT bulk papers could be fabricated after reagent treatment via vacuum filtration, with each sample containing 6 mg total SWCNT mass and an areal density of approximately 0.6 mg/cm^2 . The resulting SWCNT papers were rinsed with fresh solvent and dried in a vacuum oven at 100°C for 1 hr to remove residual solvent/moisture. An additional control sample was also fabricated using a previously reported procedure, whereby the SWCNT dispersion was mixed with 6M HCl and bath sonicated for 1 hr. The SWCNTs were subsequently filtered and redispersed in ethanol, then heated to 80°C for 1 hr.⁷ The treated SWCNTs (HCl-SWCNTs) were isolated and processed into a bulk paper via vacuum filtration. Compared to the SDS-SWCNTs, the proposed reagent treatment reduces both the filtration and total processing time by up to 99%. In particular, the acetone and acetonitrile treatments reduced processing time from nearly 6 hr, for the SDS-SWCNT control, to less than 0.1 hr. Although slightly longer than the ACT- and ACN- treatments, the EtOH-, DMA-, and CHP- treatments yielded total processing times between 0.5 – 1 hr, which is $\geq 82\%$ improvement compared to the SDS-SWCNT control sample. It is important to note that filtration and processing times will vary based on the sample volume, membrane pore size, etc., however, these relative times are intended to demonstrate that in addition to aiding in purification, the reagent treatments also significantly reduce processing times, thus enabling more efficient, large-scale SWCNT isolation from SDS dispersion.

The purity of the reagent treated samples was quantified relative to the P-SWCNT and SDS-SWCNT control samples using a combination of microscopy and spectroscopy. Representative SEM micrographs are shown in Figure 10 for the six reagent treated samples. In general, the SWCNT morphology is apparent with no obvious surfactant coating for all reagent treated samples, and appears to be similar in all cases to the P-SWCNT control. With the exception of the ACT-SWCNT sample, the bundle size appears to increase (at least on the surface) compared to the P-SWCNT sample. This qualitative analysis demonstrates that the reagent treatment is effective compared to traditional water washing, however, additional characterization is required to determine the purity of the SWCNTs and whether any residual SDS remains.

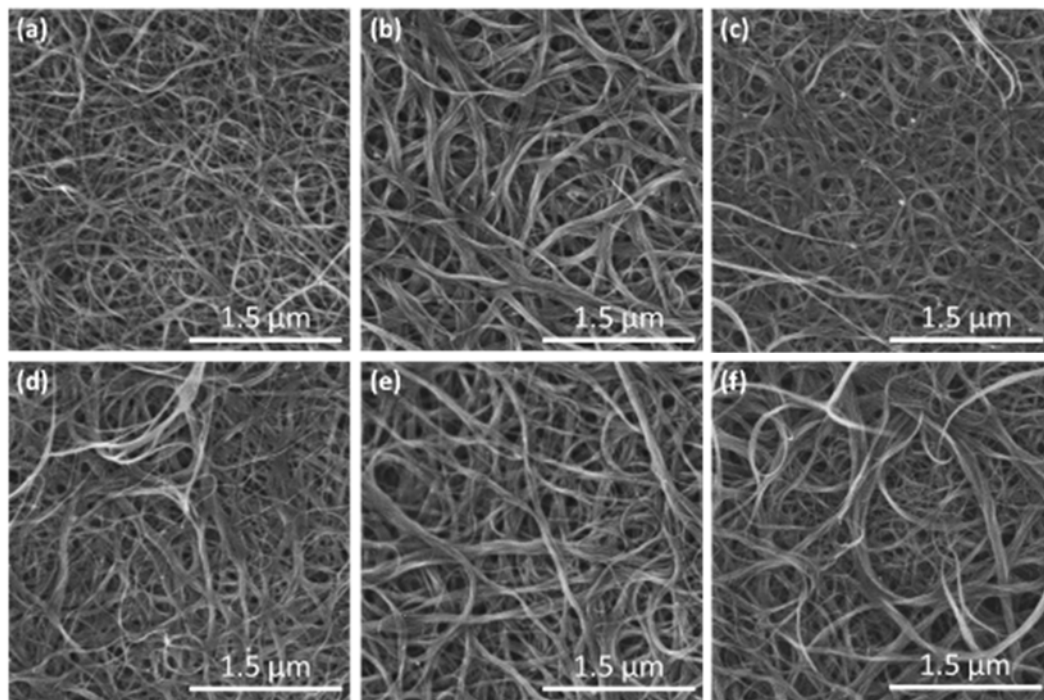


Figure 10. Qualitative SEM analysis of the as-produced (a) ACT-, (b) EtOH-, (c) DMA-, (d) CHP-, (e) CAN-, and (f) HCl-SWCNT samples.

Thermogravimetric analysis (TGA) was performed to assess the decomposition characteristics of the reagent treated SWCNT samples compared to the P-SWCNT control. Approximately 0.5 mg of each SWCNT sample was used to ensure consistency between measurements, and TGA was performed using a ramp rate of 10°C/min in air (20 mL/min flow rate). Analysis of neat SDS shows the rapid decomposition at ~200°C and a residual mass of 23%. By comparison, the SDS-SWCNT sample also shows a decrease in the SWCNT decomposition temperature to 513°C compared to the P-SWCNT control (640°C). The decrease in decomposition temperature in the SDS-SWCNT sample indicates the presence of residual surfactant, as does the small decomposition peak ~200°C, which matches that of neat SDS. The reagent treated samples were also characterized using TGA, and the results of the weight loss and first derivative weight loss are shown in Figure 11a and b, respectively. In all cases (except CHP-SWCNT), the maximum decomposition temperature is increased above that of the SDS-SWCNT sample toward that of the P-SWCNT control. It is difficult to distinguish whether the low temperature decomposition is from residual SDS or amorphous carbon impurities from processing, and is most likely a combination of both. After the initial TGA characterization was complete, the as-produced reagent treated samples were subjected to a thermal oxidation treatment in air to 520°C (ramp/stop at 10°C/min). Figure 11c and d show that the decomposition temperature of the SWCNT samples increases after thermal oxidation, and the impurities, which were observed at decomposition temperatures below 450°C, are removed. Although thermal oxidation produced improvement for all samples, the SDS-SWCNT sample continues to exhibit the lowest decomposition temperature (530°C) compared to the P-SWCNTs, and the reagent treated samples show increasing decomposition temperatures in order of ACT- (544°C) < EtOH- (552°C) < CHP- (567°C) < DMA- (582°C) < HCl- (584°C) < ACN- (592°C) SWCNTs. Thus, based on TGA analysis alone, thermal oxidation aids in SWCNT

purification, however, the results are most improved with the additional use of the reagent treatments. From this analysis, the acetonitrile treatment appears to be the most effective at removing residual SDS and produces a SWCNT sample most closely matched to the P-SWCNT control (640°C).

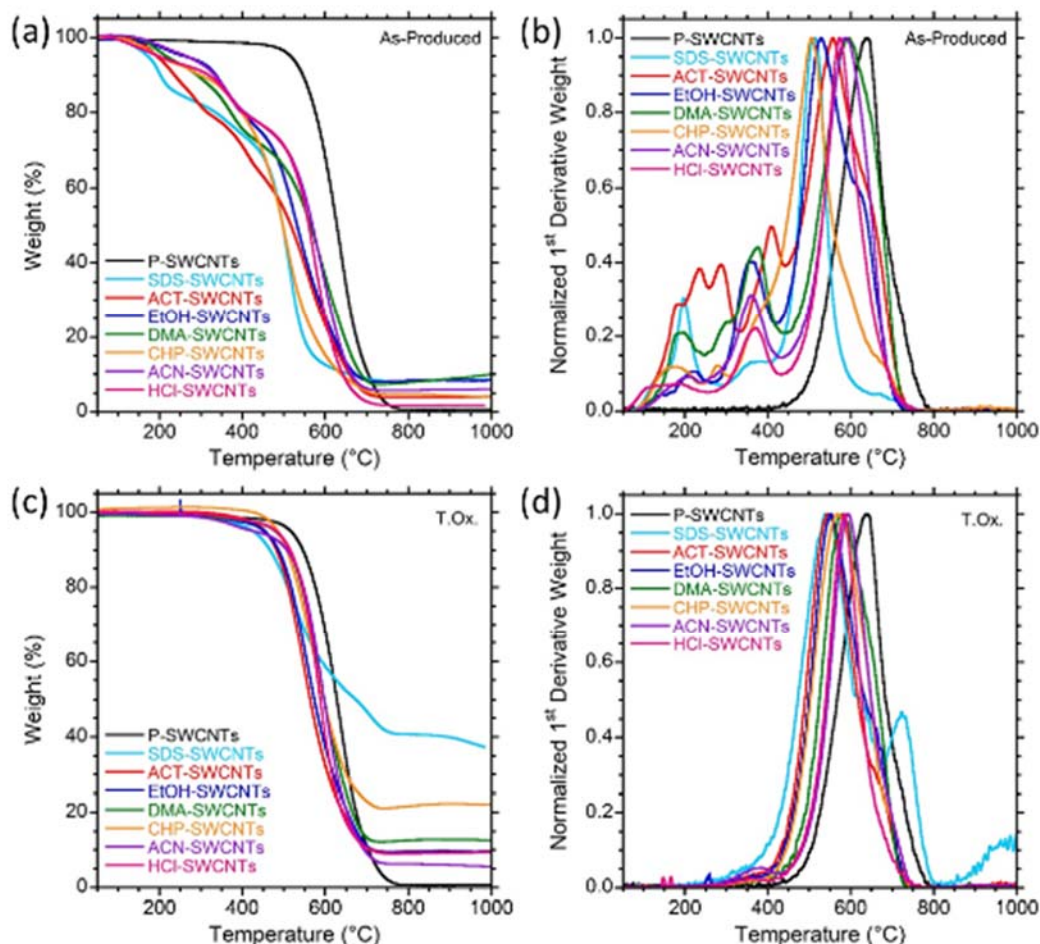


Figure 11. Thermogravimetric analysis (TGA) results of the (a) weight loss and (b) first derivative weight loss for the as-produced reagent treated samples are shown as a function of temperature. The samples were thermally oxidized in air to 520°C, and the analysis for (c) weight loss and (d) first derivative weight loss were repeated.

Raman spectroscopy was used to probe the quality of the treated SWCNT samples. In particular, Figure 12a shows a close-up examination of the relative Raman G peak. Compared to the P-SWCNT control, the SDS-SWCNT sample exhibits a significant suppression of the BWF line shape. In general, recovery in the G peak line shape is observed after reagent treatment, though some suppression is still observed in comparison to the P-SWCNT control. The as-produced samples were subsequently subjected to thermal oxidation. Figure 12b shows that the BWF is nearly fully recovered after reagent treatment and thermal oxidation for all samples. The extent of recovery after reagent treatment and thermal oxidation was evaluated by measuring the full width at half maximum (FWHM). As shown in Figure 12c, the P-SWCNT control has a FWHM of 128.1 (see dashed reference line). Exposure to SDS causes a reduction in the FWHM of the SDS-SWCNT sample to

85.8. While reagent treatment improves the FWHM (solid markers) in general, the ACT-SWCNT sample exhibits the most improvement, with a FWHM of 120.1. After thermal oxidation (open markers), all samples exhibit nominally the same FWHM within standard error, and have an average value of 120.4. Likewise, the G' peak position is affected by the presence of residual SDS, which manifests as an upshift in frequency compared to the P-SWCNT control. Figure 12d demonstrates that after reagent treatment the G' peak position is down-shifted toward that of the P-SWCNT control, with the greatest improvement observed for the ACT-SWCNT sample (2623.1 cm^{-1} compared to 2624.5 cm^{-1} , respectively). Figure 12e shows that the G' peak position of the remaining reagent treated samples is recovered after the addition of a thermal oxidation treatment. The results of this analysis are summarized in Figure 12f, which demonstrates that after thermal oxidation, the reagent treated SWCNTs have a G' peak positions that fall within $\pm 0.2\%$ of the P-SWCNT control. Thus it can be concluded from the Raman analysis, that the reagent treatment yields purity comparable to the P-SWCNT control, and the acetone and acetonitrile reagents continue to emerge as the most efficient at disrupting the SWCNT:SDS interaction.

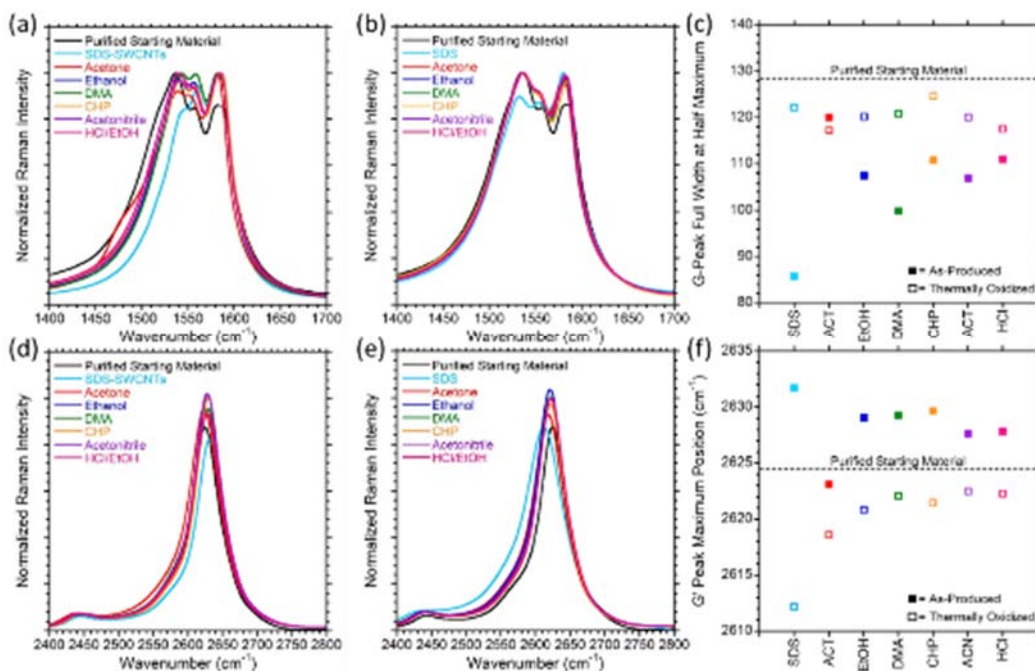


Figure 12. Analysis of the relative Raman G peak for the (a) as-produced and (b) thermally oxidized reagent treated samples compared to the P-SWCNT control (black curve). (c) The G peak FWHM was analyzed for the as-produced (solid markers) and thermally oxidized (open markers) samples and compared to the P-SWCNT control (dashed line). Characterization of the Raman G' peak was also conducted for the (d) as-produced and (e) thermally oxidized reagent treated samples. (f) Analysis of the G' peak position was conducted and compared to the P-SWCNT control (dashed line). All data was normalized to the G peak maximum intensity for each sample.

The electrical conductivity of the as-produced and thermally oxidized samples were evaluated and compared to the P-SWCNT control sample. As shown in Figure 13, the presence of the residual SDS increases the conductivity of the SDS-SWCNT sample by $\sim 7.4\times$ compared to the P-SWCNT control, acting as a dopant. Although this can be useful in some applications, it can also be used as a metric to assess purification efficacy of the reagent treated samples. In general, there is a decrease in the electrical conductivity of the as-produced reagent treated samples compared to the SDS-SWCNTs, however, the electrical

conductivity is still greater than that of the P-SWCNT control. The one exception to this, is for the ACT-SWCNT sample, which has an electrical conductivity of 4.23×10^4 S/m, compared to 2.11×10^4 S/m for the P-SWCNT control. After thermal oxidation, the electrical conductivity of all reagent treated samples fall to within $\pm 50\%$ of the P-SWCNT control value. This further demonstrates that the reagent treatment coupled with thermal oxidation produces the greatest improvement in purity after exposure to SDS, and that thermal oxidation alone does not purify the SWCNTs of SDS as efficiently without the use of the reagent treatment.

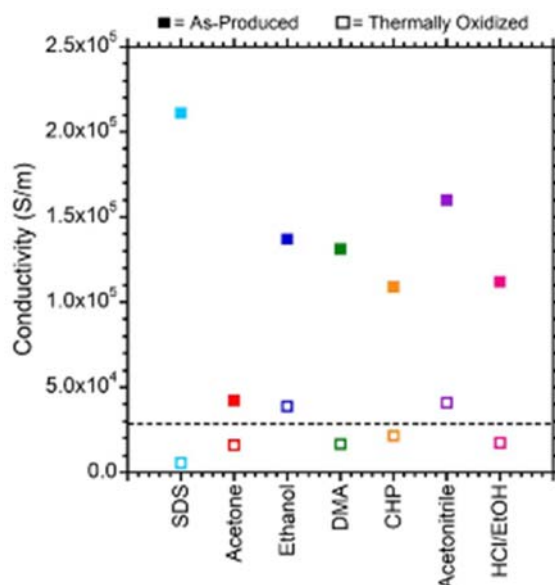


Figure 13. Electrical conductivity was evaluated for the as-produced (closed markers) and thermally oxidized (open markers) SDS-SWCNT and the reagent treated SWCNT samples compared to the P-SWCNT control (dashed line).

Based on the results of the TGA, Raman, and electrical analysis, the acetone and acetonitrile treatments emerge as the most efficient for SDS removal from SWCNTs. Thus, these samples were analyzed with X-ray photoelectron spectroscopy (XPS) to determine how much surfactant remains after treatment. The P-SWCNT control showed no evidence of Na or S present, thus, the XPS results were compared to the SDS-SWCNT sample. Figure 14a lists the atomic percentage of Na, O, C, and S for each of the as-produced reagent treated samples. Based on this analysis, the acetone (acetonitrile) sample shows a decrease in Na, O, and S to 5.6% (11.2%), 7.8% (12.7%), and 45.2% (41.9%) of the SDS-SWCNT content. XPS was also conducted after the thermal oxidation treatment. Figure 14b – d shows the raw XPS data for the O, S, and Na trace respectively, for the P-, SDS-, ACT, and ACN-SWCNTs. Although the data has not yet been analyzed to determine the atomic percentage of each element present, the data does demonstrate that the SDS-SWCNT sample contains a significantly higher amount of O, S, and Na compared to either of the reagent treated samples. Likewise, the ACT-SWCNT sample appears to contain less of each element compared to the ACN-SWCNT sample, thus indicating increased purity. The analysis presented herein, demonstrates that reagent treatment in conjunction with thermal oxidation provides a simple and efficient means to remove SDS from large-scale quantities of

SWCNTs, and enables a method for the intrinsic SWCNT properties to be investigated after surfactant processing.

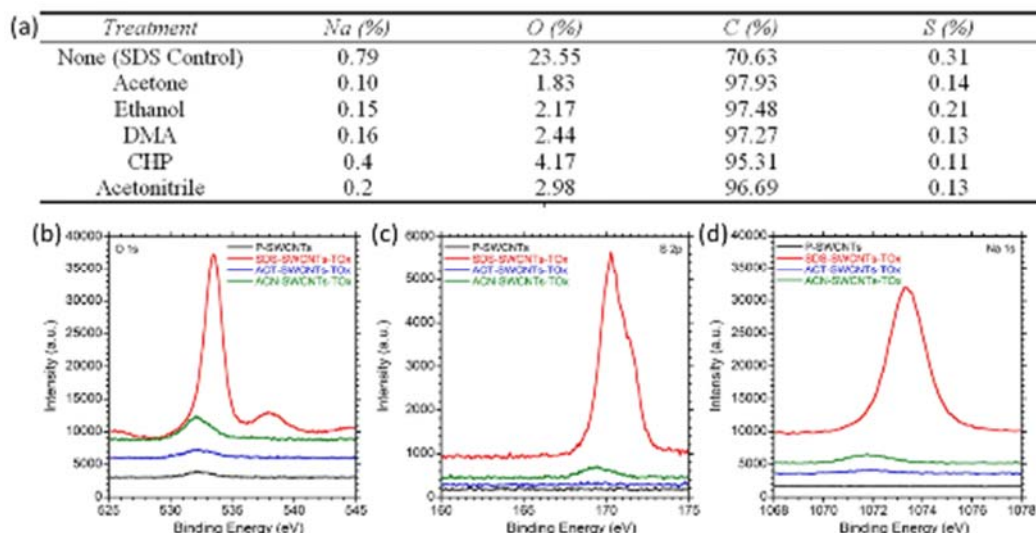


Figure 14. (a) The table lists the atomic percentages of Na, O, C, and S for the as-produced reagent treated samples compared to the SDS-SWCNT control determined by XPS. The raw XPS data for (b) O, (c) S, and (d) Na are given for the P-SWCNTs, as well as the SDS-, ACT-, and ACN-SWCNTs after reagent treatment and thermal oxidation.

2. Radiation Testing of SWCNTs

2.1 Displacement Damage Dose Effects as a Function of SWCNT Electronic-Type

Displacement damage does (DDD) effects in SWCNT thin-films were systematically studied using ion irradiation and two incident ions. Metallic (M-) and semiconducting (S-) SWCNT thin-films were prepared using commercially available electronic-type-separated SWCNTs from NanoIntegris. A Varian-350D medium current ion implanter was used to irradiate the SWCNT thin-films with either 150 keV $^{11}\text{B}^+$ or 150 keV $^{31}\text{P}^+$ with fluences ranging between 10^{12} to 10^{15} ions/cm². Each thin-film sample was irradiated iteratively *in vacuo* (25°C, 1×10^{-6} Torr) with logarithmically increasing fluences. After ion irradiation the SWCNT thin-films were allowed to equilibrate in air for 1 hr prior to characterization by Raman spectroscopy and 4-point probe electrical measurements using the van der Pauw method. Although a color change is observed from green (red) in the M-SWCNT (S-SWCNT) thin-film to grey after ion irradiation, atomic force microscopy demonstrates that there is little to no difference in the structural morphology.⁸ Therefore, structural changes in the isolated metallic and semiconducting SWCNT thin-films were monitored after each successive irradiation using Raman spectroscopy. Several general trends were observed from this analysis, specifically, the monotonic decrease in the G and G' band peak intensities, and the initially increasing D band peak intensity. The maximum D band intensity was observed at 5×10^{13} ions/cm² (5×10^{12} ions/cm²) for $^{11}\text{B}^+$ ($^{31}\text{P}^+$), after which point the absolute peak intensities for the D, G, and G' bands all decreased.⁸ Despite differences in the relative peak intensities and the rate in which they change, the metallic and semiconducting SWCNT thin-films both exhibited D and G band broadening after the final total dose was imparted to the sample, and the G' band disappeared below the noise floor, independent of the incident ion used to irradiate the SWCNT thin-films.

The quality of nanostructured carbon materials is typically measured using the ratio of peak intensities of the D and G bands. In the current study, analysis of the D/G and D/G' Raman ratios were employed to study the SWCNT thin-films after ion irradiation. In both cases, a greater slope is observed in samples irradiated with $^{31}\text{P}^+$, indicating a greater damage rate. Perhaps most interesting is the fact that the D/G' ratio is an indicator roughly one order of magnitude more sensitive to structural changes compared to the D/G ratio. Differences in the damage rates between the two incident ions relate to the 10x greater non-ionizing energy loss (*NIEL*) of $^{31}\text{P}^+$ compared to $^{11}\text{B}^+$. The product of the *NIEL* and the fluence yields the displacement damage dose (*DDD*), which is damage source and material independent, and provides a means to assess results from ion irradiation with both $^{11}\text{B}^+$ and $^{31}\text{P}^+$ in the electronic-type-separated SWCNT thin-films. Although the onset of structural deformation was observed at a fluence one order of magnitude lower in the $^{31}\text{P}^+$ ion irradiation experiments compared to $^{11}\text{B}^+$, the data collapse to form a general trend when plotted against *DDD*. This indicates that there are no significant differences in the stability of the SWCNT thin-films based on the electronic-type.

Changes in the sheet resistance (R_s) of the electronic-type-separated SWCNT thin-films were also monitored after each successive ion irradiation. This compliments the data obtained by Raman spectroscopy and allows for the relationship between the bulk electrical transport and localized structural modifications to be inferred. Examination of the electrical properties as a function of fluence shows a monotonic increase in R_s with increasing fluence, independent of the incident ion used to irradiate the samples or the electronic-type of the SWCNT thin-film. Again the onset of change is one order of magnitude lower for samples irradiated with $^{31}\text{P}^+$ compared to $^{11}\text{B}^+$, consistent with the observed Raman data. The normalized R_s was also analyzed as a function of *DDD*, and the data collapse to a similar trend independent of the incident ion used to irradiate the samples. Therefore, the increase in R_s is correlated with structural modifications induced by ion irradiation in the electronic-type-separated SWCNT thin-film samples.

The change in R_s that occurs in the M-SWCNT and S-SWCNT thin-films in response to increasing *DDD* correlate strongly with the morphological changes observed in the D/G' ratio (Figure 15a). *DDD* is the total energy imparted to the material that results in the formation of vacancies, and therefore, is directly proportional to the *number of vacancies created*. While these effects can be studied more precisely using molecular dynamics (MD) simulations, the low energy ions used in the current study are expected to produce only single and dual vacancies,⁹ and the results of MD simulation data averaged over many particle histories often agree well with the closed form *NIEL/DDD* results.^{10, 11} Additionally, as the defect density increases with increasing fluence, the changes in mobility of the SWCNT thin-film samples can be inferred from Mattheissen's rule. In many materials, a linear degradation in mobility is observed with increasing *DDD*,^{12, 13} making it possible to mathematically describe the relative change in R_s and D/G' with *DDD*, as shown in Eq. 1:

$$\frac{R_s}{R_{s,0}} = \frac{D/G'(\Phi)}{D/G'(0)} = f(DDD) = A \left(1 + \frac{DDD}{D_x} \right) \quad (1)$$

Where D_x is the characteristic damage level to reach a doubling in resistance. The dashed black line in Figure 15a is the least squares curve fit of all R_s and D/G' values using Eqn. (2).

Agreement is good for all normalized R_s values indicating the assumed linear mobility degradation with DDD is appropriate.

Additionally, using the modified Kinchin-Pease formula, and accounting for the binding energy, $E_b = 3$ eV, the number of vacancies per unit mass of SWCNT, V_m , is obtained by dividing DDD by the energy required to produce a vacancy $E_{vac} = \left(\frac{E_{th}}{0.4} + E_b\right)$, where the threshold energy, E_{th} , is the minimum energy to create a vacancy in a SWCNT. Ion irradiation results in the formation of vacancies randomly throughout the thin-films; however, the underlying 1D nature of the SWCNTs confines every vacancy to a single SWCNT within the 3D thin-film volume. From this alternative perspective, the DDD (and vacancies per unit mass) can be related to the number of vacancies per unit length of a SWCNT using the following equation:

$$V_L = \frac{DDD m_L}{E_{vac}} \quad (2)$$

where $m_L = \frac{W_C N_c}{l_c}$ is the SWCNT mass per unit length, W_C is the atomic weight of carbon, N_c is the number of atoms per circumferential unit cell around a SWCNT, and l_c is the length of the circumferential unit cell. The inverse of the V_L ($L_v \equiv V_L^{-1}$) is defined as the inter-vacancy length, which describes the average length between adjacent vacancies along the SWCNT. L_v is the sought-after parameter since it is related to the mean free path for carrier transport along the SWCNT length, assuming all vacancies on the circumference of the SWCNT effect transport and contribute to the Raman spectra equally. To provide some perspective, a number of vacancy-free (10,10) armchair SWCNT segments are illustrated in Figure 15b and correspond to the appropriate DDD . The (10,10) SWCNT has a diameter of ~ 1.35 nm, which falls near the mean diameter for the NanoIntegris materials used to construct the thin-film samples, and the values of l_c and N_c are 1.23 \AA and 20, respectively. The longest defect-free segment corresponds with a DDD value of 10^{15} MeV/g and has an associated R_s and D/G' that are essentially unchanged from the pre-irradiation values. This suggests that the effective pre-irradiation defect-free length is ~ 20 nm; some of the initial defects may be substrate induced or result from SWNCT-SWCNT interactions. With increasing DDD , R_s and D/G' increase considerably and the corresponding L_v shortens down to effectively one circumferential unit cell at a $DDD \sim 10^{17} \text{ MeV/g}$. At these very short distances, the "length" has little meaning and therefore the corresponding number of carbon atoms containing one vacancy are also displayed.

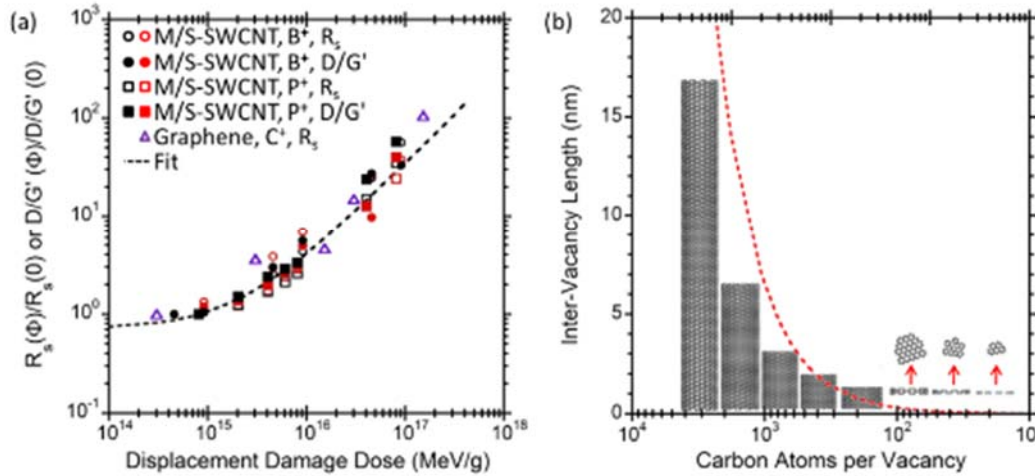


Figure 15. (a) The relative R_s and D/G' for M- and S-SWCNT thin-films are plotted as a function of DDD after ion irradiation with logarithmically increasing fluences of 150 keV $^{11}\text{B}^+$ and $^{31}\text{P}^+$. The data is described well by a fit with $f(DDD)$, as described in Eq. 1. (b) The degradation in the relative R_s and D/G' is described by the inter-vacancy length (L_v), and is represented by a series of vacancy-free (10,10) SWCNT renderings. Figure taken from Ref. 8.

Thus, changes in the bulk electrical transport properties of these materials have been directly related to the localized structural modifications induced by ion irradiation. Ultimately, a decrease in the effective vacancy-free length with increasing fluence causes changes in the percolation network, which affects the structural integrity and electrical transport properties in the nanostructured carbon thin-films. When analyzed as a function of DDD , the D/G' ratio and R_s collapse to form a near singular master curve, independent of the graphitic nature of the sample, or ionic species used to irradiate it (assuming the incident ion has low-energy recoil spectra). From this analysis, a clear trend has emerged, which directly relates modifications in electrical transport characteristics to the morphological changes observed in the Raman D/G' ratio for M-SWCNTs, S-SWCNTs (of equivalent diameter distribution), and graphene. As such, a universal model has been developed whereby the radiation response of any nanostructured carbon material can be predicted based upon L_v .

2.2 Displacement Damage Dose Effects as a Function of SWCNT Diameter Distribution

The effect of ion irradiation in thin-films of electronic-type separated SWCNTs has shown that the variation in vacancy density can be described using an empirical model based on an inter-vacancy length (L_v), which directly correlates relative Raman ratios to bulk electrical transport for ion-irradiated SWCNTs. These results showed similar stability of SWCNT thin-films based on electronic-type (*i.e.*, metallic vs. semiconducting) for equivalent diameter distribution under identical ion irradiation conditions.⁸ It was shown that the radiation response can be compared in terms of DDD , thus, a representative ion condition can be used to develop a fundamental understanding of how the SWCNT optoelectronic properties vary with ion irradiation and SWCNT structure (diameter and chirality). SWCNTs with varying diameter distribution arising from specific synthetic methods (*i.e.*, CVD and laser vaporization) were selected to probe the changes in material properties as a function of radiation exposure. Thin-films were fabricated using CoMoCAT SWCNTs (purchased from SWeNT) and SWCNTs synthesized in-house via laser vaporization in either helium (laser-He) or argon (laser-Ar) carrier gas. Comparison of the optical absorption spectra for each

SWCNT thin-film (see Figure 16a) shows a characteristic red shift in the peak position of the E_{11}^M , E_{22}^S , and E_{11}^S transitions due to quantum confinement for increasing SWCNT diameter (d_t), and illustrates the differences between the CoMoCAT sample (smallest diameter distribution) to the laser-Ar sample (largest diameter distribution). Similarly, spectra for the Raman radial breathing mode (RBM) are shown in Figure 16b, where the SWCNT d_t is inversely proportional to the peak position. The SWCNT d_t for each prominent peak is labeled on the plot, and illustrates the range of diameters for CoMoCAT (0.7 – 0.9 nm), laser-He (1.0 – 1.2 nm), and laser-Ar (1.2 – 1.6 nm) used in the current study. Thus, the sample set spans the typical SWCNT diameters that are used in advanced applications, and provides sufficient diameter differences to understand fundamental effects from radiation exposure.

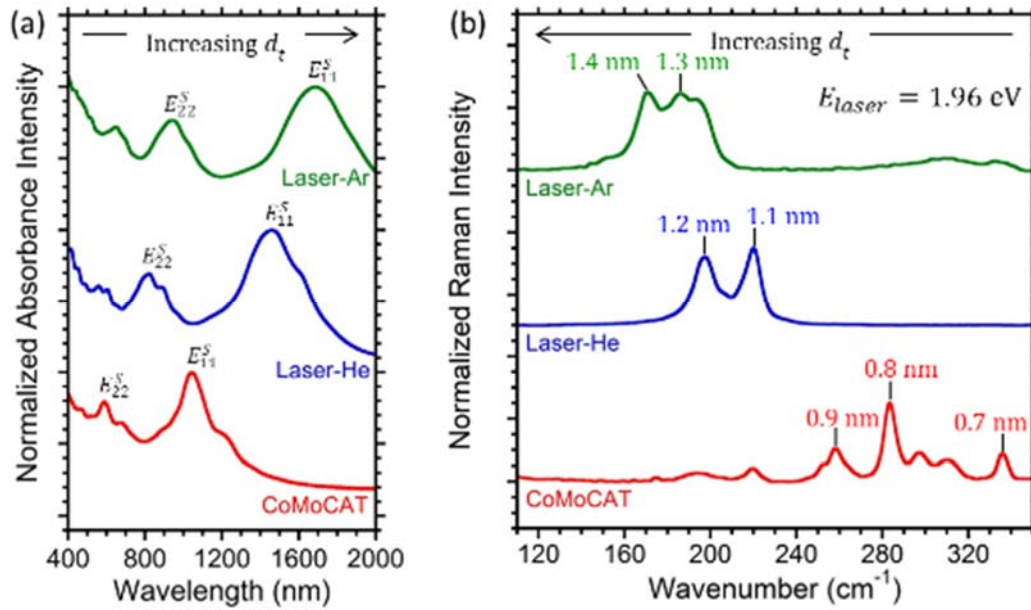


Figure 16. (a) Optical absorption spectra for the CoMoCAT, laser-He, and laser-Ar SWCNT thin-films are provided. The E_{11}^S and E_{22}^S peaks are labeled on each spectrum to demonstrate the difference in SWCNT diameter (d_t). (b) The Raman radial breathing mode (RBM) is shown for each thin-film sample, and the average d_t for each prominent peak is indicated on the spectra to highlight the distribution of diameters examined in the present study. Figure taken from Ref. 14.

SWCNT thin-film samples with similar thicknesses were prepared (equivalent areal mass densities of $17 \pm 2 \mu\text{g}/\text{cm}^2$) and transferred onto polished quartz wafers. The SWCNT mass in each sample was controlled so that changes as a function of diameter distribution could be systematically monitored. The samples were irradiated *in vacuo* (1×10^{-6} Torr) with 150 keV $^{11}\text{B}^+$ using a Varian 350D Medium Current Ion Implanter at $\sim 25^\circ\text{C}$ by rastering the beam uniformly across a 196 cm^2 area with a fixed beam current of $10 \mu\text{A}$. Optical density of the SWCNT thin-film samples was sufficient to for optical absorption spectral monitoring as a function of radiation exposure. Suppression of the characteristic metallic and semiconducting SWCNT peaks and an increase in the background intensity as the fluence increases is observed for all samples. Analysis of the ratio of the E_{11}^S peak intensity compared to the minimum baseline intensity (between the E_{11}^S and E_{22}^S peaks) illustrates that the rate of absorbance suppression increases with increasing SWCNT d_t . At a fluence of

approximately 2.5×10^{14} ($^{11}\text{B}^+$)/ cm^2 , the characteristic SWCNT electronic transitions are no longer prominent in the absorbance spectra for any of the thin-film samples, signifying an important structural state resulting from the number of defects in the SWCNTs.¹⁴ Thus, optical absorption spectroscopy, as an ensemble measurement for SWCNTs, has been shown to be greatly affected by the presence of defects, which influences the inherent oscillator strength due to changes in the number of available optically-active states.

Raman spectroscopy was performed after each successive irradiation to probe the localized structural modifications of the SWCNTs caused by ion irradiation. All samples exhibit a monotonic decrease in the G and G' band intensities in response to increasing fluence (although at different rates), while the D band peak intensity increases, consistent with results observed after ion irradiation of electronic-type-separated SWCNT thin-films.⁸ At a fluence of 2.5×10^{14} ($^{11}\text{B}^+$)/ cm^2 , the Raman peak intensities are dramatically decreased compared to the respective pre-irradiated sample for each synthetic-type. This is the same fluence where near complete suppression in the absorption data is observed, and illustrates the influence that absorption has on the resonant enhancement of the SWCNT Raman spectra. At fluences greater than 2.5×10^{14} ($^{11}\text{B}^+$)/ cm^2 , the G' band and RBM are not prominent above the noise floor, and the D and G bands begin to exhibit peak broadening. As radiation exposure increases to 1.0×10^{15} ($^{11}\text{B}^+$)/ cm^2 , the Raman spectra indicate that highly defective SWCNTs display similar character to nanostructured carbon,¹⁵ however, SEM analysis shows the nanotube morphology is still intact. Thus, the SWCNT optical properties are directly affected by the vacancy density, and the Raman G-band intensity is shown to correspond linearly to the suppression of E_{11}^S in optical absorbance.¹⁴ Analysis of the D/G' with increasing fluence for each of the SWCNT thin-film samples was conducted to examine selective structural changes as a function of SWCNT diameter distribution. Figure 17a illustrates the normalized D/G' for the CoMoCAT, laser-He, and laser-Ar SWCNT thin-film samples after each successive ion irradiation with 150 keV $^{11}\text{B}^+$. The normalized D/G' increases with fluence for all SWCNT samples, and the rate of increase shows a strong dependence on the SWCNT diameter distribution. A similar diameter dependence is observed in the normalized D/G. Thus, the smaller diameter SWCNTs have a consistently lower D/G' and D/G at equivalent fluences, suggesting *fewer defects per nanotube*.

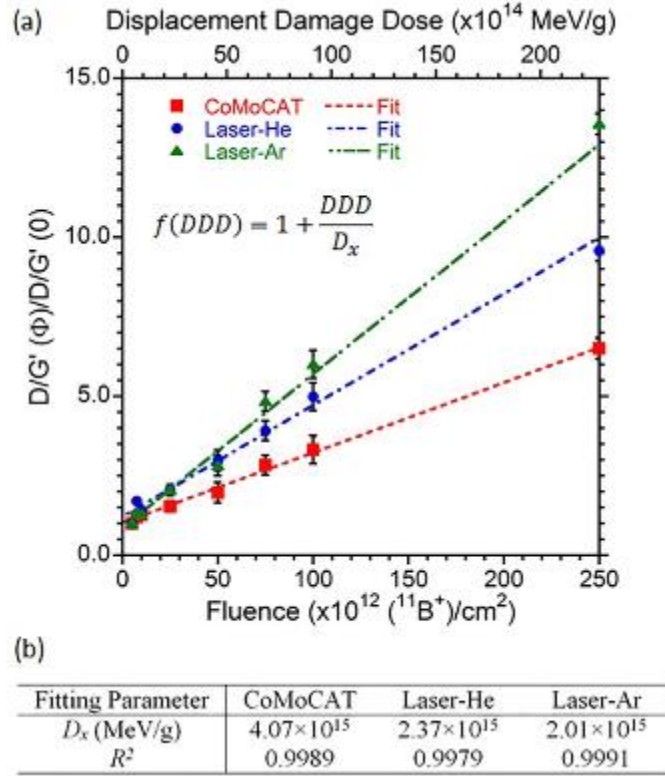


Figure 17. (a) Analysis of the normalized D/G' Raman ratio for SWCNT thin-films of varying synthetic-type and diameter distribution is shown as a function of fluence and displacement damage dose (DDD). The empirical data is fit with the inset functional form using the linear least squares method (dashed lines). (b) The table lists the A and D_x fitting parameters for each SWCNT thin-film sample. The coefficients of determination (R^2 values) are also provided to demonstrate the goodness of fit. Figure taken from Ref. 14.

An established approach to compare different radiation experiments is to convert the experimental fluence into displacement damage dose (DDD) by taking the product of the fluence and the non-ionizing energy loss (NIEL),¹⁶ and is directly proportional to the vacancy density within the samples. Assuming a displacement threshold energy (E_d) of 20 eV and a density of 0.5 g/cm³, the effective non-ionizing energy loss ($NIEL_{eff}$) for 150 keV $^{11}\text{B}^+$ is 91.2 ± 2 MeVcm²/g based on WinNIEL calculations for B^+ in a carbon film.¹⁶ Figure 17a provides the normalized D/G' as a function of DDD on the second x-axis. The data are fit using a linear least squares method with the inset equation¹⁶ provided in Figure 17a. The dashed lines represent the resulting curve fits, and excellent agreement with the data is observed. The D_x fitting parameter and coefficient of determination (R^2 values) for each sample are provided in the table shown in Figure 17b. D_x is the stability coefficient that reflects the specific DDD to reach a doubling in the measured response compared to the pre-irradiated sample. The difference in the normalized D/G' as a function of diameter is most accurately quantified by the calculated D_x values. Figure 17b demonstrates that D_x increases by a factor of ~ 2.5 as the diameter decreases from the laser-Ar to CoMoCAT sample, implying that the latter is more stable. The difference in the stability parameter indicates an intrinsic diameter dependent radiation response in SWCNTs, and can be best understood by analyzing the vacancy density, both per mass of carbon and per nanotube.

The samples used in the current study have equivalent areal mass density and were irradiated simultaneously, therefore, the vacancy density (*i.e.*, number of vacancies per unit mass), n_v , is expected to be the same. However, the different D_x values indicate that the number of vacancies per *nanotube* must be different for the CoMoCAT, laser-He, and laser-Ar SWCNT samples, which may result from differences in E_d or a diameter dependent defect generation mechanism. In the present work, the inter-vacancy length, L_v , is the mean distance between single point vacancies spaced along the length of the nanotube in the SWCNT axial direction. L_v is related to the vacancy density, n_v , and the mass per unit length, m_L , as shown in Eq. 3. Since defects were generated via ion irradiation, it is useful to express L_v in terms of DDD and E_d , where $n_v = DDD / (2.5E_d + 3)$.^{16, 17}

$$L_v = \frac{1}{m_L n_v} = \frac{2.5E_d + 3}{m_L DDD} \quad (3)$$

In Eq. 1, the Kinchin-Pease relationship is used to relate E_d to the average energy imparted by the recoil ions resulting in the formation of vacancies.¹⁷ This equation indicates that at a constant m_L , varying E_d within the typically expected range (*i.e.*, 15 – 22 eV) would only change L_v by approximately $\pm 10\%$ (compared to the originally assumed E_d of 20 eV). The m_L parameter in Eq. 1 is a dominant variable and can be expressed specifically in terms of the (n, m) chiral indices for any SWCNT as shown in Eq. 4:

$$m_L = \frac{4m_c}{3a_{cc}} \times \sqrt{n^2 + m^2 + nm} \quad (4)$$

where a_{cc} is the C-C bond length, m_c is the atomic mass of carbon, and n and m are the chiral indices. Thus, at a given n_v (or DDD), Eq. 5 contains the sought-after SWCNT chirality dependence, which illustrates the influence diameter has on L_v .

$$L_v = \frac{3a_{cc}}{4m_c} \times \frac{1}{n_v} \times \frac{1}{\sqrt{n^2 + m^2 + nm}} \quad (5)$$

The origin of the L_v dependence on diameter (chirality) is illustrated in Figure 18. The figure shows a 4.3×10.0 nm (W×L) graphene nanoribbon with 8 mono-vacancies (*i.e.*, 1 vacancy every ~ 203 C-atoms), which corresponds to a DDD of 1.3×10^{16} MeV/g (assuming $E_d = 20$ eV), and is near the mid-point of the experimental range in Figure 17a. Converting the graphene nanoribbon into the corresponding (10,10) SWCNT, or two equivalent (5,5) SWCNTs, illustrates that L_v is diameter dependent at a constant vacancy density. The 8 mono-vacancies remain for the (10, 10) SWCNT, and are divided into 4 mono-vacancies for each (5,5) SWCNT. The corresponding L_v is 1.25 nm for the (10,10), compared to 2.5 nm for the (5,5) SWCNT. Since n_v is equivalent in both cases, L_v is directly related to the diameter dependent variable, m_L . Therefore, in the case of an equivalent ensemble thin-film sample (*i.e.*, mass, bundling, lengths, etc.), there will be twice as many (5,5) SWCNTs compared to (10,10) SWCNTs, which results in half the number of vacancies per nanotube. The inter-vacancy length model is not limited to the assumption of mono-vacancies, but can be more generally referred to as an inter-“defect” model, which can include other defect-types (*i.e.*, di-vacancies,¹⁸ tri-vacancies, etc.). Overall, any inter-“defect” length will be inversely related to the defect density and the SWCNT diameter.

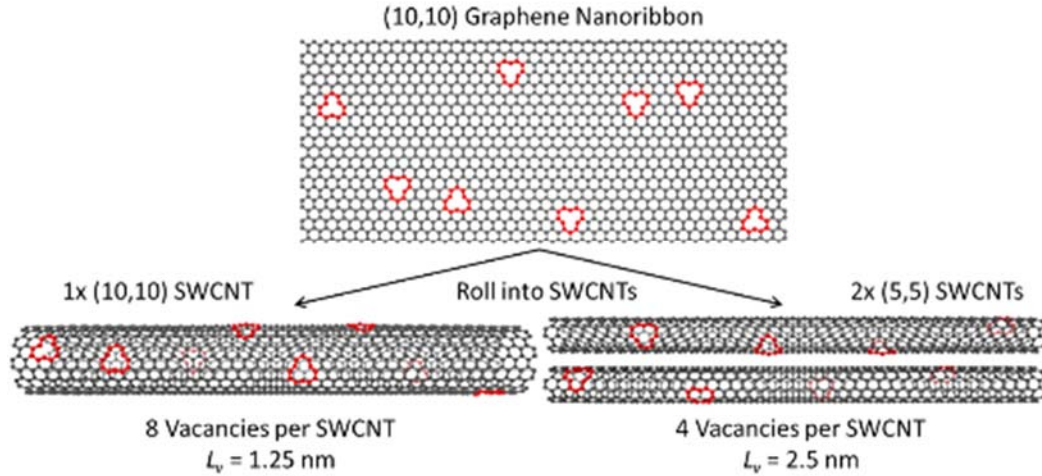


Figure 18. Graphene and SWCNT renderings illustrate the effect of SWCNT diameter (d_t) on the inter-vacancy length (L_v) at constant vacancy density (n_v). All defects are assumed to be mono-vacancies spaced along the length of the SWCNT in the axial directions. Figure taken from Ref. 14.

The critical inter-vacancy length where the normalized D/G' doubles (*i.e.*, L_x), can be determined using Eq. 3 with the value of D_x substituted for DDD . Assuming equivalent E_d for all samples, and using the empirical D_x values, a global fit for L_x was performed simultaneously using the least sum of squares method and including all 3 sample sets, which converge at an equivalent L_x . The fit values obtained for m_L correspond to an “effective m_L ” ($m_{L,eff}$) for each SWCNT thin-film sample, which represent the present diameter distribution. The universal L_x was found to be 7.4 nm, which is comparable to the originally reported value of 6.5 nm for SWCNTs synthesized via arc-discharge.¹⁶ The resulting $m_{L,eff}$ for the CoMoCAT, laser-He, and laser-Ar SWCNT samples are 1.69×10^{-21} g/nm, 2.27×10^{-21} g/nm, and 4.36×10^{-21} g/nm, respectively. The difference in $m_{L,eff}$ is expected based on the Raman RBM analysis (see Figure 16), which demonstrates that the diameter distribution is increasing from the CoMoCAT to laser-Ar sample. The empirical $m_{L,eff}$ values can be compared to the theoretical values for each SWCNT-type to validate the accuracy of the fit. Figure 19a summarizes calculated m_L values for all possible SWCNTs up to a (25,25) chirality (represented by the z-axis color gradient), and can also be analyzed as a function of the number of carbon atoms per unit length (N_L). The $m_{L,eff}$ values are plotted for the three SWCNT samples and are highlighted with a $\pm 10\%$ variation on the (n,m) contour plot to encompass the diameter distribution for each sample. The m_L values for known chiralities within each synthetic-type distribution are demarcated in Figure 19a with yellow stars. For example, the (6,5) SWCNT is a known chirality in CoMoCAT materials,¹⁹ which falls within the predicted $m_{L,eff}$ band for the CoMoCAT sample in the current study. In the case of the laser samples, the (8,7) chirality aligns with fluorescence mapping data for the laser-He sample,¹⁹ and although the $m_{L,eff}$ for the laser-Ar sample is slightly high, it falls within the expected d_t distribution based on the RBM analysis. Thus, the global fit for L_x produces $m_{L,eff}$ values consistent with known chiralities for each SWCNT synthetic-type and confirms the accuracy of the L_v model.

It can be useful to relate the Raman results for each sample to L_v and determine whether a characteristic length exhibits an equivalent response. The normalized D/G' was analyzed as a function of L_v for each SWCNT thin-film sample using the $m_{L,eff}$ values from the global fit as

representative, and an equivalent E_d of 20 eV. Figure 19b illustrates the relationship between the relative Raman response and $1/L_v$ for each SWCNT thin-film sample. The normalized D/G' data collapses to form a near singular curve as a function of $1/L_v$, thus indicating that the radiation response in SWCNTs is governed by an inter-vacancy length dependence. At any value of L_v , the measured Raman response is the same for all SWCNTs examined, although the DDD (and subsequently, n_v) required to achieve the specified length varies as a function of SWCNT d_t (see Figure S4b). Interestingly, the $1/L$ dependence is also observed in the normalized D/G and is consistent with physically shortened SWCNTs,^{20, 21} which demonstrates that the Raman response for highly defective SWCNTs behave similarly to physically shortened SWCNTs. However, the SEM analysis confirms that the original SWCNT morphology is maintained as L_v decreases with higher fluence. Thus, the inter-vacancy length model is effective in understanding the effects of ion irradiation and vacancy density in SWCNT materials. The implication of these findings is that an equivalent L_v corresponds to the same normalized D/G' for all SWCNT-types, independent of d_t or chirality.

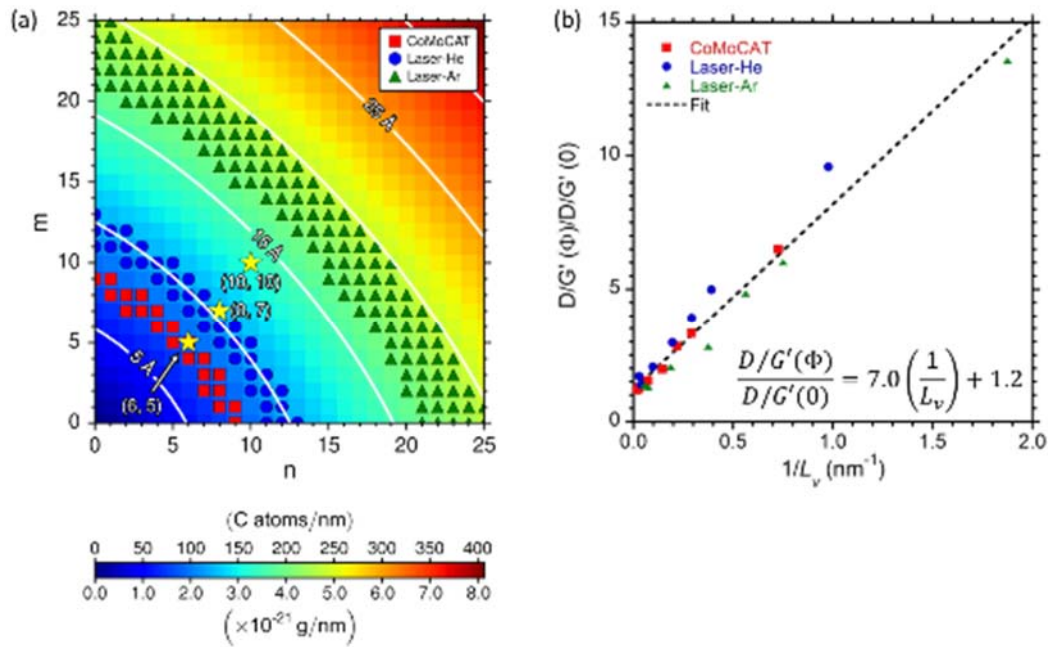


Figure 19. (a) The contour plot illustrates calculated m_L values (and N_L) for all SWCNTs up to a (25,25) chirality. The $m_{L,eff}$ values determined from a global fit for L_x are highlighted on the plot with a $\pm 10\%$ variation to account for the distribution of chiralities in the (■) CoMoCAT, (●) laser-He, and (▲) laser-Ar samples. The yellow stars (★) demarcate known chiralities for each synthetic-type. (b) The normalized D/G' is shown as a function of the inverse inter-vacancy length ($1/L_v$) for each of the SWCNT thin-films samples, which can be universally described by the functional form (inset equation) in the plot. Figure taken from Ref. 14.

The effect of ion irradiation on the optical properties of SWCNT thin-films as a function of diameter has been studied, and variations depend strongly on the inter-vacancy length, L_v . Suppression of the electronic transitions in the optical absorbance for the CoMoCAT, laser-He, and laser-Ar samples with increasing fluence (and DDD) influences the SWCNT Raman mode intensities, however, SEM analysis shows that the SWCNT morphology is maintained as the vacancy density increases under these conditions. Analysis of the normalized D/G'

indicates that the Raman response increases with increasing SWCNT diameter at all comparative levels of DDD . The D_x fitting parameter demonstrates the increase in stability of the CoMoCAT sample by nearly a factor of 2.5 compared to the larger diameter laser samples. A global fit was carried out to determine the universal critical length, L_x , which yielded $m_{L,eff}$ values for each SWCNT distribution that correlate well with known experimental values. Using the fit $m_{L,eff}$ values and a constant E_d , the normalized D/G' was analyzed as a function of $1/L_v$. At equivalent L_v , the mean vacancy spacing and relative Raman response is the same for all SWCNTs, independent of SWCNT d_t . Ultimately, the L_v model relates how the SWCNT network varies based on the number of mono-vacancies within each individual nanotube, and should remain valid independent of defect types.

2.3 Displacement damage dose effects studied via Hyperthermal Ion Implantation (HyTII)

Previous work on this project included the use of high-energy $^{11}\text{B}^+$ and $^{31}\text{P}^+$ irradiations of SWCNTs thin-films to uniformly introduce displacement damage through the full thickness of the SWCNT film. As discussed in section 3.1, these controlled irradiations provided a means to correlate the degradation in transport and changes in Raman spectra with the mean inter-vacancy length within each SWCNT in the film. The characteristic damage curves that resulted were found to also agree well with the changes observed in the transport properties of graphene. In the final year of this program, C^+ ions were used to introduce damage in bilayer graphene samples that were formed by stacking two monolayer graphene sheets.²² Since the graphene layers are polycrystalline, the crystallographic alignment of the top layer domains may be twisted with respect to the bottom layer forming domains with differing twist-angle, referred to as twisted bilayer graphene (TBG). The different twist angles lead to unique optical properties (Figure 20a) that, like SWCNTs, gradually diminish with defect concentration eventually becoming colorless (Figure 20b). The Raman modes of TBG also reveal a twist angle dependence: (i) small twist angle domains display characteristics consistent with inter-layer electronic coupling where the 2D peak intensity is similar to monolayer but displays a 4-Lorentzian lineshape, (ii) large twist angle domains display Raman modes that resemble two non-interacting graphene layers where the 2D peak intensity is $2\times$ that of monolayer, and (iii) there is a unique twist angle that yields electronic coupling with a high density of states near the energy of the laser excitation source resulting in a resonance condition and a greatly enhanced G-peak intensity that is more than $30\times$ monolayer graphene.

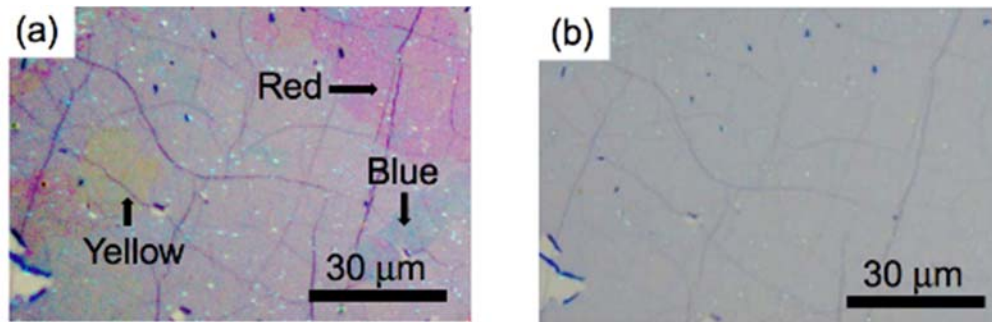


Figure 20. (a) Unfiltered optical image of TBG on 100 nm SiO_2/Si before ion bombardment showing the “yellow”, “red”, and “blue” domains observed under white light microscopy. (b) Equivalent optical image of the same area in (a) following ion bombardment with a fluence of $1\times 10^{15} \text{ cm}^{-2}$ (estimated defect density of $6\times 10^{13} \text{ cm}^{-2}$ per layer). Figure taken from Ref. 22.

Using the different coupling regimes observed in the Raman spectra, a defect coupling parameter was developed, which is the ratio of the 2D peak (or D peak) intensity for large twist angle TBG to the same peak in small twist angle TBG. The evolution of this coupling parameter, as well as the G-peak enhancement factor, were characterized with respect to the inter-vacancy length as shown in Figure 21. By fitting the changes in coupling parameter and G Peak Enhancement, the characteristic defect radii (r_x) are calculated, which characterizes the circular area that a defect diminishes the interlayer coupling. Regarding the G-peak enhancement, the r_G is quite large, 2.4 nm meaning a single defect in either graphene layer disrupts the electronic resonances in a circular area that would encompass over 200 atoms. In contrast, the $r_{2D} = 0.8$ nm indicating a defect decouples the layers only few close to the defect, encompassing a region containing <30 atoms. These results stem from the fact that the interlayer resonance condition stems from a delocalized electronic state, while effects on Raman modes are dominated by the local atomic structure.

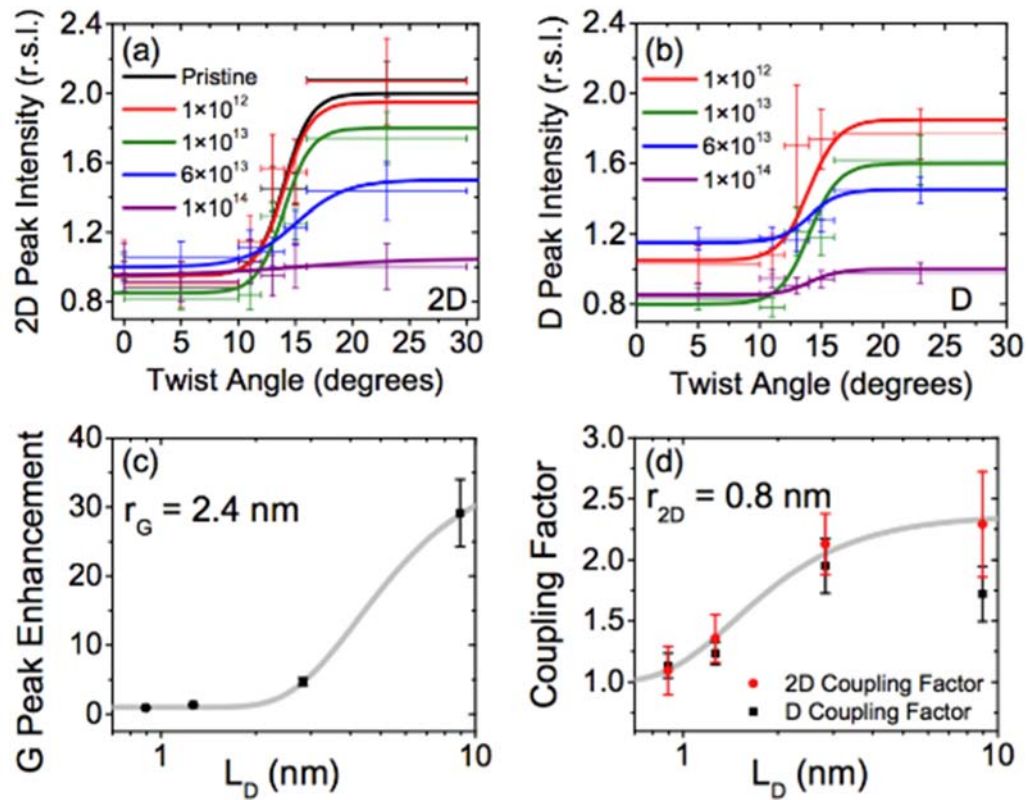


Figure 21. Variation in the Raman spectra of fTBG as a function of defect density. (a) Variations in 2D peak intensity as a function of twist angle and defect density. For each defect density, average 2D intensity is shown for five distinct twist angle ranges. Solid lines are included as a guide to the eye. Defect densities indicated are total defect densities, including both graphene layers. (b) Variation in D peak intensity are similarly represented. Again, solid lines are included as a guide to the eye. D peak intensity data is not included for pristine graphene. (c) Variations in G peak enhancement as a function of distance between defects (including both graphene layers). Data are fitted based on Eq. (1) ($P_{\text{coupled}} \cdot G_{\text{max}} + (1 - P_{\text{coupled}}) \cdot G_{\text{min}}$) using a radius of 2.2 nm (gray curve). (d) Variation in D and 2D peak coupling factor as a function of distance between defects (including both graphene layers). 2D peak intensity is fitted based on Eq. (1) with a radius of 0.82 nm (gray curve). No fit is presented for the D peak, but for defect densities above $1 \cdot 10^{13} \text{ cm}^{-2}$, the D peak coupling factor follows that of the 2D peak. Figure taken from Ref. 22.

3. Radiation-Induced Defect Characterization

3.1 Spatial Defect Profiling by Selective Au-NP Nucleation

Raman spectroscopy and electrical transport measurements are traditionally used to characterize the response of SWCNTs to ion irradiation. While these techniques provide valuable insight into the extent of defect generation, spatial profiling of the density and distribution of defects in SWCNTs from ion irradiation may provide further understanding of changes in the material properties and the defect generation process. High-resolution profiling of irradiation-damaged SWCNT networks requires detection of a large numbers of defects but at nanometer-scale resolution. Current profiling techniques such as Raman mapping and microscopy are either resolution-limited, or are not practical for profiling large sample areas such as SWCNT networks. Far-field Raman mapping for instance, is capable of relatively large area analysis, but is diffraction limited ($\lambda/2$), making it ineffective for nanometer-scale resolution. Near-field Raman mapping, on the other hand, can achieve as low as 10 nm resolution, but is typically only useful for acquiring defect locations in single SWCNTs and is not practical for large area analysis. Methods such as transmission electron microscopy (TEM) or scanning transmission microscopy (STM) are also capable of identifying single defects in SWCNTs, but again, are impractical for acquiring defect distributions in SWCNT networks because of both experimental time scale and sample preparation.

Selective Au nanoparticle (Au-NP) deposition onto SWCNTs damaged by ion irradiation was investigated as a candidate for high-resolution defect profiling in SWCNT networks. SEM and image analysis techniques were used for rapid assessment of large numbers of Au-NPs nucleated onto defective SWCNTs. High purity laser-Ar SWCNT papers were irradiated with 150 keV $^{11}\text{B}^+$ over a range of fluences to intentionally introduce varying levels of defects into the system, followed by exposure to 0.01 M $\text{KAuBr}_{4(\text{aq})}$ for specific times. Raman spectroscopy was used to characterize the irradiation damage and scanning electron microscopy was used in conjunction with image analysis techniques to analyze Au-NP nucleation.

Particle nucleation studies were conducted to understand the selectivity of using a 0.01M $\text{KAuBr}_{4(\text{aq})}$ solution to nucleate Au-NPs on defective SWCNTs. Initially, a purified SWCNT paper was partially masked by quartz and irradiated with 1×10^{15} ($^{11}\text{B}^+$)/ cm^2 . The mean penetration depth of 150 keV $^{11}\text{B}^+$ in quartz is ~ 500 nm, as approximated by SRIM²³ calculations, confirming that the 650 ± 3 μm quartz mask was sufficient to terminate all ions. In the irradiation-exposed regions, the prominent Raman modes are significantly affected by the irradiation.¹⁶ This high dose helps to ensure that there are enough defects sites to make the Au-NP-tagged region obvious in subsequent SEM analysis. Figure 22 shows SEM images at (a) 10,000 \times and (b) 30,000 \times magnification of the irradiated/masked SWCNT paper after immersion in 0.01M $\text{KAuBr}_{4(\text{aq})}$ for 1 minute. The images clearly illustrate the boundary between the irradiated (left) and quartz-masked (right) sides from particle nucleation, and is related to the presence of SWCNT defects rather than any boron present on the surface given the ion penetration depth in the sample. The selectivity of Au nucleation onto ion-irradiated SWCNTs (and not onto purified SWCNTs) shows that the technique can be used to investigate spatial distributions of ion irradiation-induced defects as well as

potentially being used to controllably deposit Au-NPs onto SWCNTs for other applications. These results support the ongoing interest to identify the location and spatial distribution of defects in SWCNT materials, and presently are shown for an ensemble network of irradiated SWCNTs.

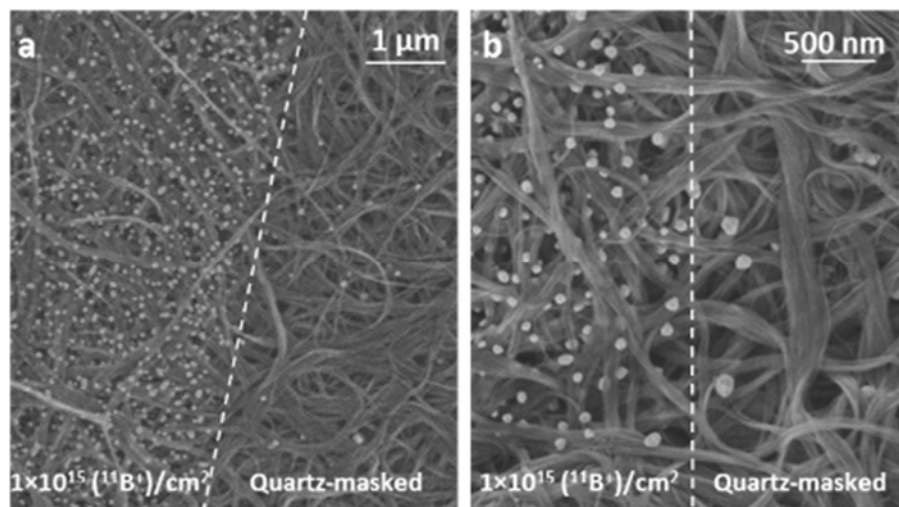


Figure 22. SEM images at (a) 10,000 \times magnification and (b) 30,000 \times magnification of a purified SWCNT paper which was partially masked by quartz (650 μm thickness) during ion irradiation at $1 \times 10^{15} \text{ }^{11}\text{B}^+/\text{cm}^2$ and subsequently exposed to 0.01M $\text{KAuBr}_{4(\text{aq})}$ for 1 minute. The dashed line demarcates the boundary of the quartz mask which highlights the Au-NP nucleation on the irradiated SWCNTs compared to the quartz-masked region. Figure taken from Ref. 40.

The Au-NP nucleation process was investigated as a function of $\text{KAuBr}_{4(\text{aq})}$ -exposure time at a constant fluence to determine a suitable method for spatial profiling of defective SWCNTs. The intent is to identify exposure conditions, which rapidly saturate all available nucleation sites with Au-NPs, while minimizing particle size from Ostwald ripening.²⁴ The collective results from SEM and statistical image analysis confirmed that 30 seconds is sufficient time to yield a saturated density of Au-NPs, thus establishing appropriate exposure conditions for further spatial defect profiling.

SWCNT papers were exposed to different 150 keV $^{11}\text{B}^+$ fluences to modify the number of defects and determine if a corresponding change in the number of nucleation sites is observed. Representative portions of a purified SWCNT paper were irradiated at fluences of 1×10^{13} , 1×10^{14} , 5×10^{14} , and $1 \times 10^{15} \text{ }^{11}\text{B}^+/\text{cm}^2$ and exposed to 0.01M $\text{KAuBr}_{4(\text{aq})}$ for 30 seconds. SEM and statistical image analysis showed both qualitatively and quantitatively that the density of Au-NPs (*i.e.*, $\text{Au-NPs}/\mu\text{m}^2$) increase with increasing fluence, and thus affirms that the Au-NP tagging technique is sensitive enough to distinguish between different radiation doses.

The observed increase in Au-NP density is expected to correlate with higher intrinsic structural damage to the SWCNTs, however, comparison with Raman can provide a direct probe of ion-generated defects for SWCNTs and validate this model. The degradation of the Raman spectra for the purified laser-synthesized SWCNT papers is consistent with reported values for irradiated electronic-type-separated arc SWCNT thin-films.¹⁶ Figure 23 shows the

relative change in the D/G' ratio (*i.e.*, normalized to the initial D/G' ratio of the starting material) for each irradiated SWCNT paper prior to Au-NP nucleation. The measured Au-NP density after exposure to $\text{KAuBr}_{4(\text{aq})}$ (as quantified by the image processing of data) is overlaid with the relative changes in the D/G' peak ratios. A relative increase in the D/G' ratio (\square) with increasing fluence is observed and tracks directly with the particle density (\diamond). These results clearly show a strong correlation between the structural degradation of the SWCNTs (as measured via D/G') and the Au-NP density (measured via image analysis). Since the D/G' ratio corresponds to an increase in the number of defects and there is a concomitant increase in particle density, the direct correlation implies that the Au-NP deposition is tagging a consistent fraction of additional defects at increasing fluence. This result is exemplified by the particle density plotted as a function of relative change in D/G' ratio values (see Figure 23 inset). The dashed line represents a linear fit ($R^2 = 0.998$) to the data, and the equation of the line can be used as a calibration for the Au-NP density that could be achieved if desired. Overall, the approach directly shows a method to assess different levels of radiation exposure (*i.e.*, dosimetry) as well as the ability to tune the number of Au-NPs on the surface by varying radiation conditions.

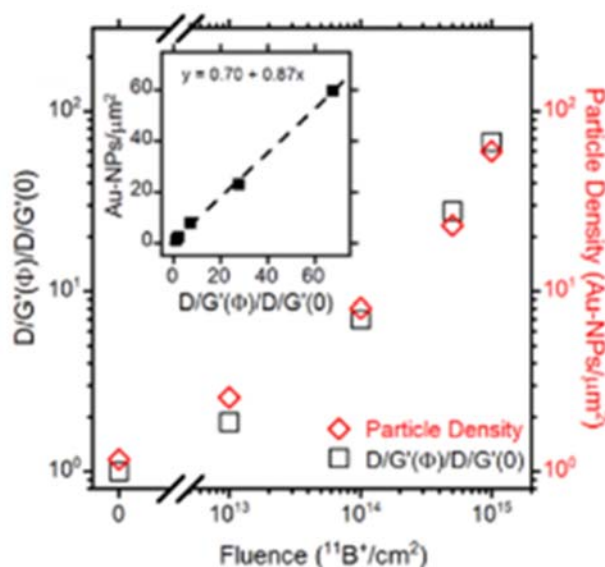


Figure 23. The relative change in D/G' peak ratio values (\square) and the Au-NP density (\diamond) are plotted versus fluence. The inset shows the particle density plotted versus the relative change in D/G' ratios, with the dashed line representing a linear fit ($R^2 = 0.998$) to the data and the equation of the line shown. Figure taken from Ref. 40.

An electroless Au-NP nucleation process (with $\text{KAuBr}_{4(\text{aq})}$) has been rigorously characterized to identify the spatial distribution of defects in SWCNT materials after ion irradiation with 150 keV $^{11}\text{B}^+$. The selectivity of Au-NP nucleation onto ion-irradiated SWCNTs (and not onto purified SWCNTs) shows that the technique can also be used as a method to controllably deposit metal nanoparticles onto SWCNTs for other applications. The nucleation of Au-NPs has been statistically analyzed as a function of exposure time and fluence. The observed increase in Au-NP density correlates directly with an increase in the Raman peak ratios of the D and G' bands, thus providing another probe of ion-generated vacancies in SWCNTs. Overall, the process for Au-NP deposition is amenable to standard laboratory or

cleanroom practices, making the process adaptable to further studies investigating radiation stability of various SWCNT/metal structures such as thin films.

3.2 Defect Identification in Irradiated SWCNT Thin-Films Using Thermal Imaging

Thermal imaging has been proposed as an alternate method for identifying radiation-induced defects in SWCNT thin-films. Thin-film test structures were fabricated using laser-Ar SWCNTs dispersed in 2.0 wt% SDS. SWCNTs were isolated from solution onto an MCE membrane and transferred to polished quartz. The resulting SWCNT thin-film was cut into a 3.5×1 cm (W×L) rectangle, and four metal contacts were deposited by thermal evaporation (200 nm Ag) to aid in electrical characterization. Figure 24a shows a schematic of the as-produced test structure. Two additional, equivalent test structures were fabricated, the first of which was irradiated over the entire structure (see Figure 24b), and the other which was masked during ion irradiation to create striped regions of pristine SWCNTs surrounded by areas of highly damaged SWCNTs (Figure 24c). The striped test structure was masked with 20 μ m Al foil having two rectangular openings to allow for radiation exposure. The irradiated samples were implanted with a fluence of 5×10^{14} ions/cm² using 150 keV ¹¹B⁺. Raman and optical absorbance spectroscopy show a clear distinction between the as-produced and irradiated portions of the striped SWCNT sample.

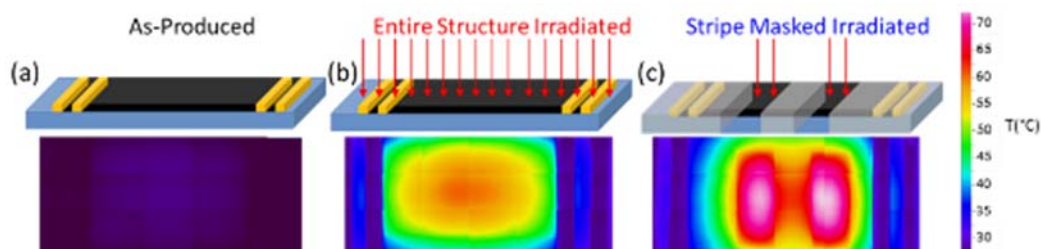


Figure 24. A schematic and thermal image are given for (a) an as-produced SWCNT thin-film test structure, (b) an irradiated (entire structure) SWCNT test structure, and (c) a stripe masked SWCNT thin-film test structure. Irradiated samples were implanted with a fluence of 5×10^{14} ions/cm² using 150 keV ¹¹B⁺. The thermal images were captured while driving 4 – 6 μ A through each sample.

Analysis using thermal imaging of the three samples was carried out while driving 4 – 6 μ A of current through each respective sample. Figure 24 shows the results of the thermal imaging, where the irradiated regions of the SWCNT thin-film heats up compared to the as-produced control. Figure 24a and b demonstrate that both the as-produced and irradiated (entire structure) samples dissipate heat uniformly, while Figure 24c demonstrates that the stripe masked sample shows clear demarcation between the pristine and irradiated portions of the sample. However, the irradiation significantly increases the SWCNT resistance requiring higher bias conditions to achieve the target current (see Figure 25a). As a result, the irradiated samples exhibit significantly higher temperatures at a fixed current (see Figure 25b). Thus, thermal imaging provides a remote method for identifying damage in SWCNT test structures.

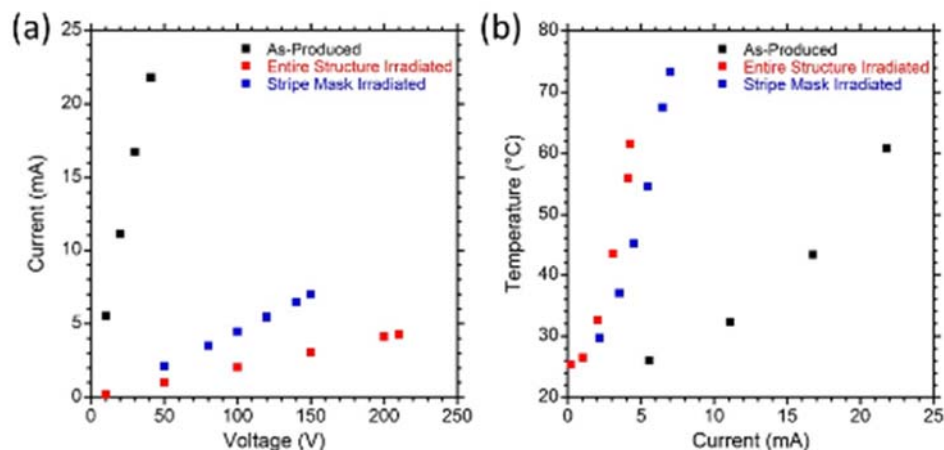


Figure 25. (a) The I-V profile for the three SWCNT thin-film test structures corresponding to each thermal profile is shown. (b) Temperature is given as a function of current for the as-produced and irradiation SWCNT samples.

4. Electrical Characterization of Irradiated SWCNTs

4.1 Mechanism of Chemical Doping in Electronic-Type-Separated SWCNTs

Doping susceptibility of SWCNT thin-films was studied as a function of electronic-type using I_2 , IBr, CSA and $KAuBr_4$ dopants with the goal of enhancing their electrical conductivity. Changes in SWCNT optical absorption, Raman spectra, and electrical conductivity were investigated. NanoIntegris SWCNT materials were used to fabricate semiconducting (referred to as “semi”, Iso-Nanotubes-S, 99%), mixed (referred to as “mixed”, Ultra-Pure SWNTs, 99%), and metallic (referred to as “metallic”, Iso-Nanotubes-M, 98%) SWCNT thin-films. One sample from each SWCNT electronic-type was doped for 1 hour with the following: (1) 10 mM $KAuBr_4$ in DI water, (2) I_2 vapor in a sealed container at 100 °C with air ambient, and (3) 0.36 M IBr in ethanol. All doping chemicals were purchased from Sigma Aldrich. The $KAuBr_4$ samples were rinsed with 10mL of DI water and the IBr samples with 10 mL of ethanol to remove any excess solution from the surface of the film and allowed to dry in air at 18-20 °C for 30 minutes. After doping, all SWCNT thin-films were characterized with optical absorbance spectroscopy, Raman spectroscopy, optical profilometry, and 4-point probe sheet resistance measurements.

The electrical conductivity of purified and doped electronic-type-separated SWCNT thin-films is calculated based on the sheet resistance and thickness of each sample (measurements by optical profilometry), and is presented in Figure 26. The thickness measurements include a $\pm 15\%$ variation in conductivity due to the error in the thickness measurement, which should also be added to each of the reported values in Figure 26, but has been omitted for clarity. The purified semi SWCNT thin-film has an average conductivity of 7.3×10^4 S/m based on the average of four samples, while the purified, mixed SWCNT thin-film has an average conductivity of 4.6×10^4 S/m. The purified, metallic SWCNT thin-film has a slightly higher average conductivity compared to the other purified electronic-type-separated SWCNT thin-films at 9.0×10^4 S/m. The higher average conductivity for semi and metallic films compared to the mixed sample may be attributed to the difference in network transport from contact resistances in mixed SWCNT electronic-types.²⁵ The doped semi SWCNT thin-films show the largest increase in conductivity by an average of 3x with I_2 , IBr, and CSA,

while KAuBr_4 resulted in a 6x increase to the highest overall conductivity of $4.3 \times 10^5 \text{ S/m}$. Metallic SWCNT thin-films show a marked change in conductivity when doped (up to 3.5x) with respect to the purified film when using CSA and KAuBr_4 dopants. The use of I_2 and IBr has minimal influence on the metallic SWCNT thin-film conductivity, which is consistent with the lack of doping changes based upon the Raman results. Mixed SWCNT thin-films exhibit a relative increase in conductivity, on average between the phase-pure semi and metallic SWCNT thin-films ranging from 3x to 5x, with KAuBr_4 offering the largest increase. Although material variations in length, defect density, and bundling are likely additional factors affecting relative changes in conductivity from inter-SWCNT barriers,²⁵⁻²⁷ the present results illustrate the importance of specific chemical interactions with electronic-type-separated SWCNTs and the resulting electrical conductivity. The purified metallic SWCNT thin-film exhibits the higher intrinsic conductivity, however, the semi SWCNT thin-films show the highest susceptibility for the present dopants resulting in the largest relative change in conductivity. Although a slightly higher relative change is observed using CSA with metallic SWCNT thin-films (potentially related to the proton affinity with metallic chiralities), KAuBr_4 achieves a significant change in the electrical conductivity for all SWCNT thin-film samples and continues to represent a unique electrochemical interaction for enhancement.

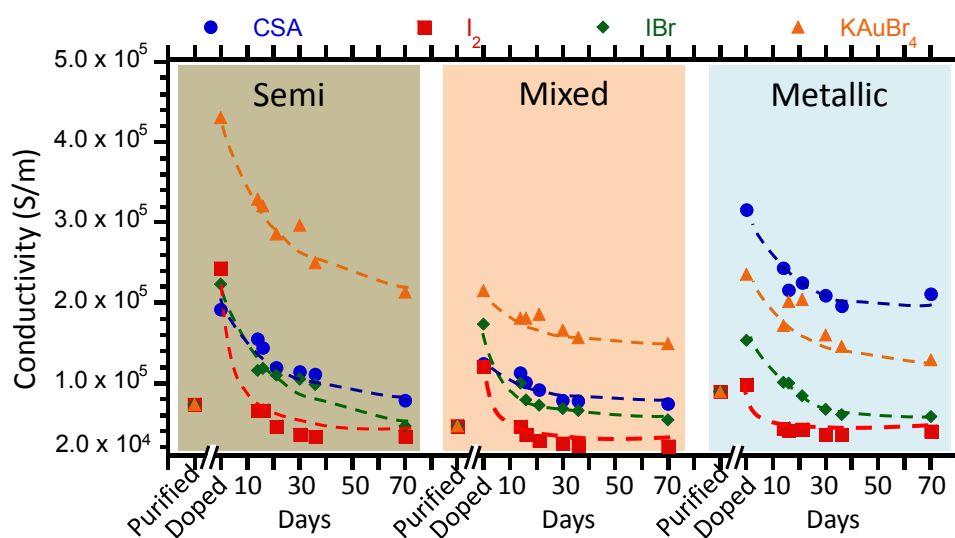


Figure 26. Electrical conductivity of semi, mixed, and metallic purified SWCNT thin-films and the corresponding effects after doping with CSA, I_2 , IBr , and KAuBr_4 . The time-dependent conductivity was studied over 70 days to assess dopant stability. The data points should include error bars representing $\pm 15\%$ error based on the thickness measurements, but have been omitted for clarity. Figure taken from Ref. 41.

The time-dependent conductivity of the SWCNT thin-films was measured by storing the doped SWCNT samples under ambient room conditions (Temperature = $18\text{--}20^\circ\text{C}$, Relative Humidity = $20\text{--}40\%$) for 70 days while performing systematic 4-point probe measurements to better understand dopant stability. As shown in Figure 26, the electrical conductivity of all doped SWCNT thin-films decreases over time, while the purified undoped SWCNT thin-films remained unchanged. The dashed lines are a guide to the eye to follow the decay that levels off after approximately 30 days. There is no appreciable difference in stability as a factor of the SWCNT electronic-type. On the other hand, there are appreciable differences due to the type of dopants. SWCNT thin-films doped with I_2 and IBr are the least stable in all

three electronic-type-separated SWCNT thin-films. The electrical conductivity of the SWCNT thin-films doped with I_2 and $I\text{Br}$ decrease back to the original undoped conductivity in about 30-40 days. The electrical conductivity retention for CSA is highest for the metallic SWCNT thin-films and progressively lower for the mixed and semi SWCNT thin-films, respectively. However, in the case of KAuBr_4 , there is residual conductivity enhancement after 70 days for all three SWCNT electronic-types and is most dramatic for the semi SWCNT thin-films.

The effectiveness of certain chemical dopant interactions with electronic-type-separated SWCNTs is shown to be critical to enhance the electrical conductivity. Correlating the relative change in the electrical conductivity of SWCNT thin-films to the Raman G' peak shift after doping can provide an empirical relationship for determining the extent of charge transfer. Figure 27(a) summarizes the data for each of the measured SWCNT thin-films and shows that the largest shift in the Raman G' peak results correlates with the largest improvement in electrical conductivity. For the semi and mixed SWCNT thin-films (triangle and circle symbols in Figure 27(a), respectively), the relationship between the G' -peak shift and the relative conductivity increase is loosely distributed between $8 - 10 \text{ cm}^{-1}$ and $2.5\times$ to $6.0\times$, respectively. This threshold doping behavior suggests an underlying relationship with the quantized electronic states for SWCNTs based on their bandgaps and requires a sufficient electrochemical difference to activate a response. For the metallic SWCNT thin-films, a clear linear relationship is observed between the G' -peak shift and the relative conductivity increase (square symbols in Figure 27(a)), indicating a gradual increase in doping intensity based on the doping species.

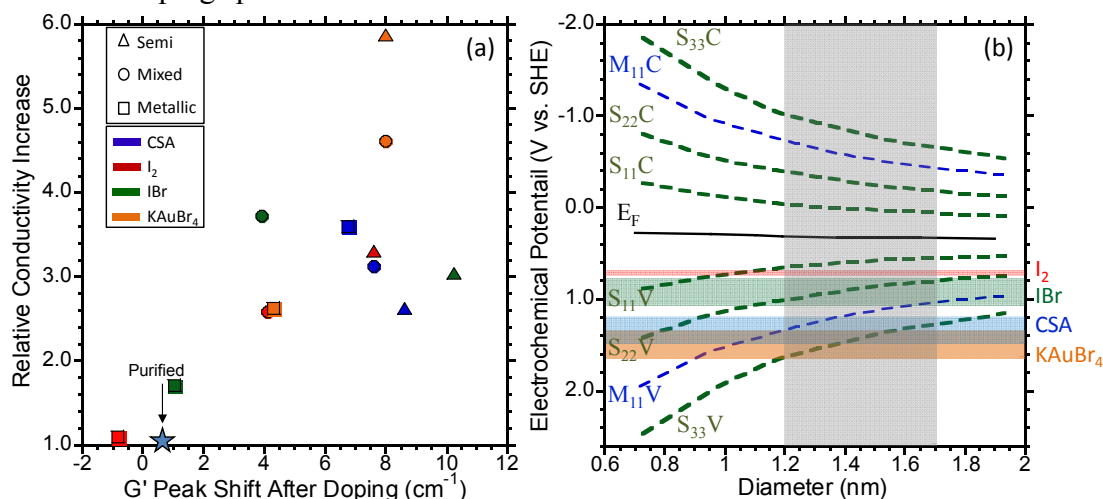


Figure 27. Relative change in electrical conductivity as a function of the G' -peak position shift based upon the ratio of the electrical conductivity of the doped to purified SWCNT thin-film. (b) Fermi level position and electrochemical potential of the valence (V) and conduction (C) energy transitions, with respect to a standard hydrogen electrode, as a function of SWCNT diameter.²⁷ The range of redox potentials of the doping species and the range of SWCNT diameters in this experiment ($1.2 - 1.7 \text{ nm}$) is represented by the shaded regions.²⁸ Figure taken from Ref. 41.

Figure 27(b) shows the valence and conduction energy levels of SWCNTs as a function of their diameter with respect to a standard hydrogen electrode (SHE) to relate the electrochemical potential for the SWCNTs and the doping species involved in these experiments.^{27, 29, 30} Thus, it can be seen that the redox potentials of all four dopants have a

more positive potential than the energy of the first semiconducting electronic transition, indicating that all four dopants can oxidize the semiconducting SWCNTs. There is some uncertainty in terms of the exact redox potential for some of the doping species given the complex reaction in solution and this is represented by the bands in Figure 27(b). Since the semi SWCNT thin-films contain the highest concentration of semiconducting SWCNTs compared to the mixed thin-films, it explains the greater G'-peak shifts for these samples and corresponding higher electrical conductivities. In some cases, the redox potential of certain doping species could exceed the second and third semiconducting transition energy levels. As indicated by Figure 27(b), this may explain the dramatically higher doping response with KAuBr₄ due to the more positive electrochemical potential, suggesting that the S₃₃ is also being depleted of electron density. In comparison, the electrical conductivity improvement of metallic SWCNT thin-films, based on the shift of the G' peak position, is gradual and continuous (square symbols in Figure 27(a)). This correlates to the fact that the first metallic SWCNT electronic transition band is at a much higher energy than the observed Fermi level and the interaction with chemical dopants can take place gradually with the available density of states present in the low energy levels.³¹ I₂ and IBr dopants weakly dope the metallic SWCNTs due to the fact that the redox potential of the doping species tend to be less positive than the first metallic SWCNT electronic transition with a diameter range of 1.2 - 1.7 nm.²⁷ Conversely, CSA and KAuBr₄ result in strongly doped metallic SWCNT films as the redox potential of the dopant species (*i.e.*, ClO₄⁻, Au₃⁺, Au⁺) are near or more positive than the first metallic SWCNT electronic transition.²⁸

The combination of the spectroscopy results (*e.g.*, optical absorption suppression and Raman G' peak intensity and shifts) with the electrical conductivity measurements supports the mechanism of electrochemical doping for SWCNTs. Based upon the equilibrium redox potentials, the strength of an acceptor-dopant to oxidize the SWCNTs will be based on the alignment of the electrochemical potential with a specific SWCNT electronic-type. In the case of the present four dopants, CSA and KAuBr₄ are most effective across all samples due to the more positive electrochemical potential, whereas I₂ and IBr are only effective with semi SWCNT thin-films due to their corresponding lower potential. Thus, the number of chemical species available to dope semi SWCNT thin-films will be greater compared to metallic SWCNT thin-films due to the larger potential needed to exceed the M₁₁ transition energy. Overall, the results herein demonstrate that using highly enriched electronic-type-separated SWCNTs support the past theoretical predictions and results with mixed SWCNTs²⁷ and substantiate the mechanism of electrochemical doping in SWCNTs towards providing a predictive framework for advancing the electrical conductivity in bulk structures.

4.2 Effect of Ion Irradiation on Chemically Doped Electronic-Type-Separated SWCNTs

In applications where enhanced electrical conductivity of SWCNT structures is desired, chemical doping of electronic-type-separated SWCNTs is commonly employed. Typical dopants are N₂H₄, I₂, NHO₃, SOCl₂, and KAuBr₄.³²⁻³⁷ In the current study the radiation hardness of doped electronic-type-separated SWCNTs is investigated. The structural and electrical properties of KAuBr₄-doped semiconducting (S-SWCNT) and metallic (M-SWCNT) SWCNT thin-films are investigated as they are irradiated with 150 keV ¹¹B⁺ ions with fluences ranging from 5×10¹² to 1×10¹⁵ ions/cm². These results are compared to purified electronic-type-separated SWCNT thin-films fabricated simultaneously and irradiated

together to minimize variations in sample preparation and radiation exposure conditions. The results of this work provide insight on the effect of radiation on the electrical conductivity and defect density of doped SWCNT thin-films.

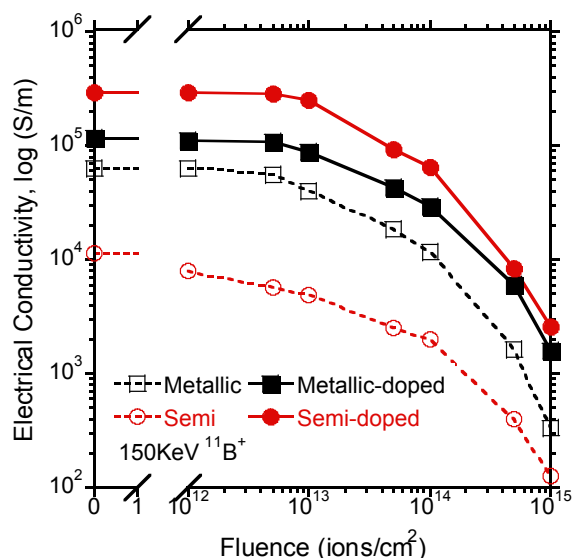


Figure 28. Conductivity of purified and doped irradiated electronic-type-separated SWCNT thin-films.

The sheet resistance was measured after each irradiation while the thickness of the thin-films was assumed as constant and only measured for the as-produced sample. Variations in R_s correlate to observations made in optical and Raman spectroscopy (previously shown) and provide insight in the irradiation-induced degradation of the SWCNT thin-films. Figure 29a shows the R_s of the purified and doped M-SWCNT and S-SWCNT thin-films in a log scale with increasing irradiation dose. All SWCNT thin-films behave in a similar fashion showing a slight increase in R_s up to a dose of 5×10^{12} ions/cm². As the irradiation dose is increased beyond this value, a logarithmic increase is observed for all samples. On the other hand, and most significant, is the fact that the conductivity enhancement that is provided by the chemical doping is maintained throughout the irradiation exposure up to the highest irradiation dose.

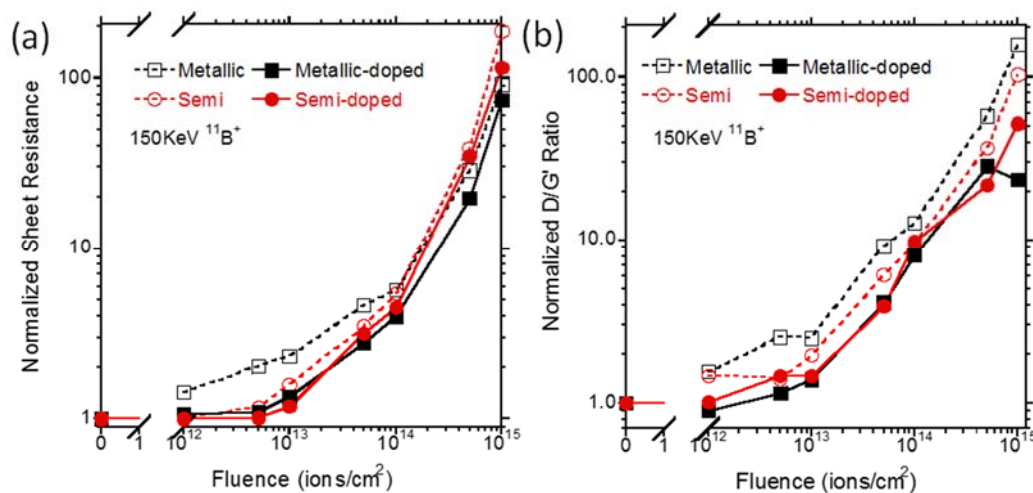


Figure 29. (a) Normalized sheet resistance and (b) normalized Raman D/G' ratio as a function of irradiation dose for purified and doped S-SWCNT and M-SWCNT thin-films.

The rate of increase in the electrical conductivity is similar for all the studied SWCNT thin-films, independent of their electronic-type and doped or purified condition, and is clearly observable in the normalized R_s plot shown in Figure 29a. This observed increase in R_s correlates to the observations made through Raman spectroscopy. More specifically, analysis of the progression of the ratio between the D and G' band peaks, as an indication of the amount of defects to the amount of available carriers,²⁰ we observe that it follows a similar trend in its decay for all the SWCNT thin-films as shown in Figure 29b.

Based on the data presented, the defects generated through irradiation are responsible for the degradation of electrical conductivity of the electronic-type-separated SWCNT thin-films studied. Moreover, the increase in the number of defects affects the electrical conductivity of purified and doped SWCNT thin-films equally. On the other hand, the electrical conductivity enhancement that chemical doping provides is maintained as the number of defects increases in the thin-film networks. As such, in applications where high electrical conductivity and radiation hardness is desired, doped SWCNTs provide a viable technology.

4.3 Diameter Dependent Conductivity in Ion Irradiated SWCNT Thin-Films

The effect of displacement damage dose (DDD) exposure on the optoelectronic properties of SWCNT thin-films was demonstrated as a function of diameter distribution. It was determined that prominent SWCNT peaks in both the optical absorption and Raman spectra decrease monotonically with increasing fluence.¹⁴ This work has been extended to study the effect of ion irradiation on the electrical transport properties of SWCNT thin-films as a function of diameter distribution. Thin-films were fabricated using CoMoCAT (0.7 – 0.9 nm), HiPco (0.8 – 1.2 nm), Laser-He (0.9 – 1.3 nm), Laser-Ar (1.0 – 1.7 nm), and Arc (1.2 – 1.7 nm) SWCNTs to span the typical range of diameters used in common nanoelectronic applications. Metal contacts (100 nm Pd) were evaporated onto each of the four corners of the samples to aid in electrical characterization using 4-point probe measurements and the van der Pauw method. The sheet resistance (R_s) of each as-produced SWCNT thin-film was measured to obtain a baseline prior to radiation exposure. The SWCNT thin-films were subsequently exposed to incrementally increasing doses of 150 keV $^{11}\text{B}^+$ with fluences between 5×10^{12} to 1×10^{15} ions/cm², and R_s was measured after each radiation exposure.

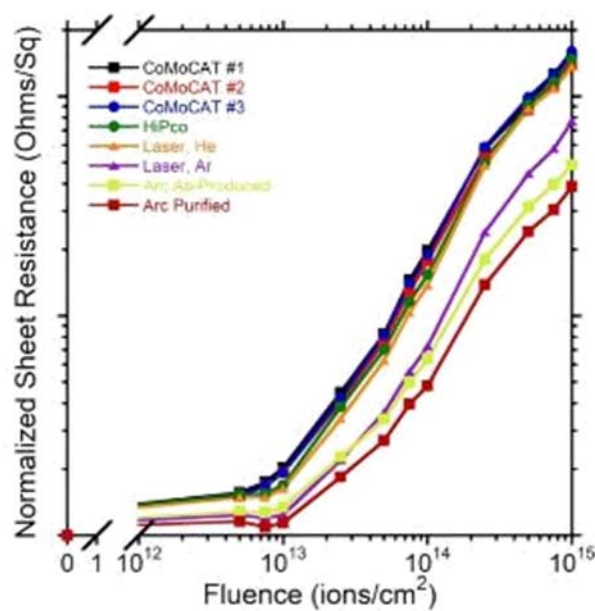


Figure 30. The sheet resistance (R_s) was monitored as a function of incrementally increasing fluence after ion irradiation with 150 keV 11B⁺ in SWCNT thin-films fabricated from CoMoCAT, HiPco, Laser, and Arc synthetic materials. All irradiated R_s values are normalized to the as-produced baseline value.

The baseline R_s increases with decreasing diameter distribution, which may be related to the length, degree of bundling, purity, etc. in the starting materials. Therefore, R_s data was normalized to the baseline value so that relative changes in electrical transport could be evaluated with increasing radiation exposure. As shown in Figure 30, R_s increases monotonically with increasing fluence for all samples, independent of the diameter distribution. The rate of change in R_s increases as the SWCNT diameter distribution decreases. This requires additional analysis to distinguish between a diameter affect compared to differences in the physical morphology of the SWCNT thin-film, such as length distributions and bundle diameter. Currently, the effect of bundle size is being examined using Laser-Ar SWCNTs. The SWCNTs are dispersed in chlorosulfonic acid (CSA) and bundle size is tuned by adding varying amounts of water to the dispersion to cause the SWCNTs to precipitate prior to thin-film fabrication. Bundle size will be quantified using SEM, and the physical and electrical properties will be studied as a function of radiation exposure.

4.4 Radiation Effects on SWCNT-Metal Contact Interfaces

The effects of ion irradiation on the contact resistance between different metals and SWCNTs are an important consideration in applications where devices will be exposed to harsh radiation environments. Recent studies suggest that a small concentration of point defects resulting from low dose irradiation may enhance the contact resistance between metal and graphene,^{38, 39} however, radiation effects on SWCNT-metal contact interfaces have not been fully studied to date. Thus, preliminary experiments have been conducted to assess the contact resistance between thermally evaporated Ag and ion-irradiated SWCNT thin-films.

Structures were fabricated for performing transfer length method (TLM) measurements to determine the contact resistance between Ag and SWCNTs. A high purity SWCNT thin film (SWCNTs produced in-house by laser vaporization synthesis) was fabricated by vacuum

filtration, halved, and transferred onto two Si/SiO₂ substrates by a standard MCE transfer process. Ag contacts with thicknesses of 1.5 μm (thick contacts) and 0.1 μm (thin contacts) were deposited via thermal evaporation through a shadow mask. Figure 31a is a schematic of the surface of the TLM structure, with Ag electrode dimensions of 2 mm and 8 mm (L and W, respectively), and SWCNT channel lengths ($d_1 - d_4$) of 1, 2, 3, and 4 mm. The samples were each irradiated with 150 keV $^{11}\text{B}^+$ at 5×10^{14} ions/cm² using the shadow mask as a radiation shield. Figure 31b and Figure 31c illustrate this process for the thick and thin contacts structures, respectively. The shadow mask is of sufficient thickness (0.5 mm) to mask the SWCNTs in the channel (between the Ag contacts) from the incident ions, so that only the Ag contacts are irradiated. Contact resistance measurements were taken before and after ion irradiation, to monitor the changes, if any, of the contact resistance in response to ion irradiation. For the contact resistance measurements, 4pt electrical measurements were taken by forcing current between each pair of electrodes and monitoring the voltage, and the resistance calculated from the resulting values ($R = V/I$). Raman spectroscopy measurements of the SWCNTs were performed both in the channel (shielded from irradiation) and under the contacts. Kapton tape was used to peel the Ag contacts off of the SWCNTs to enable Raman measurements of the SWCNTs under the contacts.

The Ag contact thicknesses for the structures in these experiments were specifically chosen for two intended scenarios: (1) that the ions would come to rest within the thick contact structures and (2) that the ions would be transmitted through the thin contact structures to the underlying SWCNTs. In this way, a comparison of the contact resistance values between the structures will reveal the extent to which the ions have an impact on the Ag-SWCNT electrical interactions. Additionally, by measuring the contact resistance before and after irradiation, each structure acts as its own control sample, eliminating any speculation about differences between values based on testing of different samples. The range of ions in metals will vary depending on factors such as the ion species, energy, and metal type. In order to ensure that the proper thicknesses of Ag contacts were selected, SRIM software was used to predict the range of $^{11}\text{B}^+$ in Ag, as shown in Figure 31d. The plot in Figure 31d shows the SRIM output values, plotted as the ion energy versus the projected range. The dashed lines show that at 150 keV (ion energy used in the present experiments), the expected range of $^{11}\text{B}^+$ in Ag is approximately 0.184 μm . The starred points in Figure 31d illustrate that the thin contacts (0.1 μm) are well below the projected range predicted by SRIM, and that the thick contacts (1.5 μm) are well above the projected range. Thus, it is expected that the ions should come to rest in the thick contact structures, and be transmitted through the thin structures, giving the ability to discern any changes in contact resistance resulting from ion irradiation at the Ag-SWCNT interface.

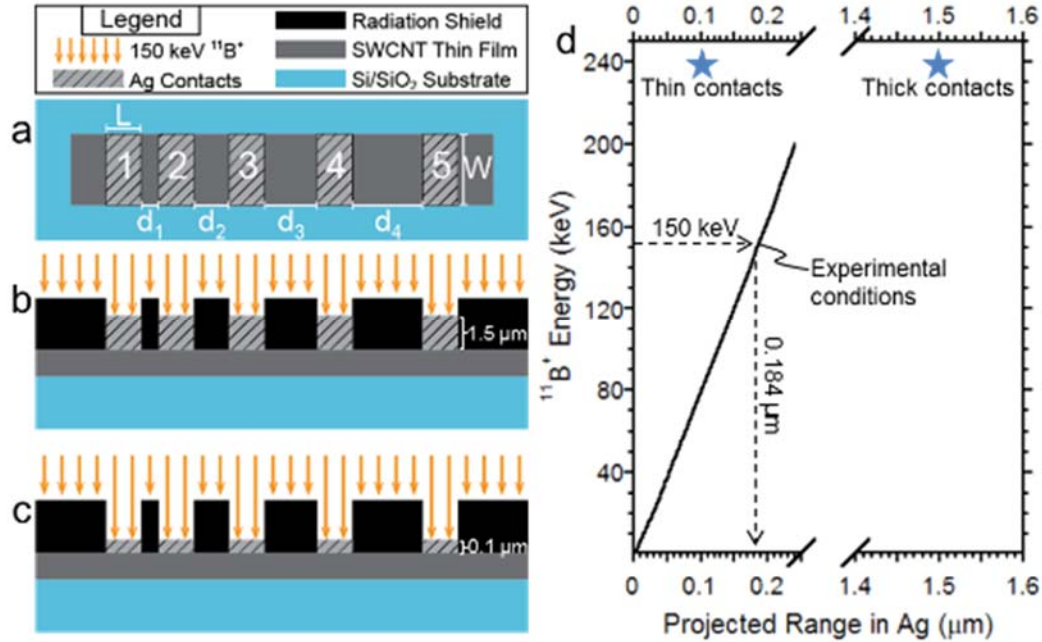


Figure 31. (a) Schematic showing a top-down view of structures fabricated for transfer length measurements (TLM) of contact resistance between Ag contacts (labeled 1-5) and SWCNT thin films, with contact lengths (L) and widths (W) of 2mm and 8mm, respectively. Cross-sectional views showing TLM structures with (b) thick (1.5 μm) and (c) thin (0.1 μm) Ag contacts during ion irradiation, with the TLM shadow mask in place (radiation shield) so that the 150 keV ¹¹B⁺ is only incident on the Ag contacts. (d) Incident ion energy is plotted versus the projected range of ¹¹B⁺ in Ag as calculated by SRIM software. Star-shaped markers identify the thickness of the contacts used in the present experiments.

Contact resistance (R_c) measurements of the structures described in Figure 31 were performed before and after ion irradiation to discern whether the ions have any impact on R_c at the Ag-SWCNT interface. The results of the TLM measurements are shown Figure 32 as the electrical resistance versus Ag contact spacing for the Ag-SWCNT structures with thick and thin Ag contacts (Figure 32a and b, respectively). The closed black squares are the measured resistance *before* ion-irradiation, and the open red squares are the measured resistance *after* ion-irradiation, with dotted lines corresponding to linear least square fits to each data set (all linear fits exhibit $R^2 > 0.996$). The sheet resistance (R_s) of the film in the channel region (between the contacts) and R_c can be extracted from plots of the electrical resistance vs contact spacing. The slope of the line is directly proportional to the sheet resistance (slope = R_s/W), and the vertical intercept (resistance value at zero electrode spacing) is $2R_c$. Work to date has shown that SWCNTs irradiated under these conditions should exhibit a significant increase in R_s .⁸ No changes are observed in the slope of the linear fits to the data (and hence, R_s) after ion irradiation, indicating that the SWCNTs in the channel were well shielded by the shadow mask and thus any changes in R_c are attributed to changes in the properties of the Ag-SWCNT interface. The contact resistance is nominally the same for both structures before irradiation: 12.8 Ω for the thin contacts and 10.4 Ω for the thick contacts. Similar values are expected as both structures were made from the same SWCNT film and equivalent Ag deposition conditions. After ion irradiation, R_c for the thick contacts remains relatively unchanged (11.4 Ω), but for the structure with thin contacts, R_c increases by $\sim 4\times$ to 50.6 Ω. The electrical results are consistent with the SRIM predictions

shown in Figure 31d, which shows that the $^{11}\text{B}^+$ should stop well within the thick Ag contacts, as illustrated in Figure 32c. Likewise, it is expected that the ions will be transmitted through the thin contacts to the underlying SWCNT film, as illustrated in Figure 32d. These results for R_c values before and after ion irradiation clearly indicate that radiation causes a significant increase in the contact resistance for the thin contact structures.

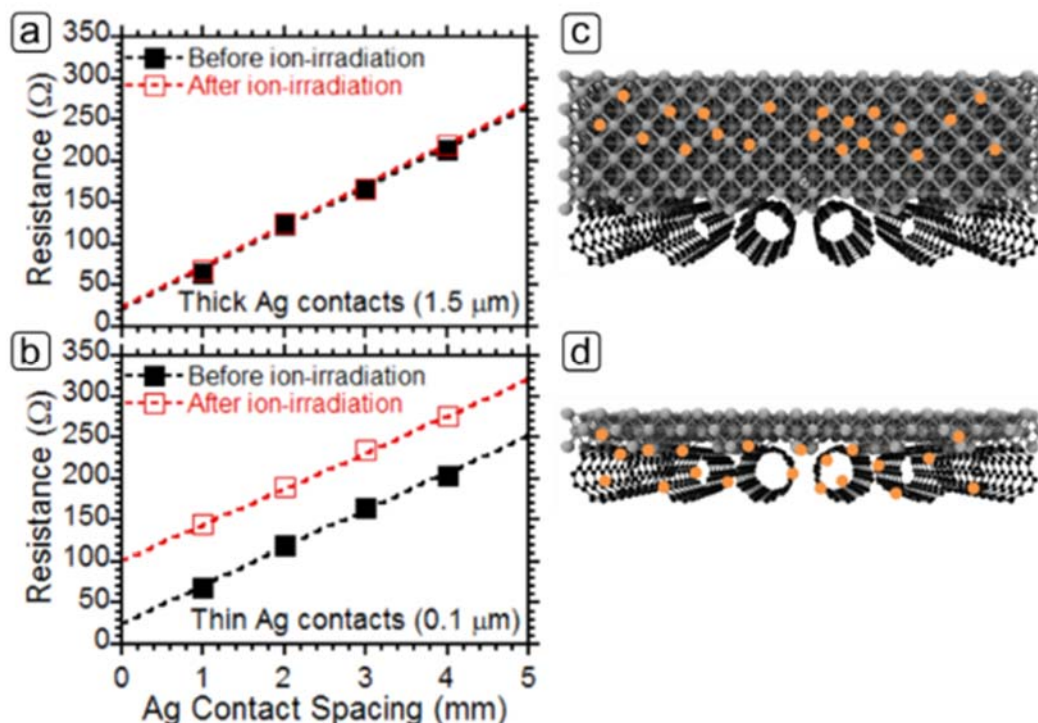


Figure 32. Plots of the measured 4-point resistance versus Ag electrode spacing for TLM structures with Ag electrode thickness of (a) 1.5 μm and (b) 0.1 μm . Resistance values for the two structures are measured both before (black square) and after (red squares) irradiation with 150 keV $^{11}\text{B}^+$, with linear fits of the data indicated by dashed lines. Conceptual illustrations show (c) thick and (d) thin metal contacts to SWCNTs, and depict ions (orange dots) either (c) stopping in the metal or (d) transmitted through the metal to the SWCNTs beneath.

Characterization of changes in the SWCNT material properties can facilitate understanding of the changes in contact resistance (or lack thereof) of the Ag-SWCNT interface in response to ion irradiation. Previous work has shown that under similar radiation conditions, both the sheet resistance and the relative defect content of the SWCNTs should significantly increase.^{8, 14, 40} Therefore, Raman spectroscopy was employed to evaluate structural changes in the SWCNTs under the contacts, as well as in the channel region, which was shielded from the ions by the TLM shadow mask. Figure 33a (thick contacts) and Figure 33b (thin contacts) are illustrations showing a zoomed in view of the irradiated structures. The regions between the contacts, which were shielded by the shadow mask, are labeled “shielded region”, and the regions where the Ag contacts were exposed to radiation are labeled “under contacts”. The illustration also demonstrates that the contacts were removed by Kapton tape to enable the Raman measurements under the contacts. The Raman peaks of interest for assessing relative defect content in SWCNTs are the D-peak ($\sim 1300\text{ cm}^{-1}$), which is related to defects, the G-peak ($\sim 1590\text{ cm}^{-1}$), and the G'-peak ($\sim 2690\text{ cm}^{-1}$). The presence of defects within the SWCNTs can be evaluated by examining relative changes in the D/G or the D/G' peak ratios

after ion irradiation. Figure 33c shows the Raman spectra for the thick-contact structure. The Raman spectra both in the shielded region and under the contacts are nearly identical, indicating no significant changes in the SWCNT material properties. Figure 33d shows the Raman spectra for the thin-contact structure. The Raman spectrum for the SWCNTs in the shielded region is also nearly identical to both spectra for the thick contact structure (Figure 31a); however, the Raman spectrum under the contacts for the thin structure shows significant changes in the prominent SWCNT peaks. The D/G peak ratio under the contacts (1.6) increases by over 5x compared to the D/G ratio in the shielded region (0.3). This is accompanied by nearly complete suppression of the G' peak in the SWCNTs under the contacts, making changes in the D/G' peak ratio difficult to quantify. These results reveal significant damage of the SWCNTs under the contacts, which suggests that the increase in R_c for the thin contact structure is due to damage to the SWCNTs by ions transmitted through the Ag contacts. Work is still ongoing to understand why structural damage of the SWCNTs under the contacts would also cause degradation in R_c , as it is not intuitive that such changes should occur.

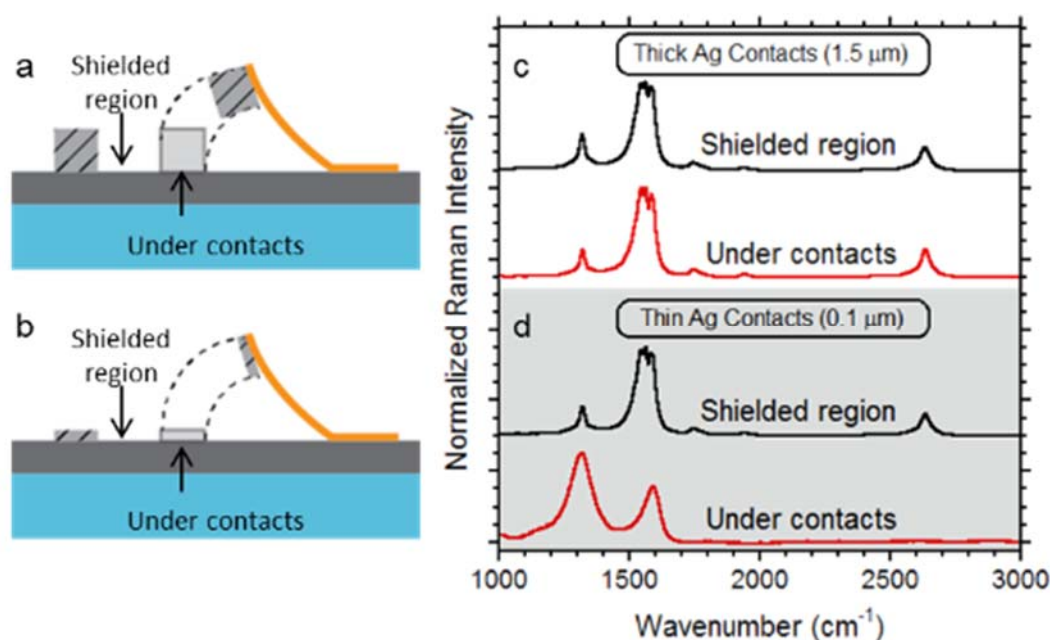


Figure 33. Schematic illustrations showing the methods for acquiring Raman data under the contacts on (a) thick and (b) thin TLM structures. The channel region, which was shielded from ion irradiation, is labeled “shielded region”. Also shown is the removal of the contacts by Kapton tape to enable Raman measurements under the contacts. The Raman spectra for the shielded region and under the contacts are also shown for (c) thick and (d) thin contact structures.

The results clearly indicate that ion irradiation can significantly impact the properties of the SWCNT-metal interface. Contact resistance increased by $\sim 4\times$ after ion irradiation for structures with thin contacts (100 nm), with essentially no change in contact resistance for structures with thick contacts (1.5 μm) under the same conditions. These changes in the contact resistance (or lack thereof) are directly correlated to structural damage in the SWCNTs, as suggested by analysis of the changes in the Raman peak ratios. The outcomes of this study have significant implications for scaled devices, where the contact resistance already limits transport, and which typically have contacts thinner than 100 nm.

4.5 Ionizing Radiation Response of Bulk CNT Conductors

Bulk CNT conductors are currently under investigation for a number of applications where the high conductivity and low mass provide significant weight savings that benefit space missions. One such application is the use of CNT conductors in coax cables, as the outer shield, center conductor or both. In one study, coaxial cables were assembled with CNT outer conductors and their radiation stability was examined. RG-58 cable assemblies, having a polyethylene dielectric (2.9 mm) and Cu inner conductor (0.81 mm) designed to yield a characteristic impedance of 50 Ω , were wrapped with a CNT outer conductor. A CNT sheet from Nanocomp Technologies, Inc. was used as the outer conductor after purification and doping with KAuBr_4 , and was secured on the cable using Teflon tape (Figure 34a). Compared to traditional Cu mesh, CNT coaxial cables offer substantial weight savings (Figure 34b), while performing close to Mil-17 spec (Figure 34c).

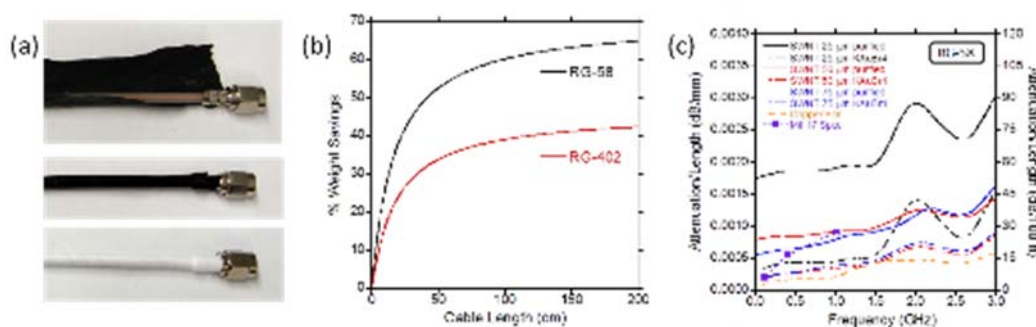


Figure 34. (a) Assembly of an RG-58 coaxial cable with CNT outer conductor offers (b) significant weight savings compared to traditional Cu mesh. (c) Purification and doping of the CNT outer conductor yields cable performance close to Mil-17 spec.

The purified, doped CNT coaxial cable was exposed to a total ionizing dose up to 5 Mrad (Co-60 approximately 1 krad (Si)/s), and studied in comparison with a reference copper coaxial cable (Figure 35). The radiation stability of the CNT coaxial cable was similar to standard Cu-based cables up to 3 GHz. These seminal radiation-response studies on bulk CNT conductors establishes their survivability in harsh radiation environments, and supports further developments that transition these findings to commercial use.

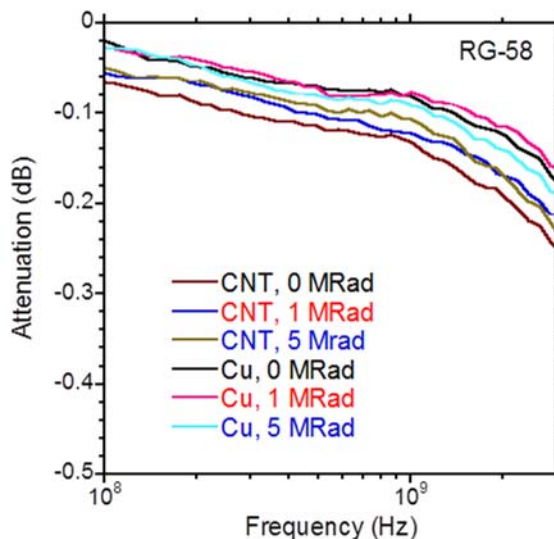


Figure 35. Examination of radiation stability up to 5 MRad in CNT coaxial cables compared to tradition Cu-based cables

5. SWCNT Healing Techniques After Irradiation

5.1 Defect Healing in Ion Irradiated SWCNT Thin-Films Through Thermal Annealing

High quality thin-films were fabricated using purified laser-Ar SWCNTs and deposited onto quartz substrates so that changes due to ion irradiation and annealing could be easily evaluated. Traditionally, SWCNT thin-film samples were purified through a 2 hr thermal oxidation treatment in air at 300°C to remove residual SDS, MCE, or solvents from the transfer method. In the current study, the samples were also subjected to a high temperature annealing treatment in H₂/Ar (5%/95%) forming gas following thermal oxidation to be consistent with the annealing conditions that will be used after ion irradiation. The change in SWCNT thin-film purity was monitored after each treatment using optical absorbance spectroscopy, and in particular, the S₁₁ peak was evaluated as it has been shown to be a good indicator of SWCNT purity.⁴¹ The S₁₁ optical transition increases in the thermally oxidized sample relative to the as-transferred sample, and a slight red shift in the wavelength corresponding to the peak maximum was observed. The sample was then subjected to a 30 min anneal at 1000°C in forming gas, which produced an additional increase in the S₁₁ peak intensity. Annealing treatments were repeated by iteratively exposing the sample to the high temperature conditions in 30 min intervals until no additional change was observed, and it was determined that 1 hr was optimal. Five nominally equivalent SWCNT thin-films were fabricated using the optimized purification method. The films were cut into 7×7 mm squares prior to transfer onto the polished quartz substrates, and Cr/Au (10/200 nm) contacts were thermally deposited onto the 4 corners of each sample to aid in the electrical characterization of the final test structures. The baseline optical absorbance, Raman spectra, and sheet resistance (R_s) were evaluated to demonstrate consistency between the five as-produced SWCNT thin-film samples. The R_s varies by ~38% across all samples likely due to non-uniformity across the entire film, compared to a 5% variation in the S₁₁ peak intensity and ~15% in both the D/G and D/G' Raman ratios, which only probe a localized volume of the sample. Therefore, all relative changes due to ion irradiation and annealing will be compared back to the respective starting sample.

Ion irradiation was used to easily and controllably impart defects in the SWCNT thin-films, as it has been previously demonstrated to produce mostly single- and dual-vacancies,⁴² and the defect density increases monotonically with fluence.¹⁴ The SWCNT samples were fabricated with an areal density of $4.2 \mu\text{g}/\text{cm}^2$, which corresponds to an average film thickness of $27.3 \pm 7.9 \text{ nm}$ based on optical interferometry. This thickness was chosen to ensure uniform and complete penetration of the ions through the SWCNT thin-film, as the projected particle stopping range for $150 \text{ keV } ^{11}\text{B}^+$ is $\sim 2 \mu\text{m}$ based on the SWCNT density and SRIM calculations.⁴³ The SWCNT thin-film samples were irradiated with increasing fluence between $1 \times 10^{13} \text{ cm}^{-2}$ to $1 \times 10^{15} \text{ cm}^{-2}$, and changes in the optical properties were evaluated. In addition to the S_{11} optical transition being more sensitive to impurities for purity analysis, it is also more sensitive to ion irradiation effects compared to S_{22} or M_{11} .¹⁴ Figure 36 shows the monotonic suppression in the SWCNT S_{11} optical transition with increasing fluence (red curves), which is consistent with previously reported values for SWCNTs synthesized by laser vaporization.^{6, 44} The samples were subsequently degassed at 200°C in forming gas for 15 min and annealed for 1 hr at 1000°C . Repeat characterization shows recovery of the S_{11} optical transition after annealing (blue curves in Figure 36). Analysis of the S_{11} peak maximum intensity relative to the as-produced value (see Figure 37) shows nearly 100% recovery in the optical transition after low dose radiation exposure (*i.e.*, $1 \times 10^{13} \text{ cm}^{-2}$) and high temperature annealing. At moderate fluences $\leq 1 \times 10^{14} \text{ cm}^{-2}$, the S_{11} peak maximum intensity is recovered to $\geq 64\%$ of the as-produced starting value. Even at high fluences (*i.e.*, $\geq 5 \times 10^{14} \text{ cm}^{-2}$) where complete suppression of the S_{11} peak is observed, recovery after annealing can restore the S_{11} peak maximum up to 37% of the as-produced value. Changes in the absolute S_{22} and M_{11} optical transitions were also characterized via optical absorption spectroscopy, and the relative change in peak maximum intensity compared to the as-produced value is nominally the same for S_{22} and M_{11} as has been reported here for S_{11} . Thus, recovery of the SWCNT physical properties can be achieved after exposure to harsh radiation conditions.

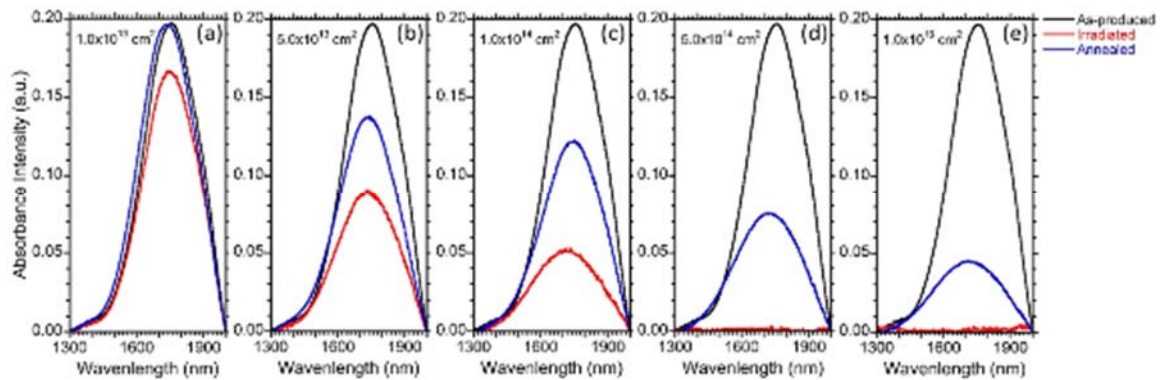


Figure 36. Analysis of the SWCNT thin-film S_{11} optical transition after ion irradiation (red curves) with $150 \text{ keV } ^{11}\text{B}^+$ to fluences of (a) $1 \times 10^{13} \text{ cm}^{-2}$, (b) $5 \times 10^{13} \text{ cm}^{-2}$, (c) $1 \times 10^{14} \text{ cm}^{-2}$, (d) $5 \times 10^{14} \text{ cm}^{-2}$, and (e) $1 \times 10^{15} \text{ cm}^{-2}$. Also plotted is the as-produced data (black curves) and annealed data (blue curves).

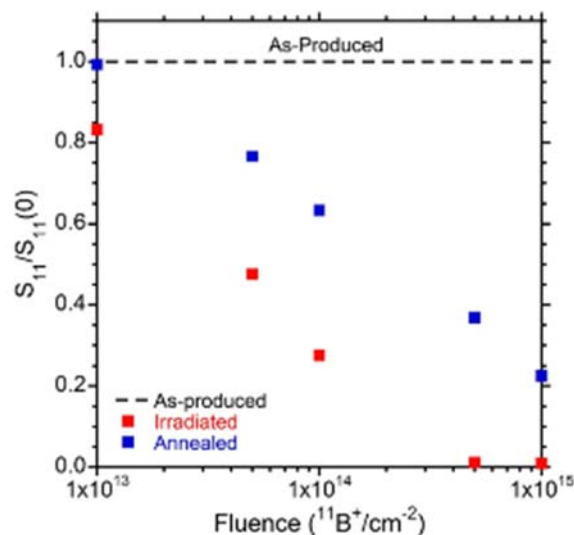


Figure 37. The peak maximum intensity of the S11 optical transition is plotted as a function of fluence. The data is normalized to the as-produced S11 peak maximum intensity of the as-produced SWCNT sample.

Raman spectroscopy was used to assess changes in the SWCNT thin-film quality after radiation exposure and annealing. The D/G' Raman ratio has been shown to be more sensitive to ion irradiation induced changes compared to D/G. Figure 38 (solid red markers) shows the change in D/G' relative to the as-produced SWCNT thin-film. The monotonic increase in D/G' as a function of fluence corroborates trends observed previously for laser SWCNTs irradiated with 150 keV $^{11}\text{B}^+$.¹⁴ Figure 38 (open red markers) shows the relative D/G' Raman response after annealing. Low dose ion irradiation (*i.e.*, $1 \times 10^{13} \text{ cm}^{-2}$) produces a less than 2x increase in the relative D/G' Raman ratio, and is further reduced by 14% after thermal annealing in forming gas. As the fluence increases, up to a 55x increase in the relative D/G' Raman ratio is observed after exposure to a fluence of $1 \times 10^{15} \text{ cm}^{-2}$. In this case, annealing produces an 87% recovery, yielding a D/G' ratio that is only 7x greater than the as-produced starting material. A similar trend is observed for the efficacy of thermal annealing to recover the normalized D/G Raman ratio after ion irradiation. Thus, thermal annealing of SWCNT thin-films provides nearly 100% recovery of the relative Raman ratios after radiation exposure up to a fluence of $1 \times 10^{14} \text{ cm}^{-2}$, and significant improvements are observed even with the exponential increase in defect damage that results from radiation exposure at extreme fluences.

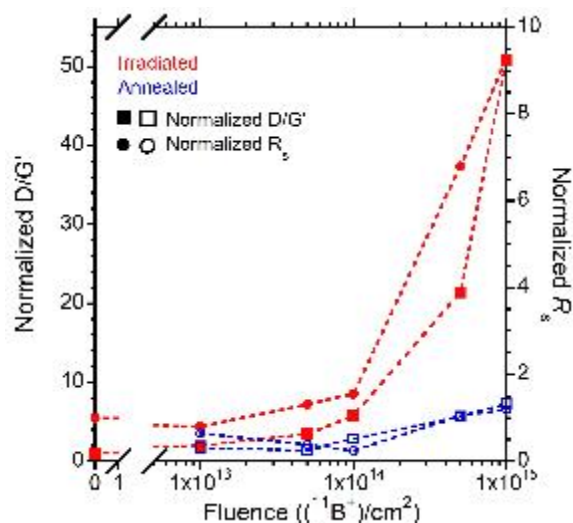


Figure 38. The relative D/G' Raman ratio (red data) and electrical sheet resistance (R_s , blue data) is plotted after ion irradiation (closed markers) and after thermal annealing (open markers). All data is normalized to the respective value of the as-produced SWCNT sample.

The relative change in the electrical sheet resistance (R_s) is overlaid with the relative change in the D/G' Raman ratio in Figure 38. The monotonic increase in R_s with increasing fluence (solid blue markers) follows nominally the same trend observed in the normalized D/G' Raman ratio, although with an intensity $\sim 5\times$ less. This relationship between the normalized D/G' Raman ratio and normalized R_s has been well established previously for ion irradiated thin-films composed of arc SWCNTs.⁸ Although ion irradiation causes an increase in R_s up to $\sim 9\times$ at a fluence of $1 \times 10^{15} \text{ cm}^{-2}$ compared to the as-produced value, thermal annealing can produce recovery of 100% or better. When irradiated with low or moderate fluences of 150 keV $^{11}\text{B}^+$ followed by thermal annealing at 1000°C in forming gas (Figure 38, open blue markers), the R_s can be reduced by up to 65% of the as-produced starting value. It is important to note that the greatest improvement was observed for the SWCNT thin-film sample irradiated to a fluence of $1 \times 10^{14} \text{ cm}^{-2}$, whereas samples irradiated to 1×10^{13} or $5 \times 10^{13} \text{ cm}^{-2}$ showed a reduction in R_s of approximately 25% and 40%, respectively. This demonstrates that the use of ion irradiation and thermal annealing to improve the electrical conductivity of a SWCNT thin-film can be tuned to optimize the electrical properties of the sample.

In the current study, R_s is fully recovered, and in some cases improved, independent of the fluence used to irradiate the SWCNT samples. Although the normalized D/G' Raman ratio follows a similar trend, up to a 7x increase in D/G' is maintained after irradiation exposure and thermal annealing at the highest fluence examined (*i.e.*, $1 \times 10^{15} \text{ cm}^{-2}$). Interestingly, the optical absorbance was the least responsive to the thermal annealing treatment. Nominally 100% recovery was observed in the optical absorbance after low dose ion irradiation at a fluence of $1 \times 10^{13} \text{ cm}^{-2}$, however, the recovery diminished from 77 – 22% as the fluence increased between $5 \times 10^{13} \text{ cm}^{-2}$ to $1 \times 10^{15} \text{ cm}^{-2}$, respectively. Recent work shows that low dose ion irradiation can cause covalent bonding between CNTs due to the introduction of 4-coordinated carbon adatoms that facilitate inter-tube cross linking, which lead to an increase in thermal conductivity.⁴⁵ Inter-tube cross-linking likely also explains the improvement in electrical conductivity shown in the current study, where the benefits of cross linking can

outweigh the remaining structural damage within an individual SWCNT. Still, the 4-coordinated adatom acts as a symmetry breaking defect, and the ability to recover structural properties becomes increasingly difficult as SWCNTs become more amorphous with fluence.⁴⁶ Thus, the observed increase in the relative D/G' Raman ratio and decrease in the maximum peak intensity of the S₁₁ optical transition are expected at high fluences, even though the electrical resistance is fully recovered. Enhanced effects of thermal annealing may be recognized in phase-pure SWCNT samples, as the adatom migration energy is proposed to vary with SWCNT chirality and electronic-type.⁴⁷

5.2 Evidence of SWCNT Defect Healing Through Spatial Profiling

Although annealing of ion irradiation-induced defects in SWCNT thin-films has been reported previously, defect profiling by Au-NP nucleation can be used as a complimentary technique to confirm annealing in irradiated SWCNTs. The high selectivity of the Au-NP nucleation to regions of ion-irradiation damage may provide a method to verify annealing by comparison of Au-NP density in irradiated SWCNTs exposed to KAuBr₄ before and after annealing. A highly purified SWCNT paper was irradiated with 150 keV ³¹P⁺ at a fluence of 5×10¹⁴ ions/cm² and divided into two portions. Following irradiation, one paper was annealed in Ar/H₂ (95%/5%) for 30 minutes at 1000 °C, while the other was placed in a vacuum oven (100 °C, ~100 mTorr). Both the irradiated and the annealed SWCNT papers were exposed to 0.01 M KAuBr₄ for 30 seconds, rinsed with DI H₂O, and dried in vacuum at 100 °C for 2 hours. The samples were subsequently analyzed via SEM for analysis of Au-NP nucleation. The irradiation conditions (*i.e.*, fluence, incident ion, etc.) used in the current study were selected to impart significant damage in the SWCNTs so that an effect of annealing would be apparent.

A strong correlation between Raman modes and Au-NP density has previously been established, showing that the degradation in the Raman modes tracks directly with increasing Au-NP density. Thus, for the irradiated SWCNT paper with high defect density, a high Au-NP density is expected. However, if the Raman modes are restored under the selected annealing conditions, then it follows that a low density of Au-NPs may be expected in the annealed SWCNT paper. Representative SEM images (50,000× magnification) of the irradiated and annealed samples after exposure to KAuBr₄ are shown in Figure 39. A high density of Au-NPs is observed for the irradiated SWCNT paper (see Figure 39a), while the irradiated and annealed portion shows virtually no Au-NP nucleation (see Figure 39b). These preliminary results indicate that the Au-NP nucleation technique enables rapid assessment of defect annealing, and may be used in conjunction with, or as an alternative to, Raman spectroscopy analysis for verification of defect annealing in SWCNTs.

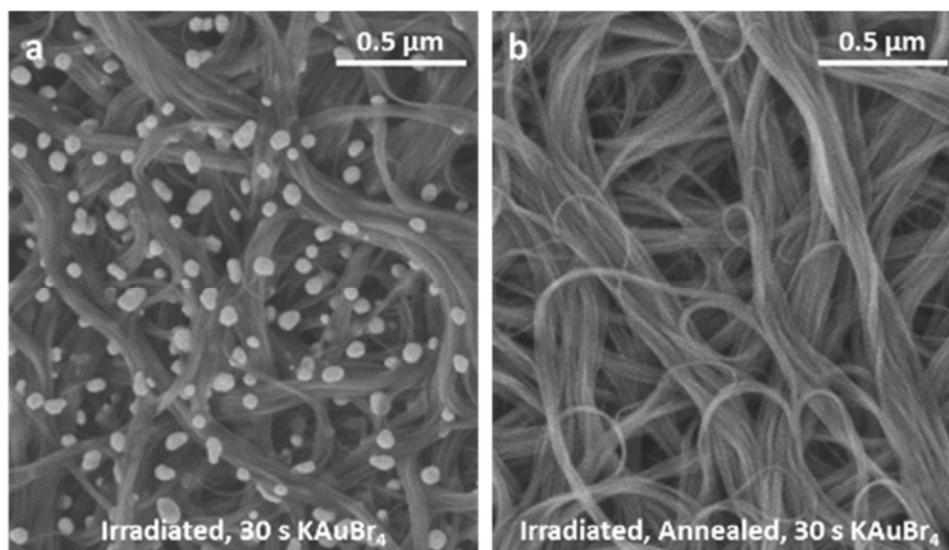


Figure 39. SEM images at 50,000 \times magnification of a purified SWCNT paper irradiated with 150 keV $^{31}\text{P}^+$ at a fluence of 5×10^{14} ($^{31}\text{P}^+$)/ cm^2 and exposed to 0.01M $\text{KAuBr}_{4(\text{aq})}$ for 30 seconds (a) before annealing and (b) after annealing in Ar/H at 1000 $^{\circ}\text{C}$ for 30 min.

6. Molecular Dynamics Simulations

6.1 Threshold Displacement Energies (E_d) in Graphene and SWCNTs

The minimum kinetic energy an atom must acquire to be displaced from its lattice site is the threshold displacement energy E_d . It plays a central role within the theoretical frameworks and computational tools used to calculate and predict the effects of different types of irradiation on the physical properties of a material. Precise knowledge of E_d as a function of chirality is a critical experimental input parameter to enable irradiation induced modification of carbon nanostructure properties, such as controlled vacancy formation or direct substitutional doping. Larger threshold energies imply higher radiation stability and a chiral map of E_d could bring important new insights to help guide the design and modification of these nanostructured materials for use in radiation environments.

A computational toolkit was developed for studying ion and electron irradiation of nanostructures using classical molecular dynamics (MD) and was used to determine the E_d for graphene and 216 different (n, m) SWCNT chiralities, with $5 \leq n \leq 20$ and $0 \leq m \leq n$.⁴⁸ The objective of this work was to provide simulation data generated with conditions that permit direct comparison to the growing body of experimental data of normally incident electron or ion irradiation damage in carbon nanostructures. Therefore, we simulated two normally incident orientations, in which the particle (carbon or electron) is directed downward on a SWCNT leading to a PKA displacement in the radially inward direction towards the SWCNT axis (see Figure 40a). Our third series of simulation data, in which simulated electron irradiation causes a radially outward displacement, provide additional insight into the mechanisms that dictate the chirality-dependent E_d .

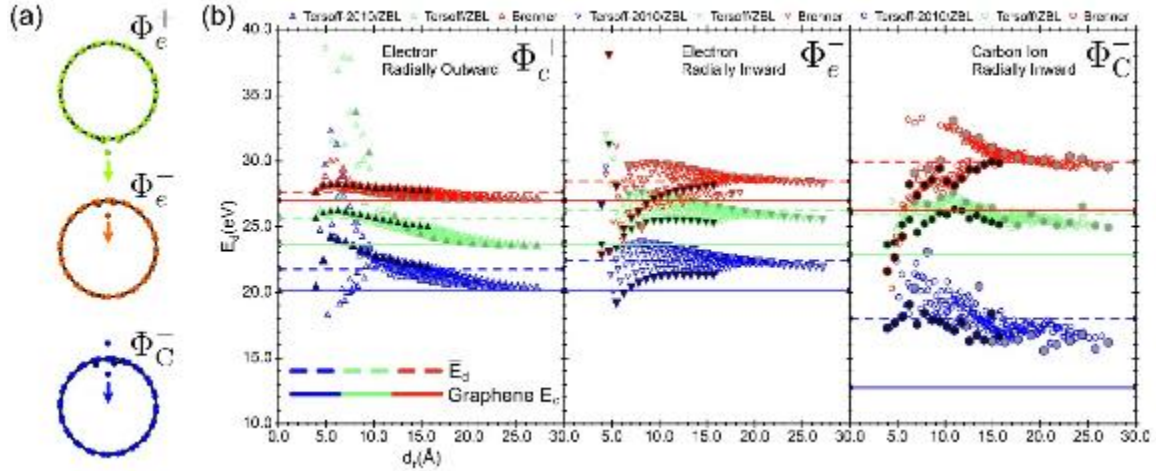


Figure 40: Three variations in simulation conditions involving different irradiation particles (electron or carbon ion) and direction of momentum transfer (radially in (−) vs. out (+)) along with its corresponding symbolic representation for the model: Φ_e^+ , Φ_e^- , Φ_C^- . Threshold displacement energy E_d as a function of nanotube diameter for the nine combinations of irradiation particles, direction, and empirical potentials: The E_d for electron irradiation with PKA momentum transfer directed radially (a) outward, away from the nanotube axis and (b) inward, towards the nanotube axis, and (c) Carbon ion irradiation with ion-PKA momentum transfer directed radially inward. The zigzag chirality markers are filled in with black and the armchair markers with gray. The dashed lines show the mean E_d (\bar{E}_d) values for each set of conditions. The solid lines are the E_d values obtained for graphene at each simulated irradiation condition. Figure taken from Ref. 48.

Figure 40(b) shows the diameter dependent E_d values determined for graphene and SWCNTs using MD simulations for different combinations of empirical potentials, irradiation particles, and directions of radial momentum transfer to the PKA. Comparing the electron irradiation simulations [Φ_e^+ vs. Φ_e^- in Figure 40(b)], it is evident that the change in direction of the radial momentum transfer gives rise to a change in curvature in the diameter dependent E_d trends. The most impactful aspects of these trends are that the achiral E_d values form the lower and upper E_d bounds across nearly all diameters and the achiral *type* forming the upper (lower) bound changes from zigzag (armchair) when the radial momentum transfer direction changes from Φ_e^+ to Φ_e^- . Comparing the electron and carbon ion irradiation simulations with radially inward PKA momentum transfer [Φ_e^- vs. Φ_C^- in Figure 40(b)], a reduction in the graphene E_d for all three interatomic potentials and a reduction in the average SWCNT E_d for both Tersoff parameterizations, which include the ZBL correction, is observed. The fact that the graphene E_d value reduces slightly for all three potentials suggests that the ion continues to repel the PKA following knock-on (or screens the attractive forces that normally return the PKA to its original lattice site) thereby reducing the peak kinetic energy needed to be displaced. In the Tersoff/ZBL Φ_C^- results, more randomness in E_d for chiral SWCNTs is observed, likely due to slight misalignment in the ion trajectory, but the bounding of the E_d values by the armchair SWCNTs (gray filled) at the upper end and by the zigzag SWCNTs (black filled) at the lower end, is preserved. Therefore, this parameterization suggests essentially no difference, within error, between the E_d for electron and carbon ion irradiations. In contrast, the Tersoff-2010/ZBL parameterization results in Φ_C^- E_d values that are considerably smaller (2-7 eV) than the corresponding Φ_e^- results and the achiral SWCNTs only set the lower E_d bound. These findings lead to significant uncertainty regarding the dynamics of near-threshold carbon ion irradiations. Depending on the choice of potential, the curvature of the SWCNTs has minimal effect on the E_d for carbon ion irradiations (Tersoff/ZBL) or a very significant

effect (Tersoff-2010/ZBL), and therefore warrants additional *ab initio* or experimental investigation.

Several equilibrium (before knock-on) and time-dependent (following knock-on) structure properties of the PKA were calculated and analyzed to ascertain the physical origin of the chirality and diameter dependent trends as well as their dependence on the direction of radial momentum transfer to the PKA. The results reveal a compelling correlation between the E_d trends and the median PKA nearest-neighbor bond length. Figure 41(a) shows a snapshot 5 fs following simulated knock-on of the time-dependent PKA bond lengths for all 216 chiralities for both Φ_e^- and Φ_e^+ simulations. Following knock-on, the diameter and chirality dependent trends of the median bond length transforms in a manner consistent with the diameter dependent trends of the simulated E_d for both Φ_e^- and Φ_e^+ simulations. Specifically, the diameter dependent trends of E_d are mirrored across all three bond lengths for both Φ_e^- and Φ_e^+ , with decreasing (increasing) E_d /bonds with increasing d_t for Φ_e^+ (Φ_e^-) simulations. Next, the spread in E_d across each chiral series ($n, m \leq n$) decreases with increasing n and a similar trend is observed for the spread in the chiral series for the median bond length (see Figure 41(a)). However, the most convincing argument pointing to a physical connection between the PKA E_d and median bond length is the correlation in the upper and lower bounds of both the E_d and median bond length data. In this case, the achiral SWCNTs align with the upper and lower bounds in the electron irradiation simulations. Also, an interchange of the achiral *type* (armchair vs. zigzag) forming the upper and lower bounds is evident upon changing the direction of the radial momentum transfer to the PKA. Thus, the physical origin of the E_d trends appears to be correlated to the time-dependent evolution of the median PKA bond lengths.

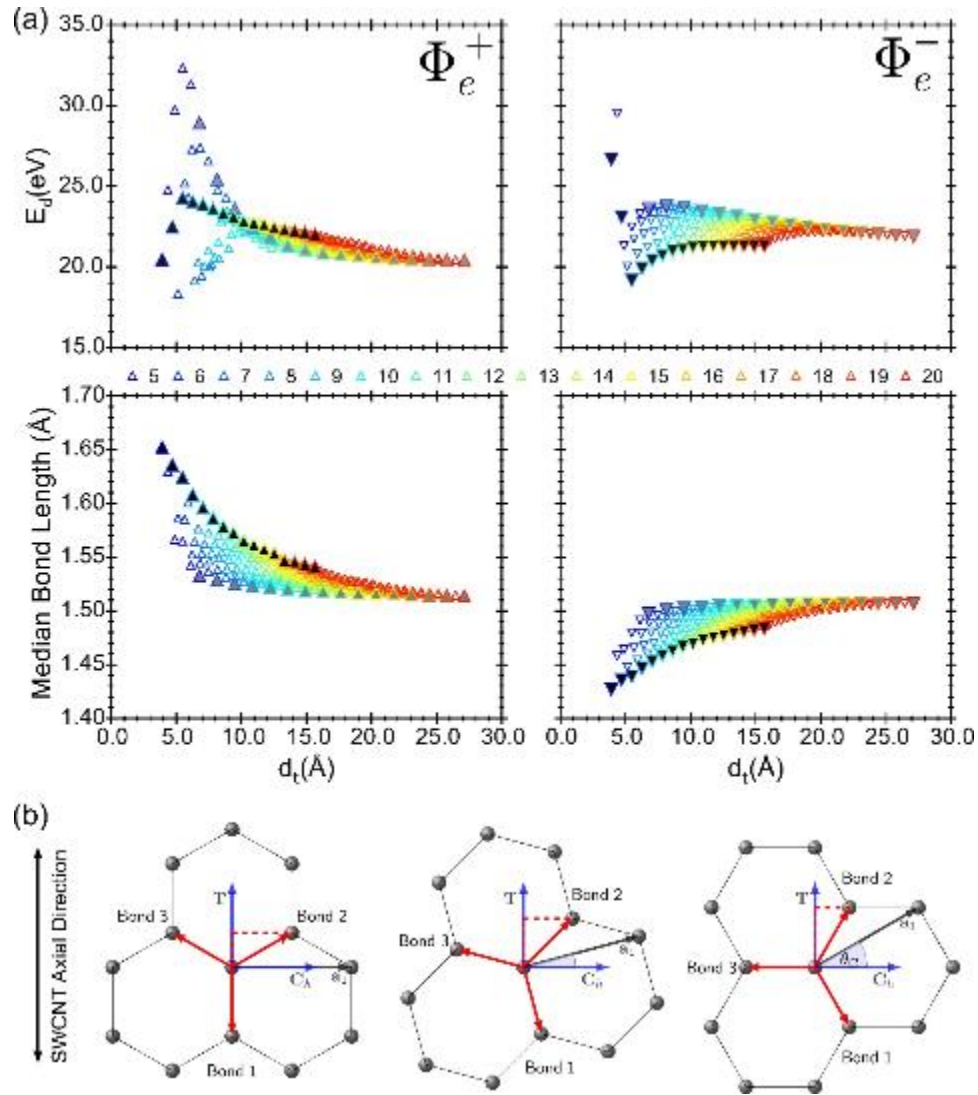


Figure 41: (a) Threshold displacement energy E_d and snapshots of the time-dependent changes in the median PKA nearest-neighbor bond length 5 fs following simulated knock-on for electron irradiation simulations. The zigzag chirality markers are filled in with black and the armchair markers with gray. (b) Schematic diagram showing 2D projections of the PKA and its nearest-neighbors onto the tangent plane of the PKA, highlighting the change in the orientation of the PKA's three nearest-neighbor bond vectors with respect to the SWCNT chiral vector C_h and translation vector T , as the chiral angle increases from 0° ($m = 0$) to 30° ($m = n$) for a given chiral series n . The bond vectors of the PKA's three nearest-neighbor atoms are shown in red. The projection of the bond 2 vector onto the translation vector is represented by the dashed red line in each orientation. Figure taken from Ref. 48.

Figure 41(b) shows 2D projections onto the PKA tangent plane of three different equilibrium orientations of the PKA and its three nearest-neighbor bonds as the chiral angle θ_c changes from 0° (zigzag) to 15° (chiral) to 30° (armchair). For zigzag SWCNTs, the 2D projection of one PKA bond vector (labeled bond 1) lies parallel to the SWCNT axis (represented by the translation vector T) and exhibits the least strain, while the 2D projections of bonds 2 and 3 are oriented with components along the chiral vector C_h leading to larger bond strain compared to bond 1. As θ_c increases from 0° ($m = 0$) to 30° ($m = n$), for a given chiral series n , Figure 41(b) shows that the components of the bond vectors for bonds 1 and 3 along C_h (T) increase (decrease) with increasing m , indicating a corresponding increase in bond

strain with increasing m , while the projection of the bond vector for bond 2 along \mathbf{C}_h (\mathbf{T}) decreases (increases) with increasing m , implying decreasing bond strain with increasing m . Thus, the change in bond 2 strain is opposite that of bonds 1 and 3, suggesting that the physical origin of the correlation of E_d with the median bond length is mediated by the change in the strain in the bond whose projection onto the translation vector increases with increasing chiral angle. The combined E_d dependence on the direction of radial momentum transfer and chirality/diameter trends adds a new dimension to how reported threshold displacement energies of SWCNTs are interpreted and used for other calculations. Although the diameter and chirality dependence has been previously investigated⁴⁹, the change in the chirality dependence due to the change in the direction of radial momentum transfer has not been previously reported and has been revealed through the present time-dependent structure analysis.

The results from Figure 41(b) show that the diameter dependent trends in E_d are consistent with the experimental findings of Warner *et al.*⁵⁰, which demonstrated SWCNTs exhibit increasing irradiation stability with increasing diameter under electron irradiation from a HRTEM. As their HRTEM images show, the pristine SWCNTs were irradiated with electrons directed towards the SWCNT. While many of the images suggest the first defects were generated along the SWCNT edge, any normally incident irradiation scenarios would be more consistent with the Φ_e^- irradiation simulations and not the Φ_e^+ results. As such, our findings reveal consistency with reported experiments investigating irradiation stability of SWCNTs through simulations consistent with the reported experimental setup. None of the reported E_d electron irradiation simulations from the literature have considered the scenario with the PKA momentum transfer directed radially inward. Interestingly, the strong correlation between our computational Φ_e^- E_d trends and experimental results illustrate the importance of modeling both incident directions. Furthermore, it suggests that the use of classical molecular dynamics is a credible approach for investigating irradiation effects in materials and may be an effective approach to attaining physical insight or providing predictions of experimental results that depend on relative changes or ratios in measurements.

7. Test Structures with RadHard Oxides and Modified SWCNTs for Radiation Mitigation

7.1 Radiation Response and Radiation Hardening of SWCNT & Graphene FETs

A considerable contribution of this DTRA effort was the study and mitigation of the deleterious radiation induced effects in SWCNT and graphene field effect transistors. In the seminal work by the PI's, the impact that radiation has on SWCNT-TFTs were demonstrated for ⁶⁰Co TID exposures up to 10 Mrad(Si).⁵¹ The effects observed in these devices with thick gate oxides (100 nm SiO₂) resembled those of Si MOSFETs, when conducted in vacuum, in which oxide trapped holes induced a significant negative voltage shift in the transfer characteristics of the device (Figure 42a). Contrary to Si MOSFETs, the *all-surface* properties of the SWCNTs resulted in an additional radiation induced response when TID exposure is conducted in air. Under ambient conditions, TID exposure induced the opposite effect as was observed in the sample irradiated under vacuum, with a shift in the transfer characteristics to higher gate voltage and increasing channel conductance (Figure 42b). The positive gate bias shift of the transfer characteristics results from molecular adsorbates on the

surface of the SWCNTs and SiO₂ (e.g., O₂, H₂O) that withdraw electrons from the SWCNTs leaving them increasing hole-doped.

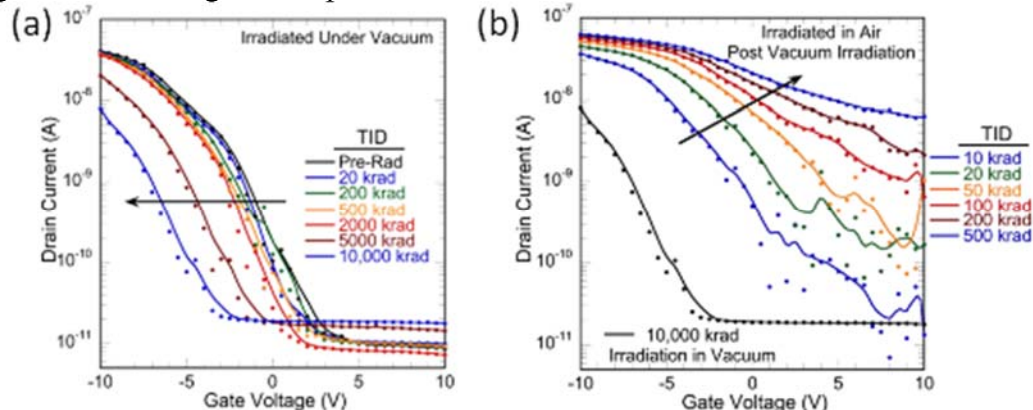


Figure 42. (a) Transfer characteristics of a back-gated SWCNT-FET with incremental total ionizing dose; (b) Transfer characteristics of the same device following air exposure and additional total ionizing dose. Figure taken from Ref. 50.

In subsequent work, similar radiation induced responses were measured in graphene FETs with thick SiO₂ gate oxides irradiated both in vacuum and in air as shown in Figure 43a and b.^{52, 53} The mechanisms that control the adsorption of molecular species onto the surface of SWCNTs and graphene are similar due to their similar hexagonally bonded, sp²-hybridized carbon lattice. These mechanisms, however, are controlled by the properties of the local environment making them an extrinsic radiation induced effect. Therefore, studying the intrinsic radiation-induced mechanisms of carbon nanomaterials (along with other 2D materials outside the scope of this project) requires the use of controlled ambient conditions either through vacuum exposures or passivation.

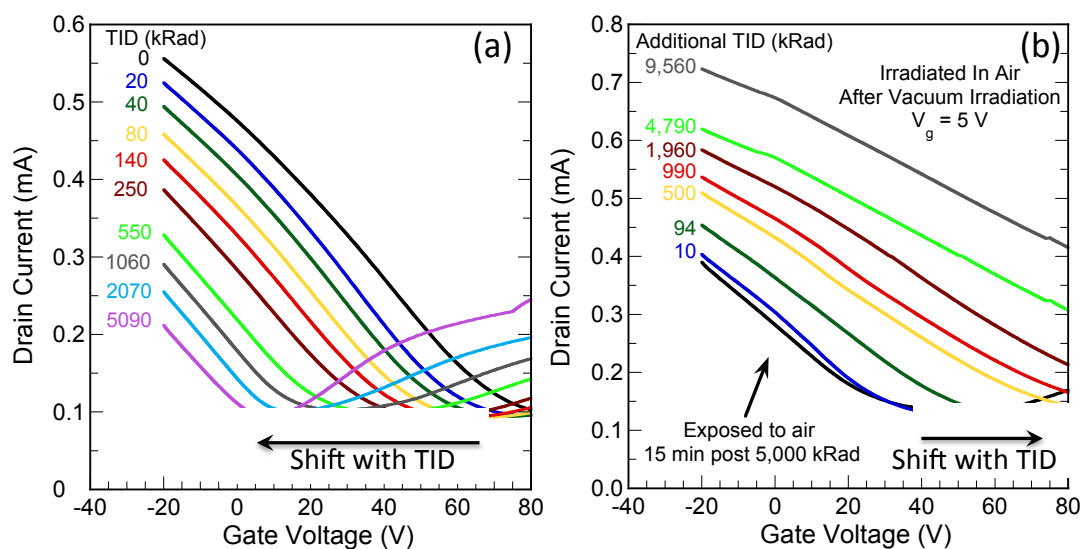


Figure 43. (a) Transfer characteristics of a back-gated graphene-FET with incremental total ionizing dose. (b) Transfer characteristics of the same device following 15 min of air exposure (black curve) and with additional TID exposure in air. Figure taken from Ref. 52.

Overcoming the deleterious impacts of TID exposure on SWCNT-TFTs was a second objective of the program. To accomplish this, standard hardening techniques were employed that included thinning down the dielectric, and employing a gate dielectric that has more favorable hole/electron trapping characteristics. To this end, SWCNT-TFTs with a novel thinned back-gate architecture were designed and fabricated with 23 nm silicon oxynitride gate dielectric layers (Figure 44).⁵² The radiation response of these devices were measured for total ionizing doses (TIDs) of Co-60 gamma irradiation up to 2 Mrad(Si). Irradiations with ± 1 MV/cm across the gate dielectric have little effect on the threshold voltage, yielding shifts of less than ± 0.25 V and no detrimental effect on SWCNT mobility or maximum drain current. A description of the measurement conditions and the results are depicted in Figure 45. The radiation hardness displayed in these devices reflects the inherent radiation tolerance of SWCNTs to ionizing radiation in combination with a thin gate dielectric, which has favorable charge trapping characteristics when exposed to radiation. Significant differences in the radiation response of SWCNT-TFT devices were observed depending on their irradiation environment, and confirm that, under controlled conditions, standard dielectric hardening approaches are applicable to carbon nanoelectronics. These results establish SWCNT (and graphene) based electronic devices as potential candidates for use in harsh radiation environments. While not yet confirmed, it is expected that the atomic layer *thinness* of these materials make them significantly less susceptible to single event effects. Circuits based on a transistors that display minimal TID response and not prone to upset would significantly benefit the space community as it could enable lower redundancies, less overhead for error corrections, and much more.

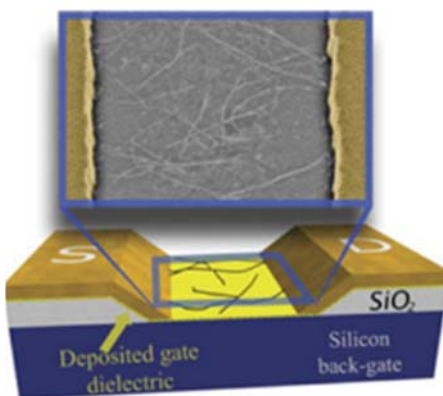


Figure 44. Schematic depicting the locally etched, back-gated SWCNT-TFT with a deposited gate dielectric, with a representative SEM of the SWCNTs in the channel region. Figure taken from Ref. 51.

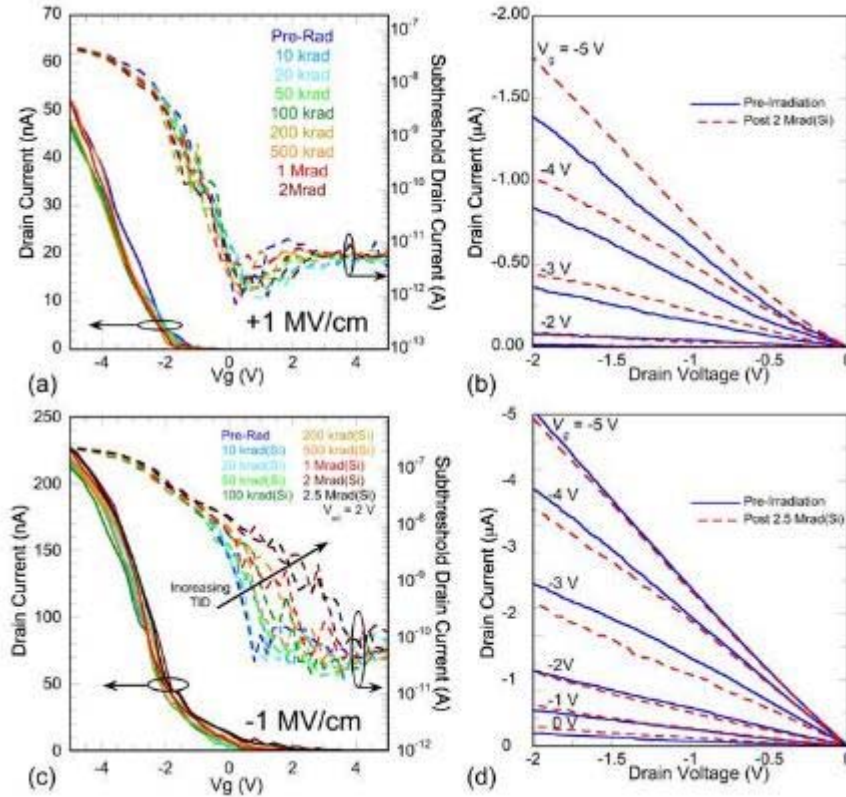


Figure 45. (a) Gate transfer characteristics following incremental TIDs. Irradiation was conducted under vacuum with a positive gate electric field of +1 MV/cm. (b) Family of curves for the device in (a) for pre-irradiation (blue, solid lines) and post 2 Mrad(Si) (red, dashed lines). (c) Gate transfer characteristics following incremental TIDs with a negative gate electric field of -1 MV/cm. (d) Corresponding family of curves for the device in (c) for pre-irradiation (blue, solid lines) and post 2.5 Mrad(Si) (red, dashed lines). The gate is biased from -5 to 0 V in +1 V steps for both (b) and (d), and the dose rate for all radiation exposures was 1.1 krad(Si)/s. Figure taken from Ref. 51.

To be a relevant radiation-hardened electronic device technology requires the devices to be scaled to sub 100 nm channel lengths and operate in the quasi-ballistic regime. In this transport regime, carriers transit the channel with minimal scattering events, and the contacts can play a large role in the overall channel conductance and potentially can lead to a different radiation response. To investigate these effects, scaled graphene FET devices were fabricated using the NRL NSI clean room facilities. Long-channel devices were first formed using standard contact photolithography processes. After testing, the devices were re-processed using electron-beam lithography to extend the source-drain contacts resulting in short channel devices. Channel lengths ranging from 35 to 100 nm were successfully patterned; four of which were wire-bonded and tested under as a function of VUV exposure. The channel lengths of these devices were 45 nm, 60 nm, 65 nm, and 100 nm. Figure 46a illustrates the transfer characteristics of the 45 nm graphene FET with incremental VUV exposure (conducted in vacuum of $<5 \times 10^6$ Torr). Like ^{60}Co irradiation, the ultraviolet photons (>8.5 eV) are absorbed in the SiO_2 gate oxide forming electron-hole pairs, and the electrons rapidly transport out of the oxide leaving behind trapped holes. The trapped holes cause a negative threshold (or Dirac point) shift in the transfer characteristics. Interesting, the transfer characteristics shift but there is little change in the mobility of the device with increasing VUV-dose. This behavior suggests that resistance at the contacts limits the device

conductance, and therefore, trapped charges in the gate oxide do not degrade the quasi-ballistic transport in the channel. In collaboration with I.S. Esqueda, a Landauer based transport model that accounts for radiation-induced changes in the carrier mean free path has been developed and used to understand the basic mechanisms associated with the measured radiation response as device channel lengths scale below the channel mean free path.⁵⁴

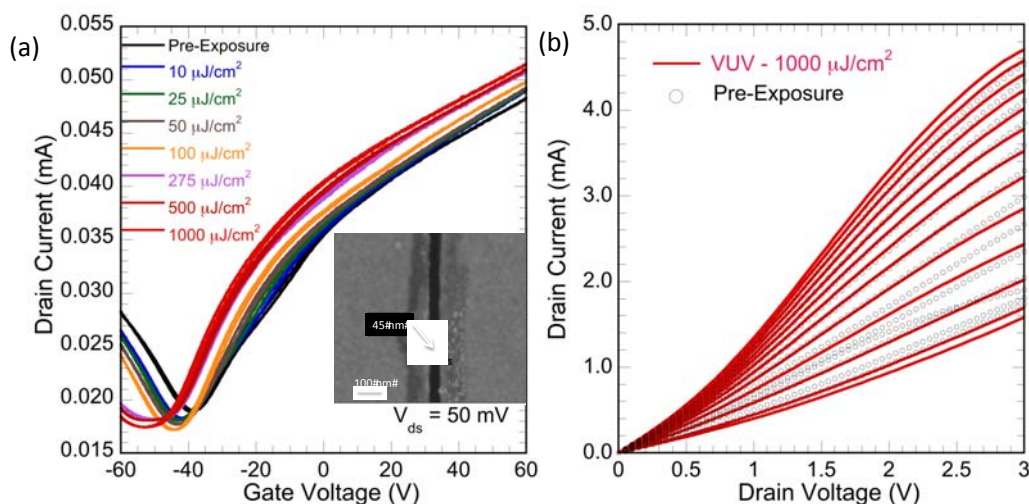


Figure 46. (a) Transfer characteristics of a graphene FET with a 45 nm channel length (5 μm channel width) with incremental vacuum ultraviolet (VUV) exposure. Inset: SEM image of the channel region confirming the 45 nm channel length. (b) Family of curves for the same graphene FET both pre-exposure (black circles) and post 1000 $\mu\text{J}/\text{cm}^2$ VUV exposure. Figure taken from Ref. 53.

Additional modeling work in collaboration with Ji Ung Lee (SUNY Polytechnic Institute), approaches the modeling of radiation effects in SWCNT FETs more rigorously, but with significantly simplified structures.⁵⁵ Specifically, the transport properties of a suspended SWCNT-FET were modeled using the non-equilibrium Green's Function formalism (NEGF). NEGF is well suited for studying quantum transport as it natively includes the effects of quantum mechanical interference, tunneling and confinement; likewise, the simplicity of a suspended SWCNT (see Figure 47a) with an air dielectric allows the model to closely resemble the actual device structure. In the particular study, the effects of ionized air molecules (ionized by high-energy protons) on the transport properties of the device are modeled. This model was investigated because of a recent paper, which observed suspended SWCNT-FET transients that were characterized by a rapid degradation in drain current followed by a full recovery.⁵⁶ [ENREF 49](#) Figure 47b depicts the geometry used to quantify the field induced in the SWCNT by neighboring charged gas molecules. Using the NEGF formalism, the spatially-dependent local density of states (LDOS) may be obtained directly and is plotted in Figure 47c. The LDOS illustrates a significant band-bending in both the valance and conduction bands of the SWCNT near the ion (located at 25 nm along the x-axis and positioned at the D as labeled on the figures). This band bending reduces the DOS in SWCNTs, thereby acting as a barrier to hole-transport in the p-channel SWCNT-FET. These results are consistent with previously reported experimental data by Bushmaker et al. in

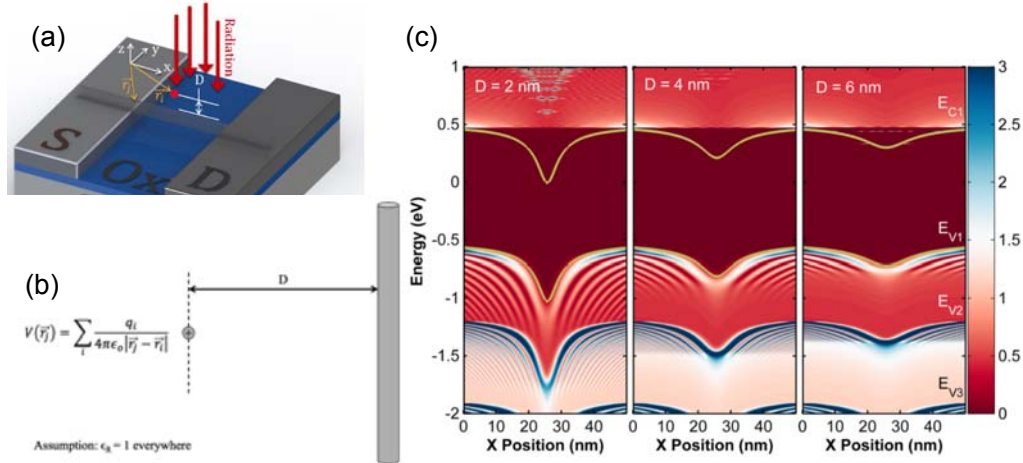


Figure 47: (a) Schematic of the suspended SWCNT-FET, (b) geometry assumed to calculate the effective field induced by the ion, and (c) the SWCNT local density of states (LDOS) as a function of position along the SWCNT length (assumed to be 50 nm). Figure taken from Ref. 53.

7.2 Radiation Effects On SWCNT-Based Antennas

Based on conductivity and thickness requirements, an NPRL's laser vaporized SWCNT-based thin-film antenna structure was fabricated using KAuBr₄ as the dopant. The return loss of the fabricated SWCNT-antenna was characterized as an indication of the resonant and RF signal strength of the antennas.

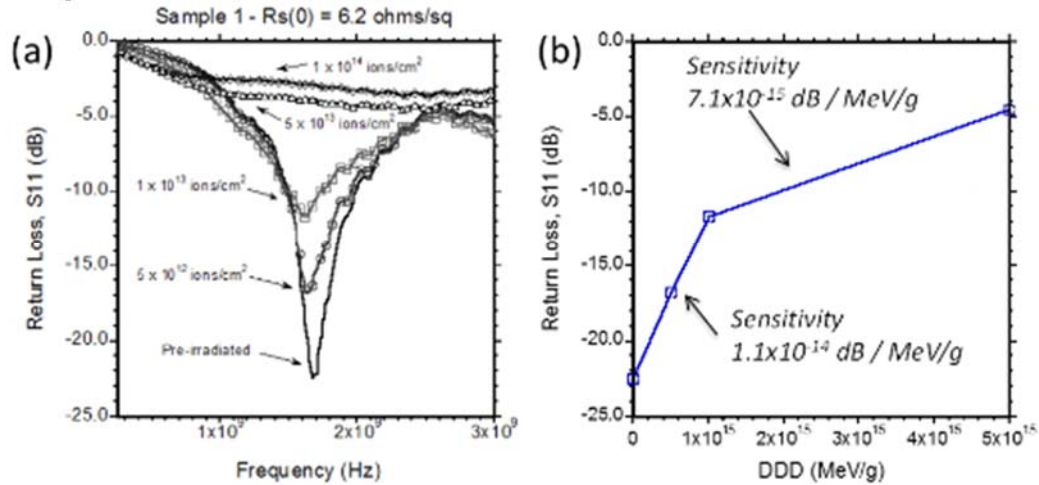


Figure 48. (a) Return loss of SWCNT thin-film antennas with increasing fluence. (b) Peak return loss of SWCNT-based thin-film antenna as a function of displacement damage dose (DDD).

Figure 48(a) shows the return loss of the fabricated monopole KAuBr₄-doped SWCNT thin-film antenna as it is irradiated with a logarithmically increasing fluence of $^{11}\text{B}^+$ ions with energy of 150 KeV, at a constant current of 10 μA . The decrease in conductivity that is observed in doped SWCNT thin-films is responsible for the degradation of the frequency response of the SWCNT antenna. Figure 48(b) also shows that the maximum signal strength of the return loss, at the frequency of resonance, decreases as the SWCNT thin-film antennas are irradiated. The maximum return loss decreases at rate of 1.1×10^{-14} dB / MeV/g for a DDD value less than 1×10^{15} MeV/g, reaching a value of -5dB at a DDD of $\sim 5 \times 10^{15}$ MeV/g.

As a result of this work, a patent opportunity has been identified where a resonant SWCNT thin-film antenna can be used as a remote wireless sensor and transmitter. The uniqueness of the invention is that the resonant SWCNT thin-film antenna structure is used both as the sensing and transmitting element, reducing system complexity and cost. In addition to sensing radiation, as shown in the example above, the thin-film antenna can be further modified to be able to sense other environmental factors that affect its conductivity and resonance characteristics.

4. IMPACT

Understanding the fundamental mechanisms and radiation response of CNTs, and determining if there is a method to mitigate such effects, is critical to the incorporation of these nanomaterials into C-WMD applications. The major impact and accomplishments of this program include:

- Optimized column chromatography and selective dispersion procedures for the fabrication of electronic-type-separated SWCNTs from multiple synthetic sources spanning the typical range of diameters for SWCNTs.
- Developed a procedure for post-separation surfactant removal, so that the intrinsic properties of the SWCNTs could be studied in subsequent radiation studies.
- Determined that the SWCNT degradation on exposure to displacement damage dose effects depends on the inter-vacancy length, L_v , which is diameter and chirality specific.
- Proposed a mechanism that explains doping in electronic-type-separated SWCNTs based on redox potentials, thus demonstrating that S-SWCNTs are more susceptible to doping compared to M-SWCNTs, which results in the highest relative change in conductivity after doping.
- Showed that the rate of degradation in ion irradiated electronic-type-separated SWCNTs is independent of electronic-type or changes in conductivity due to ionic doping.
- Developed an electroless Au tagging procedure that allows for the spatial defect profiling of ion irradiated SWCNTs.
- Identified thermal imaging as a non-contact alternative to electroless Au-tagging for characterizing ion irradiation induced defects in CNT materials, which relates changes in the material resistance after radiation exposure to changes in temperature under various bias conditions. This technique may be exploited in future applications for lab on chip applications where controlled, localized heating is required.
- Demonstrated that short-channel graphene FETs shows little mobility degradation with VUV-exposure suggestive of contact-limited quasi-ballistic transport. These results demonstrate the importance of understanding the radiation response at the contacts for scaled CNT devices, where R_c has been shown to increase by over an order of magnitude after ion irradiation exposure.
- Fundamental studies on bulk CNT conductors (*i.e.*, CNT coax cables) establishes their survivability in harsh radiation environments and supports further developments that transitions these findings to commercial use.
- Optimized annealing conditions for SWCNT thin-films, showing near-complete recovery in both the physical properties and improvement in the electrical properties after ion irradiation and thermal annealing.

- Developed computational molecular dynamics (MD) toolkit for studying ion and electron irradiation effects in nanostructured materials, including new methods for quantifying the threshold displacement energy (E_d) in graphene and SWCNTs.
- Calculated chirality dependent threshold displacement energy (E_d) for graphene and 216 SWCNT chiralities using classical MD for 9 combinations of irradiation particle, empirical potential, and direction of radial momentum transfer.
- Generated chirality-mapped, E_d color maps to visualize E_d chirality dependence for each set of model conditions.
- Computed displacement probability (P_d) as a function of the initial ion kinetic energy and the PKA kinetic energy at knock-on for a subset of chiralities.
- Established a physical connection between the PKA E_d and median bond length describing the observed chirality- and diameter-dependent trends.
- Demonstrated the effects of molecular dopants on SWCNT and graphene based transistors during radiation exposure and conducted the first vacuum irradiations of the devices to reveal the intrinsic radiation response is similar to other semiconductor materials.
- Designed a back-gated SWCNT transistor architecture employing a scaled silicon oxynitride (SiON) dielectric that displayed superior radiation tolerance due to the reduced trapped charge density and tendency of the SiON to trap both electrons and holes thereby maintaining a net charge neutrality.
- Fabricated SWCNT antennas for high frequency sensing applications, which are modulated by environmental changes to their electrical conductivity.

5. FUTURE WORK

The integration of low-dimensional nanomaterials (LDNs) into logic and memory devices has transformative potential in low-power, high-speed electronic systems. Such LDNs include 1-dimensional single-wall carbon nanotubes (CNTs), and 2-dimensional graphene and transition metal dichalcogenides (*e.g.*, MoS₂). While there have been studies on the impact of radiation exposure to the LDN channels in nanoelectronic devices, recent results have shown that performance in such devices is predominantly determined by carrier injection at the metal contacts. Thus, it is critical that fundamental research investigate the impact of radiation on metal contact-LDN interfaces. It is proposed that advanced characterization structures and modeling techniques be used to quantitatively correlate the relative contribution of metal contact-LDN interfaces on the overall nanoelectronic device performance, and determine how such interfaces are affected by radiation exposure under relevant missile or space environments for combating weapons of mass destruction (C-WMD). A series of unique characterization structures with different LDNs will be fabricated and used to evaluate how the radiation-induced defect type and density at the contact interface influence the fundamental transport mechanisms. This would leverage the molecular dynamics toolkit, developed under the current DTRA funding, so that radiation-induced defects in LDNs can be modeled, allowing for defect types with and without metal contacts to be identified and to explore the collision dynamics associated with damage and post-annealing processes. These advancements may be coupled with the exploration of passivation materials that mitigate the radiation-vulnerabilities unique to LDNs due their all-surface structure, while maintaining device performance in operational environments. Additionally, the quantification of the radiation-response in scaled LDN transistors and complementary circuits is crucial for advancing toward the ultimate goal of the science for

protection Thrust Area, in which the consequences of WMDs are reduced by implementation of LDN-based devices that are radiation-hardened and immune to single event effects. To this end, the study of aggressively scaled integrated circuits from LDNs may be performed, including total ionizing dose effects (TID) and single event effects (SEEs). Overall, through investigation of metal contact-LDN interfaces, passivation coatings, and scaled LDN devices and circuits, this proposed future work will result in a more complete picture of the radiation-response in nanoscale logic and memory devices comprised of LDNs.

6. PARTICIPATING AND OTHER COLLABORATING ORGANIZATIONS

Considerable exchange of technological and experimental data took place between RIT and NRL, which was managed through a CRADA.

7. PERSONNEL SUPPORTED

Last Name	First Name	Organization	Personnel Type	Graduated
Landi	Brian	RIT	PI	n/a
Hubbard	Seth	RIT	Co-PI	n/a
Cress	Cory	NRL	Co-PI	n/a
Messenger	Scott	NRL	Co-PI	n/a
Jarosz	Paul	RIT	Postdoctoral Fellow	n/a
Puchades	Ivan	RIT	Postdoctoral Fellow	n/a
Schauerman	Chris	RIT	PhD, Sustainability	May 2013
Ganter	Matt	RIT	PhD, Sustainability	May 2013
Cox	Nathanael	RIT	PhD, Microsystems Engineering	Exp. 2016
Kassis	Mike	RIT	Undergraduate	May 2011
McCormick	Shannon	RIT	Undergraduate	May 2012
Shaukat	Aalyia	RIT	Undergraduate	May 2012
Helenic	Alysha	RIT	Undergraduate	May 2013
Doucett	Amanda	RIT	Undergraduate	May 2014
Matthews	Olivia	RIT	Undergraduate	May 2014
Soule	Karen	RIT	Undergraduate	May 2015
Stempien	Alana	RIT	Undergraduate	May 2015
Miller	Michael	RIT	Undergraduate	May 2015
Piscitelli	Alicia	RIT	Undergraduate	Exp. May 2016
Goodman	Sheila	RIT	Undergraduate	Exp. May 2016
Schaake	Nick	RIT	Undergraduate	Exp. May 2016
Rossi	Jamie	RIT	Research Staff	n/a
Mastrangelo	Tom	RIT	Research Staff	n/a
Merrill	Andrew	RIT	Research Staff	n/a
Staub	Jason	RIT	Research Staff	n/a
Rollins	Holly	RIT	Administrative Staff	n/a

Hart	Stephanie	RIT	Administrative Staff	n/a
Best	Jeremy	NRL	PhD	May 2013
McMorrow	Julian	NRL	Postdoc	n/a
Schmucker	Scott	NRL	Postdoc	n/a
Guyette	Andrew	NRL	Research Engineer	n/a
Weaver	Brad	NRL	Research Scientist	n/a
Colbertson	James	NRL	Research Staff	n/a
Ma	David	NRL	Research Staff	n/a
Mann	James	NRL	Research Staff	n/a

8. PATENTS, PUBLICATIONS, AND PRESENTATIONS

8.1 Patents

1. Puchades, I., Landi, B.J., Rossi, J.E., Cress, C.D. "Senstenna: Thin-film wireless sensor antennas." Patent disclosure submitted to the RIT Intellectual Property Management Office, February 2016.

8.2 Manuscripts in Preparation

1. Puchades, I., Rossi, J.E., Cress, C.D., Landi, B.J. "Carbon nanotube-based antenna sensors." *Manuscript in preparation*, 2016.
2. Puchades, I., Rossi, J.E., Cox, N.D., Bucossi, A.R., Soule, K.J., Cress, C.D., Landi, B.J. "Effects of ion irradiation on chemically doped electronic-type-separated single-wall carbon nanotubes." *Manuscript in preparation*, 2016.
3. Merrill, A., Cress, C.D., Rossi, J.E., Cox, N.D., Puchades, I., Landi, B.J. "TASR: Toolkit for Atomistic Simulation with Radiation". *Manuscript in preparation*, 2016.
4. Merrill, A., Cress, C.D., Rossi, J.E., Cox, N.D., Puchades, I., Landi, B.J. "scikit-nano: Python toolkit for generating and analyzing nanostructure data". *Manuscript in preparation*, 2016.
5. Cox, N.D., Rossi, J.E., Puchades, I., Merrill, A., Cress, C.D., Landi, B.J. "Assessing the effects of ion irradiation on the contact resistance between Ag and single-wall carbon nanotubes." *Manuscript in preparation*, 2016.
6. Rossi, J.E., Soule, K.J., Cleveland, E., Schmucker, S., Cress, C.D., Landi, B.J. "Large-scale removal of surfactant from aqueous dispersions of single-wall carbon nanotubes." *Manuscript in preparation*, 2016.
7. Rossi, J.E., Cress, C.D., Goodman, S.M., Puchades, I., Cox, N.D., Merrill, A., Landi, B.J. "Defect healing in single-wall carbon nanotube thin-films through high temperature thermal annealing." *Manuscript in preparation*, 2016.
8. Rossi, J.E., Cress, C.D., Puchades, I., Cox, N.D., Merrill, A., Landi, B.J. "Thermal response of single-wall carbon nanotubes as a function of defect density." *Manuscript in preparation*, 2016.
9. Rossi, J.E., Puchades, I., Cox, N.D., Merrill, A., Cress, C.D., Landi, B.J. "Effect of single-wall carbon nanotube bundle size on ionic doping and radiation stability." *Manuscript in preparation*, 2016.
10. Rossi, J.E., Piscitelli, A.L., Puchades, I., Cox, N.D., Merrill, A., Cress, C.D., Landi, B.J. "Sorting of laser vaporized single-wall carbon nanotubes using prominent separation techniques." *Manuscript in preparation*, 2016.

8.3 Journal Publications

1. Puchades, I., Lawlor, C., Schauerma, C.M., Bucossi, A.R., Rossi, J.E., Cox, N.D. Landi, B.J. "Mechanism of chemical doping in electronic-type-separated single wall carbon nanotubes towards high electrical conductivity." *J. Mater. Chem. C*, **2015**, 39, 10256-10266.
2. Merrill, A., Cress, C.D. Rossi, J.E., Cox, N.D., Landi, B.J. "Threshold displacement energies in graphene and single-walled carbon nanotubes." *Phys. Rev. B*, **2015**, 92, 075404.
3. Esqueda, I.S., Cress, C.D., Cao, Y., Che, Y., Fritze, M., Zhou, C. "The impact of defect scattering on the quasi-ballistic transport of nanoscale conductors." *J. Appl. Phys.*, **2015**, 117, 84319.
4. Schmucker, S.W., Cress, C.D., Culbertson, J.C., Beeman, J.W., Dubon, O.D., Robinson, J.T. "Raman signature of defected twisted bilayer graphene." *Carbon*, **2015**, 93, 250-257.
5. Francis, S.A., Petrosky, J.C., McClory, J.W., Cress, C.D. "Effects of proton and X-ray irradiation on graphene field-effect transistors with thin gate dielectrics." *IEEE Trans. Nucl. Sci.*, **2014**, 61, 3010-3017.
6. Rossi, J.E., Cress, C.D., Merrill, A., Soule, K.J., Cox, N.D., Landi, B.J. "Intrinsic Diameter Dependent Degradation of Single-Wall Carbon Nanotubes from Ion Irradiation." *Carbon*, **2015**, 81, 488-496.
7. Cox, N.D., Rossi, J.E., Cress, C.D., Merrill, A., Crompton, K.R., Landi, B.J. "Spatially selective Au nanoparticle deposition and Raman analysis of ion-irradiated single-wall carbon nanotubes." *J. Phys. Chem. C*, **2014**, 118, 14031-14038.
8. Schauerma, C.M., Alvarenga, J., Staub, J., Forney, M.W., Foringer, R., Landi, B.J. "Ultrasonic welding of bulk carbon nanotube conductors." *Adv. Eng. Mater.*, **2014**, 17, 76-83.
9. Francis, S.A., Cress, C.D., McClory, J.W., Moore, E.A., Petrosky, J.C. "Characterization of radiation damage in carbon nanotube field-effect transistors." *IEEE Trans. Nuc. Sci.*, **2013**, 60, 4087-4093.
10. Esqueda, I.S., Cress, C.D., Anderson, T.J., Ahlbin, J.R., Bajura, M., Ritze, M., Moon, J.S. "Modeling Radiation-Induced Degradation in Top-gated Epitaxial Graphene FETs." *Electronics*, **2013**, 2, 234-245.
11. Cress, C.D., Champlain, J.G., Esqueda, I.S., Robinson, J.T., McMorro, J.J., Friedman, A.L. "Total Ionizing Dose Induced Charge Carrier Scattering in Graphene Devices." *IEEE Trans. Nuc. Sci.*, **2012**, 59, 3045-3053.
12. Jarosz, P.J., Shaukat, A., Mastrangelo, T., Schauerma, C.M., Cress, C.D., Ridgley, R.D., Landi, B.J. "Coaxial Cables with Single Wall Carbon Nanotube Outer Conductors Exhibiting Attenuation/Length within Specification." *Micro & Nano Lett.*, **2012**, 7, 959-961.
13. Rossi, J.E.; Cress, C.D.; Helenic, A.R.; Schauerma, C.M.; DiLeo, R.A.; Cox, N.D.; Messenger, S.R.; Weaver, B.D.; Hubbard, S.M.; Landi, B.J. "Ion irradiation of electronic-type-separated single wall carbon nanotubes: A model for radiation effects in nanostructured carbon." *J. Appl. Phys.* **2012**, 112, 034314.
14. Jarosz, P.R.; Shaukat, A.; Schauerma, C.M.; Cress, C.D.; Kladitis, P.E.; Ridgley, R.D.; Landi, B.J. "High performance lightweight coaxial cable from carbon nanotube conductors." *ACS Appl. Mater. Interfaces*, **2012**, 4, 1103-1109.

15. Cress, C.D.; McMorow, J.J.; Robinson, J.T.; Landi, B.J.; Hubbard, S.M.; Messenger, S.R. "Radiation effects in carbon nanoelectronics." *Electronics*, **2012**, *1*, 23-31.
16. McMorow, J.J.; Cress, C.D.; Affouda, C.A. "Charge injection in high- κ gate dielectrics of single-walled carbon nanotube thin-film transistors." *ACS Nano*, **2012**, *6*, 5040-5050.
17. Comfort, E.S.; Fishman, M.; Malapanis, A.; Hughes, H.L.; McMarr, P.; Cress, C.D.; Bakhru, H.; Lee, J.U. "Creation of individual defects at extremely high proton fluences in carbon nanotube p-n diodes." *IEEE Trans. Nucl. Sci.*, **2011**, *58*, 2898-2903.
18. Cress, C.D.; McMorow, J.J.; Robinson, J.T.; Friedman, A.L.; Hughes, H.L.; Weaver, B.D.; Landi, B.J. "Total ionizing dose hardened carbon nanotube thin film transistors." *MRS Communications*, **2011**, *1*, 27-31.

8.4 Oral Presentations and Invited Talks

1. Cox, N.D., Rossi, J.E., Merrill, A., Crompton, K.R., Cress, C.D., Landi, B.J. "Spatially selective Au nanoparticle deposition and Raman analysis of ion-irradiated single-wall carbon nanotubes." Materials Research Society Fall Meeting and Exhibit, Boston, MA, Dec. 2014.
2. Cox, N.D. "Implementation and radiation response of single-wall carbon nanotubes in space applications." Microsystems Engineering Seminar, Rochester, NY, Oct. 2014.
3. Schmucker, S.W., Cress, C.D., Culbertson, J.C., Beeman, J.W., Dubon, O.D., Robinson, J.T. "The influence of defects on interfaces and interlayer coupling in twisted bilayer graphene." International Conference on Nanoscience and Technology, Vail, CO, Jul. 2014.
4. Cress, C.D., Schmucker, S.M., Robinson, J.T., Yakes, M.K. "Modifying contacts to carbon nanomaterials through hyperthermal ion implantation." Government Microcircuit Applications and Critical Technology Conference, Charleston, SC, Mar. 2014. (Best Paper Award)
5. Cress, C.D. "Radiation response of carbon nanoelectronics." International Conference on Small Science, Las Vegas, NV, Dec. 2013.
6. Rossi, J.E., Soule, K.J., Cox, N.D., Merrill, A., Mastrangelo, T.L., Cress, C.D., Landi, B.J. "Surfactant removal and purification of single-wall carbon nanotubes." American Institute of Chemical Engineers Annual Meeting, San Francisco, CA, Nov. 2013.
7. Cox, N.D. "Defect distributions in ion-irradiated carbon nanotubes." Microsystems Engineering Seminar, Rochester, NY, Oct. 2013.
8. Cress, C.D. "Carbon nanoelectronics: The role of dielectric trapped charges." Invited Seminar, University of Wisconsin – Madison, Madison, WI, Aug. 2013.
9. Soule, K.J., Rossi, J.E., Cox, N.D., Landi, B.J. "Surfactant removal and purification of single-wall carbon nanotubes." Rochester Institute of Technology Undergraduate Research Symposium, Rochester, NY, Aug. 2013.
10. Piscitelli, A.L., Rossi, J.E., Landi, B.J. "Separation of single-wall carbon nanotubes by column chromatography." Rochester Institute of Technology Undergraduate Research Symposium, Rochester, NY, Aug. 2013.
11. Goodman, S.M., Rossi, J.E., Landi, B.J. "Annealing defects in electronic-type-separated single-wall carbon nanotubes after ion irradiation." Rochester Institute of Technology Undergraduate Research Symposium, Rochester, NY, Aug. 2013.
12. Landi, B.J., Cress, C.D. "Assessing ion irradiation-induced defects in SWCNTs." Telluride Science Research Center Workshop on Carbon Nanotube Defects, Telluride, CO, Jul. 2013.

13. Cress, C.D. "Radiation effects in carbon nanomaterials and devices." Invited Seminar, Columbia University, New York, NY, Feb. 2013.
14. Cox, N.D. "Fabrication of back-gated single wall carbon nanotube thin-film transistors." Microsystems Engineering Seminar, Rochester, NY, Jan. 2013.
15. Rossi, J.E., Cress, C.D., Helenic, A.R.; Schauerman, C.M.; DiLeo, R.A., Cox, N.D., Messenger, S.R., Weaver, B.D., Hubbard, S.M., Landi, B.J. "Effect of ion irradiation on electronic-type-separated single-wall carbon nanotubes." Materials Research Society Fall Meeting, Boston, MA, Nov. 2012.
16. Schauerman, C.M.; Maher, T.P.; Jarosz, P.R.; Rossi, J.E.; Mastrangelo, T.L.; Landi, B.J. "Physical and Electrical characterization of single and multi wall carbon nanotube bulk networks." American Institute of Chemical Engineers Annual Meeting, Pittsburgh, PA, Oct. 2012.
17. Soule, K., Rossi, J., Cox, N., Merrill, A., Landi, B.J. "Electrical and physical characterization of single wall carbon nanotube thin-films as a function of film thickness." American Institute of Chemical Engineers Annual Meeting, Pittsburgh, PA, Oct. 2012.
18. Best, J.S., McClory, J.W., Cress, C.D., Francis, S.A., Petrosky, J. "Electron radiation damage effects on SWCNT thin films." IEEE and Nuclear Science Symposium, Anaheim, CA, Oct. 2012.
19. Rossi, J.E., Cress, C.D., Helenic, A.R., Schauerman, C.M., DiLeo, R.A., Cox, N.D., Messenger, S.R., Weaver, B.D., Hubbard, S.M., Landi, B.J. "Effect of ion irradiation on single wall carbon nanotubes as a function of electronic-type." Northeast Regional Meeting of the American Chemical Society, Rochester, NY, Sept. 2012.
20. Esqueda, I.S., Cress, C.D., Fu, Y., Zhang, J., Zhou, C., Ahlbin, J.R., Bajura, M., Boverman, G., Fritze, M. "Modeling the effect of hysteresis on aligned nanotube FETs exposed to ionizing radiation. 21st European Conference on Radiation Effects on Components and Systems, Biarritz, France, Sept. 2012.
21. Ahlbin, J.R., Esqueda, I.S., Cress, C.D., Weeden-Wright, S.L., McMarr, P.J., Hughes, H.L., Friedman, A.L., Fu, Y., Zhang, J., Wang, C., Zhou, C., Boverman, G., Bajura, M., Fritze, M. "Total Dose Effects in Aligned Carbon Nanotube Transistors with Al₂O₃ Gate Dielectrics." 21st European Conference on Radiation Effects on Components and Systems, Biarritz, France, Sept. 2012.
22. Cress, C.D.; Rossi, J.E.; Helenic, A.R.; Schauerman, C.M.; Mastrangelo, T.; Cox, N.D.; Hubbard, S.M.; Landi, B.J. "Radiation response of monodisperse single-walled carbon nanotube thin films." Carbon, Krakow, Poland, June 2012.
23. Mastrangelo, T.; Rossi, J.E.; Helenic, A.R.; Schauerman, C.M.; Landi, B.J. "Chirality enrichment and diameter control of laser-synthesized single-wall carbon nanotubes for energy applications." Materials Research Society Annual Spring Meeting, San Francisco, California, Apr. 2012.
24. Cress, C.D. "Disorder effects in carbon nanoelectronics." Invited Seminar, University of Nevada, Las Vegas, Las Vegas, Nevada, Mar. 2012.
25. Rossi, J.E.; Cress, C.D.; Helenic, A.R.; Schauerman, C.M.; DiLeo, R.A.; Cox, N.D.; Messenger, S.R.; Weaver, B.D.; Hubbard, S.M.; Landi, B.J. "Ion irradiation of electronic-type-separated single wall carbon nanotubes: A model for radiation effects in nanostructured carbon." Government Microcircuit Applications and Critical Technologies Conference, Las Vegas, Nevada, Mar. 2012.

26. Jarosz, P.; Landi, B.J.; Schauerman, C.M.; Alvarenga, J.; Moses, B.; Mastrangelo, T.; Raffaele, R.; Ridgley, R.; Shaukat, A.; Maher, T. "Fabrication and analysis of bulk CNT wires and cables." Materials Research Society Annual Fall Meeting, Boston, MA, Dec. 2011.
27. Landi, B.J.; Ganter, M.J.; Schauerman, C.M.; Jarosz, P.J.; Cress, C.D.; Raffaele, R.P.; Rogers, R.E.; Staub, J. "Electrical and thermal aspects of carbon nanotube composite electrodes." Materials Research Society Annual Fall Meeting, Boston, MA, Dec. 2011.
28. McMorow, J.J., Cress, C.D. "Semiconductor enriched single-walled carbon nanotube thin-film-transistors with High- κ dielectrics" Materials Research Society Annual Spring Meeting, San Francisco, CA, Apr. 2011.
29. Cress, C.D., McMorow, J.J., Robinson, J.T., Landi, B.J., Hubbard, S.M., Messenger, S.R. "Radiation hardening of carbon nanoelectronics" Government Microcircuit Application & Critical Technology Conference, Orlando, FL, Mar. 2011.

8.5 *Poster Presentations:*

1. Arnold, H. Cress, C.D., McMorow, J.J., Sangwan, V., Marks, T., Hersam M. "Radiation effects in graphene field-effect transistors with zirconia-organic self-assembled nanodielectrics." New Diamond and Nano Carbons Conference, Chicago, IL, May 2014.
2. Puchades, I., Ridgley, R., Landi, B.J. "Chromatographic separation of single-wall carbon nanotubes with advanced chirality enrichment for devices and electrodes." I.C. Postdoctoral Fellowship Colloquium, Washington, D.C., Apr. 2014.
3. Soule, K.J., Rossi, J.E., Cox, N.D., Merrill, A., Mastrangelo, T.L., Cress, C.D., Landi, B.J. "Surfactant removal and purification of single-wall carbon nanotubes." American Institute of Chemical Engineers Annual Meeting, San Francisco, CA, Nov. 2013.
4. Rossi, J.E., Cress, C.D., Soule, K.J., Stempien, A.C., Mastrangelo, T., Merrill, A., Cox, N.D., Schauerman, C.M., Landi, B.J. "Radiation response in single wall carbon nanotube thin-films as a function of electronic-type and diameter." Government Microcircuit Applications and Critical Technology Conference, Las Vegas, NV, Mar. 2013. (Best Poster Paper)

8.6 *Thesis/Dissertation*

1. Cox, N.D., "Enhanced metal contacts to phase pure carbon nanotube networks through chemical and physical modification." RIT PhD Dissertation Proposal, Rochester, NY, Dec. 2014.
2. Schauerman, C.M. "Functional carbon nanotubes for electrical conductors." RIT PhD Dissertation, Golisano Institute of Sustainability, 2013.
3. Best, J. S. "Electron damage effects on carbon nanotube thin films." AFIT Master's Thesis, 2013.

9. REFERENCES

1. Landi, B. J.; Raffaele, R. P. Effects of Carrier Gas Dynamics on Single Wall Carbon Nanotube Chiral Distributions During Laser Vaporization Synthesis. *J Nanosci Nanotechnol*, **2007**, 7, 883-890.
2. Tanaka, T.; Liu, H. P.; Fujii, S.; Kataura, H. From Metal/Semiconductor Separation to Single-Chirality Separation of Single-Wall Carbon Nanotubes Using Gel. *Phys Status Solidi-R*, **2011**, 5, 301-306.
3. Haroz, E. H.; Duque, J. G.; Lu, B. Y.; Nikolaev, P.; Arepalli, S.; Hauge, R. H.; Doorn, S. K.; Kono, J. Unique Origin of Colors of Armchair Carbon Nanotubes. *J Am Chem Soc*, **2012**, 134, 4461-4464.
4. Liu, H. P.; Nishide, D.; Tanaka, T.; Kataura, H. Large-Scale Single-Chirality Separation of Single-Wall Carbon Nanotubes by Simple Gel Chromatography. *Nat Commun*, **2011**, 2.

5. Mistry, K. S.; Larsen, B. A.; Blackburn, J. L. High-Yield Dispersions of Large-Diameter Semiconducting Single-Walled Carbon Nanotubes with Tunable Narrow Chirality Distributions. *ACS Nano*, **2013**, 7, 2231-2239.
6. Landi, B. J.; Ruf, H. J.; Evans, C. M.; Cress, C. D.; Raffaele, R. P. Purity Assessment of Single-Wall Carbon Nanotubes, Using Optical Absorption Spectroscopy. *J Phys Chem B*, **2005**, 109, 9952-9965.
7. Lukaszczuk, P.; Rummeli, M. H.; Knupfer, M.; Kalenczuk, R. J.; Borowiak-Palen, E. Surfactant Free Fractions of Metallic and Semiconducting Single-Walled Carbon Nanotubes Via Optimised Gel Chromatography. *Mater Res Bull*, **2012**, 47, 687-691.
8. Rossi, J. E.; Cress, C. D.; Helenic, A. R.; Schauerma, C. M.; DiLeo, R. A.; Cox, N. D.; Messenger, S. R.; Weaver, B. D.; Hubbard, S. M.; Landi, B. J. Ion Irradiation of Electronic-Type-Separated Single Wall Carbon Nanotubes: A Model for Radiation Effects in Nanostructured Carbon. *J Appl Phys*, **2012**, 112.
9. Tolvanen, A.; Kotakoski, J.; Krashennnikov, A. V.; Nordlund, K. Relative Abundance of Single and Double Vacancies in Irradiated Single-Walled Carbon Nanotubes. *Applied Physics Letters*, **2007**, 91, 173109.
10. Messenger, S. R.; Burke, E. A.; Summers, G. P.; Xapsos, M. A. Nonionizing Energy Loss (Niel) for Heavy Ions. *IEEE Transactions on Nuclear Science* **1999**, 46, 1595-1600.
11. Krashennnikov, A. V.; Miyamoto, Y.; Tomanek, D. Role of Electronic Excitations in Ion Collisions with Carbon Nanotubes. *Physical Review Letters*, **2007**, 99, 016104.
12. Burke, E. A.; Dale, C. J.; Campbell, A. B.; Summers, G. P.; Stapor, W. J.; Xapsos, M. A.; Palmer, T.; Zuleeg, R. Energy Dependence of Proton-Induced Displacement Damage in Gallium Arsenide. *IEEE Transactions on Nuclear Science*, **1987**, NS-34, 1220-1226.
13. Summers, G. P.; Burke, E. A.; Xapsos, M. A.; Dale, C. J.; Marshall, P. W.; Petersen, E. L. Displacement Damage in Gaas Structures. *IEEE Transactions on Nuclear Science*, **1988**, 35, 1221-1226.
14. Rossi, J. E.; Cress, C. D.; Merrill, A.; Soule, K. J.; Cox, N. D.; Landi, B. J. Intrinsic Diameter Dependent Degradation of Single-Wall Carbon Nanotubes from Ion Irradiation. *Carbon*, **2015**, 81, 488-496.
15. DiLeo, R. A.; Landi, B. J.; Raffaele, R. P. Purity Assessment of Multiwalled Carbon Nanotubes by Raman Spectroscopy. *J Appl Phys*, **2007**, 101.
16. Rossi, J. E.; Cress, C. D.; Helenic, A. R.; Schauerma, C. M.; DiLeo, R. A.; Cox, N. D.; Messenger, S. R.; Weaver, B. D.; Hubbard, S. M.; Landi, B. J. Ion Irradiation of Electronic-Type-Separated Single Wall Carbon Nanotubes: A Model for Radiation Effects in Nanostructured Carbon *Journal of Applied Physics*, **2012**, 112, 034314.
17. Messenger, S. R.; Burke, E. A.; Summers, G. P.; Xapsos, M. A.; Walters, R. J.; Jackson, E. M.; Weaver, B. D. Nonionizing Energy Loss (Niel) for Heavy Ions. *IEEE Transactions on Nuclear Science*, **1999**, 46, 1595-1602.
18. Gomez-Navarro, C.; De Pablo, P. J.; Gomez-Herrero, J.; Biel, B.; Garcia-Vidal, F. J.; Rubio, A.; Flores, F. Tuning the Conductance of Single-Walled Carbon Nanotubes by Ion Irradiation in the Anderson Localization Regime. *Nature Materials*, **2005**, 4, 534-539.
19. Landi, B. J.; Ganter, M. J.; Cress, C. D.; DiLeo, R. A.; Raffaele, R. P. Carbon Nanotubes for Lithium Ion Batteries. *Energ Environ Sci*, **2009**, 2, 638-654.
20. Chou, S. G.; Son, H.; Kong, J.; Jorio, A.; Saito, R.; Zheng, M.; Dresselhaus, G.; Dresselhaus, M. S. Length Characterization of DNA-Wrapped Carbon Nanotubes Using Raman Spectroscopy. *Applied Physics Letters*, **2007**, 90.
21. Fagan, J. A.; Simpson, J. R.; Bauer, B. J.; Lacerda, S. H. D.; Becker, M. L.; Chun, J.; Migler, K. B.; Walker, A. R. H.; Hobbie, E. K. Length-Dependent Optical Effects in Single-Wall Carbon Nanotubes. *J Am Chem Soc*, **2007**, 129, 10607-10612.
22. Schmucker, S. W.; Cress, C. D.; Culbertson, J. C.; Beeman, J. W.; Dubon, O. D.; Robinson, J. T. Raman Signature of Defected Twisted Bilayer Graphene. *Carbon*, **2015**, 93, 250-257.
23. Ziegler, J. F. Srim-2003. *Nuclear Instruments and Methods in Physics Research Section B: Beam Interactions with Materials and Atoms*, **2004**, 219-220, 1027-1036.
24. Muratore, C.; Reed, A. N.; Bultman, J. E.; Ganguli, S.; Cola, B. A.; Voevodin, A. A. Nanoparticle Decoration of Carbon Nanotubes by Sputtering. *Carbon*, **2013**, 57, 274-281.
25. Topinka, M. A.; Rowell, M. W.; Goldhaber-Gordon, D.; McGehee, M. D.; Hecht, D. S.; Gruner, G. Charge Transport in Interpenetrating Networks of Semiconducting and Metallic Carbon Nanotubes. *Nano Lett*, **2009**, 9, 1866-1871.
26. Barnes, T. M.; Blackburn, J. L.; van de Lagemaat, J.; Coutts, T. J.; Heben, M. J. Reversibility, Dopant Desorption, and Tunneling in the Temperature-Dependent Conductivity of Type-Separated, Conductive Carbon Nanotube Networks. *Acs Nano*, **2008**, 2, 1968-1976.
27. Kim, K. K.; Yoon, S. M.; Park, H. K.; Shin, H. J.; Kim, S. M.; Bae, J. J.; Cui, Y.; Kim, J. M.; Choi, J. Y.; Lee, Y. H. Doping Strategy of Carbon Nanotubes with Redox Chemistry. *New J Chem*, **2010**, 34, 2183-2188.
28. Lide, D. R., *Crc Handbook of Chemistry and Physics*; 87th ed.; CRC Press: Boca Raton, FL, 2006.
29. http://www.photon.t.u-tokyo.ac.jp/~maruyama/kataura/1D_DOS.html (accessed March 20, 2015).
30. Jijun Zhao, J. H., Jian Ping Lu. Work Functions of Pristine and Alkali-Metal Intercalated Carbon Nanotubes and Bundles. *Phys Rev B*, **2002**, 65, 193401.
31. Zhou, W.; Vavro, J.; Nemes, N. M.; Fischer, J. E.; Borondics, F.; Kamaras, K.; Tanner, D. B. Charge Transfer and Fermi Level Shift in P-Doped Single-Walled Carbon Nanotubes. *Phys Rev B*, **2005**, 71.
32. Chandra, B.; Afzali, A.; Khare, N.; El-Ashry, M. M.; Tulevski, G. S. Stable Charge-Transfer Doping of Transparent Single-Walled Carbon Nanotube Films. *Chem Mater*, **2010**, 22, 5179-5183.

33. Dan, B.; Irvin, G. C.; Pasquali, M. Continuous and Scalable Fabrication of Transparent Conducting Carbon Nanotube Films. *Acs Nano*, **2009**, 3, 835-843.
34. Janas, D.; Herman, A. P.; Boncel, S.; Kozioł, K. K. Iodine Monochloride as a Powerful Enhancer of Electrical Conductivity of Carbon Nanotube Wires. *Carbon*, **2014**, 73, 225-233.
35. Jarosz, P. R.; Shaukat, A.; Schauerman, C. M.; Cress, C. D.; Kladitis, P. E.; Ridgley, R. D.; Landi, B. J. High-Performance, Lightweight Coaxial Cable from Carbon Nanotube Conductors. *Acs Appl Mater Inter*, **2012**, 4, 1103-1109.
36. Michel, T.; Alvarez, L.; Sauvajol, J. L.; Almairac, R.; Aznar, R.; Mathon, O.; Bantignies, J. L.; Flahaut, E. Structural Selective Charge Transfer in Iodine-Doped Carbon Nanotubes. *J Phys Chem Solids*, **2006**, 67, 1190-1192.
37. Mistry, K. S.; Larsen, B. A.; Bergeson, J. D.; Barnes, T. M.; Teeter, G.; Engtrakul, C.; Blackburn, J. L. N-Type Transparent Conducting Films of Small Molecule and Polymer Amine Doped Single-Walled Carbon Nanotubes. *Acs Nano*, **2011**, 5, 3714-3723.
38. Cretu, O.; Krasheninnikov, A. V.; Rodriguez-Manzo, J. A.; Sun, L. T.; Nieminen, R. M.; Banhart, F. Migration and Localization of Metal Atoms on Strained Graphene. *Phys Rev Lett*, **2010**, 105.
39. Robinson, J. A.; LaBella, M.; Zhu, M.; Hollander, M.; Kasarda, R.; Hughes, Z.; Trumbull, K.; Cavaleiro, R.; Snyder, D. Contacting Graphene. *Appl Phys Lett*, **2011**, 98.
40. Cox, N. D.; Rossi, J. E.; Cress, C. D.; Merrill, A.; Crompton, K. R.; Landi, B. J. Spatially Selective Au Nanoparticle Deposition and Raman Analysis of Ion-Irradiated Single-Wall Carbon Nanotubes. *J Phys Chem C*, **2014**, 118, 14031-14038.
41. Puchades, I.; Lawlor, C. C.; Schauerman, C. M.; Bucossi, A. R.; Rossi, J. E.; Cox, N. D.; Landi, B. J. Mechanism of Chemical Doping in Electronic-Type-Separated Single Wall Carbon Nanotubes Towards High Electrical Conductivity. *J Mater Chem C*, **2015**, 3, 10256-10266.
42. Tolvanen, A.; Kotakoski, J.; Krasheninnikov, A. V.; Nordlund, K. Relative Abundance of Single and Double Vacancies in Irradiated Single-Walled Carbon Nanotubes. *Appl Phys Lett*, **2007**, 91.
43. Ziegler, J. F. Srim-2003. *Nucl Instrum Meth B*, **2004**, 219, 1027-1036.
44. Landi, B. J.; Cress, C. D.; Evans, C. M.; Raffaele, R. P. Thermal Oxidation Profiling of Single-Walled Carbon Nanotubes. *Chem Mater*, **2005**, 17, 6819-6834.
45. Aitkaliyeva, A.; Chen, D.; Shao, L. Phonon Transport Assisted by Inter-Tube Carbon Displacements in Carbon Nanotube Mats. *Sci Rep-Uk*, **2013**, 3.
46. Aitkaliyeva, A.; McCarthy, M. C.; Martin, M.; Fu, E. G.; Wijesundera, D.; Wang, X. M.; Chu, W. K.; Jeong, H. K.; Shao, L. Defect Formation and Annealing Kinetics in Ion Irradiated Carbon Nanotube Buckypapers. *Nucl Instrum Meth B*, **2009**, 267, 3443-3446.
47. Krasheninnikov, A. V.; Nordlund, K.; Lehtinen, P. O.; Foster, A. S.; Ayuela, A.; Nieminen, R. M. Adsorption and Migration of Carbon Adatoms on Carbon Nanotubes: Density-Functional Ab Initio and Tight-Binding Studies. *Phys Rev B*, **2004**, 69.
48. Merrill, A.; Cress, C. D.; Rossi, J. E.; Cox, N. D.; Landi, B. J. Threshold Displacement Energies in Graphene and Single-Walled Carbon Nanotubes. *Phys Rev B*, **2015**, 92.
49. Krasheninnikov, A. V.; Banhart, F.; Li, J. X.; Foster, A. S.; Nieminen, R. M. Stability of Carbon Nanotubes under Electron Irradiation: Role of Tube Diameter and Chirality. *Phys Rev B*, **2005**, 72.
50. Warner, J. H.; Schaffel, F.; Zhong, G. F.; Rummeli, M. H.; Buchner, B.; Robertson, J.; Briggs, G. A. D. Investigating the Diameter-Dependent Stability of Single-Walled Carbon Nanotubes. *Acs Nano*, **2009**, 3, 1557-1563.
51. Cress, C. D.; McMorro, J. J.; Robinson, J. T.; Friedman, A. L.; Landi, B. J. Radiation Effects in Single-Walled Carbon Nanotube Thin-Film Transistors. *Ieee T Nucl Sci*, **2010**, 57, 3040-3045.
52. Cress, C. D.; McMorro, J. J.; Robinson, J. T.; Friedman, A. L.; Hughes, H. L.; Weaver, B. D.; Landi, B. J. Total Ionizing Dose-Hardened Carbon Nanotube Thin-Film Transistors with Silicon Oxynitride Gate Dielectrics. *MRS Communications*, **2011**, 1, 27-31.
53. Cress, C. D.; McMorro, J. J.; Robinson, J. T.; Landi, B. J.; Hubbard, S. M.; Messenger, S. R. Radiation Effects in Carbon Nanoelectronics. *Electronics*, **2012**, 1, 23-31.
54. Esqueda, I. S.; Cress, C. D.; Cao, Y.; Che, Y.; Fritze, M.; Zhou, C. The Impact of Defect Scattering on the Quasi-Ballistic Transport of Nanoscale Conductors. *J Appl Phys*, **2015**, 117.
55. LaGasse, S. W.; Cress, C. D.; Hughes, H. L.; Lee, J. U. Atomistic Modeling of Suspended Carbon Nanotube Field Effect Transistors under Proton Radiation. *Ieee T Nucl Sci*, **2015**, 62, 2881-2887.
56. Bushmaker, A. W.; Walker, D.; Mann, C. J.; Oklejas, V.; Hopkins, A. R.; Amer, M. R.; Cronin, S. B. Single Event Effects in Carbon Nanotube-Based Field Effect Transistors under Energetic Particle Radiation. *Nuclear Science, IEEE Transactions on*, **2014**, 2839 - 2846.

DEPARTMENT OF DEFENSE

DEFENSE THREAT REDUCTION
AGENCY
8725 JOHN J. KINGMAN ROAD
STOP 6201
FORT BELVOIR, VA 22060
ATTN: J. CALKINS

DEFENSE TECHNICAL
INFORMATION CENTER
8725 JOHN J. KINGMAN ROAD,
SUITE 0944
FT. BELVOIR, VA 22060-6201
ATTN: DTIC/OCA

**DEPARTMENT OF DEFENSE
CONTRACTORS**

QUANTERION SOLUTIONS, INC.
1680 TEXAS STREET, SE
KIRTLAND AFB, NM 87117-5669
ATTN: DTRIAC